

# Functional Renormalization Group flows as diffusive Hamilton-Jacobi-type equations

Adrian Koenigstein <sup>1</sup>, Martin J. Steil <sup>2</sup> and Stefan Floerchinger <sup>1</sup>

<sup>1</sup>*Theoretisch-Physikalisches Institut, Friedrich-Schiller Universität, D-07743 Jena, Germany.*

<sup>2</sup>*Institut für Kernphysik, Theoriezentrum, Technische Universität Darmstadt, D-64289 Darmstadt, Germany*

(Dated: December 9, 2025)

In this work, we suggest to identify the Functional Renormalization Group flow equations of two-point functions as Hamilton-Jacobi(-Bellman)-type partial differential equations. This reformulation and reinterpretation goes beyond recent developments that treat Renormalization Group flow equations as conservation laws in field space and also allows to systematically understand and handle the nonconservative contributions in flow equations numerically.

We demonstrate this novel approach by first applying it to a simple fermion-boson system in zero spacetime dimensions – which itself presents as an interesting playground for method development. Afterwards, we show, how the gained insights can be transferred to more realistic systems: One is the bosonic  $\mathbb{Z}_2$ -symmetric model in three Euclidean dimensions within a truncation that involves the field-dependent effective potential and field-dependent wave-function renormalization. The other example is the  $(1+1)$ -dimensional Gross-Neveu model within a truncation that involves a field-dependent potential and a field-dependent fermion mass/Yukawa coupling at nonzero temperature, chemical potential, and finite fermion number.

Keywords: Functional Renormalization Group, Hamilton-Jacobi equation, conservation laws, fluid-dynamics, numeric, partial differential equation, Kurganov-Tadmor

## CONTENTS

		C. Boundary conditions	17
I. Introduction	2	VI. Tests and discussion in zero dimensions	18
A. Research issue	2	A. Test 0: Decoupling	19
B. Scope, structure and conception of this work	2	B. Test 1: Minimal test	21
II. The Wetterich equation and its functional derivatives	3	1. Qualitative discussion	21
A. Functional flow equation for the one-point function	4	2. Quantitative discussion	22
B. Functional flow equation for the two-point function	4	C. Test 2: First order phase transition and shock development	23
C. The FRG as an infinite dimensional stochastic optimal control problem	5	1. Qualitative discussion	23
III. Testbed: A zero-dimensional fermion-boson model	6	2. Quantitative discussion	25
A. Expectation values and generating functions	7	D. Test 3: A “mild” sign problem and “shockingly” hard dynamics	25
B. Full field-dependence of the two-point vertex functions	7	1. Discussion from the path-integral perspective	26
IV. The FRG approach to the zero-dimensional model	8	2. Discussion from the FRG perspective	27
A. An exact truncation	9	VII. Applications to higher dimensional models	31
B. FRG flow equations	10	A. Field-dependent wave-function renormalization in the $\mathbb{Z}_2$ -symmetric model	31
C. Comments on the FRG flow equations and their nonconservative form	10	1. Flow equations	31
D. FRG flow equations as coupled viscous Hamilton-Jacobi systems	12	2. Discussion	32
V. Numerical scheme	14	B. Gross-Neveu-Yukawa model	33
A. Original semi-discrete scheme	15	1. Flow equations	36
B. Modifications of the KT-HJ scheme for FRG flow equations	16	2. RG flows	37
		VIII. Conclusions and outlook	39
		Acknowledgments	42
		A. Correlation and vertex functions of the zero-dimensional model	42
		1. Connected correlation functions	42
		2. Vertex functions	42

B. Flow equations from exact inversion of the full field-dependent two-point function	43
C. Flow equations via projections of the Wetterich equation	45
D. Flow equations for the $\mathbb{Z}_2$ -symmetric model	46
1. Callan-Symanzik regulator in three dimensions	47
2. Litim regulator in three dimensions	48
References	49

## I. INTRODUCTION

Within the last decades, the functional renormalization group (FRG) has become a powerful tool for the study of models from statistical physics and quantum field theory (QFT). It was applied successfully to a wide range of problems, such as the study of phase transitions and critical phenomena in the context of particle physics, gravity, and condensed matter physics, see, *e.g.*, Ref. [1] for a review. A strength of the FRG is the possibility to access and evolve theories in the full range of energy/length scales: from high-energy/microphysical scales in the ultraviolet (UV) to low energy/macrophysical scales in the infrared (IR), while resolving field space in a single nonperturbative framework without the need of explicitly solving complicated high-dimensional functional integrals.

### A. Research issue

However, also the FRG has its own shortcomings and practical limitations. One central problem is the issue of truncations, which are usually necessary to make the explicit solution of FRG flow equations, derived from the central governing Wetterich equation, tangible. Still, also within a given truncation, the FRG flow equations are often highly nonlinear coupled partial differential equations (PDEs) and/or ordinary differential equations (ODEs) and their solution is *a priori* an involved task. Prime examples for such systems and common truncations are low-energy effective theories (LEFTs) for Quantum Chromodynamics (QCD) or systems from solid state theory, both in their high-density regimes, where the FRG is used to study – among other things – the scale-dependence of the effective potential, field-dependent wave-function renormalizations, and the flow of field-dependent Yukawa couplings or fermion masses (depending on the perspective). The question arises, how reliable the results of such truncations and the numerical solutions of the corresponding flow equations are, because so far, there seems little consensus on the mathematical structure of the problem and its numerical treatment. One way to address this question is to compare the results

from the FRG to results obtained with other methods or exact results from solvable models.<sup>1</sup> Solvable models are rare or they are trivial, especially in the context of QFTs. Another approach is to perform selfconvergence tests, where the PDEs are solved with different discretization schemes and resolutions. Hence, within this work, we address different closely related topics:

1. We search for toy models that are simple enough to be exactly solvable and rich enough to serve as benchmark tests that mimic many complications of FRG(-model) studies whose truncations involve a field-dependent potential, field-dependent wave-function renormalizations, and/or field-dependent Yukawa couplings.
2. We aim at a reformulation of the FRG flow equations in a form that allows a better application of numerical methods and algorithms and at the same time provides deeper insights into the mathematical structure of the Wetterich equation and its truncated field-dependent flow equations.
3. We want to explicitly find, modify, apply, and test numeric schemes to solve the corresponding PDEs.

### B. Scope, structure and conception of this work

During its conception and early stages<sup>2</sup>, this work was primarily focused on zero-dimensional fermion-boson models and their study within the FRG. The idea was to construct and analyze such models as exactly solvable testbeds for exploring the fermion-boson, *i.e.* Grassmann-scalar, systems in zero dimensions with a focus on the development of numerical methods for coupled flow equations. As the project developed, however, it became apparent that many of the challenges and insights encountered in the zero-dimensional setting pointed towards more general structural questions about the FRG itself. This realization led us to broaden the

<sup>1</sup> We use the term solvable model in the sense of a model, where the expectation values, correlation functions, and vertex functions can be calculated exactly or numerically to arbitrary precision via some other method without approximations.

<sup>2</sup> The present work started as an extension of the series [2–4] and is mentioned in it as “Part IV: A fermion-boson model.” We initially set out to study a zero-dimensional model with four fermions and three scalars with a  $SU(2)$  symmetry. We soon realized that such a model is already diagrammatically and in terms of the resulting differential equations very involved to the point of being ill-suited for a first study of Grassmann-valued degrees of freedom in zero dimensions, see Section 3.3 of Ref. [5] for a discussion. Hence, we decided to consider the simpler – in a sense for our purposes minimal – model discussed in this work. During the preparation of this manuscript, we decided against structuring and framing this work as a direct extension of the series [2–4] in form of a part IV in favor of a more independent publication with a broader focus.

scope and structuring of the present work: before discussing our zero-dimensional fermion-boson model, we first discuss the Wetterich equation and its functional derivatives at a conceptual level. Building on this foundation, we then return to the construction and treatment of the zero-dimensional model, adapt suitable numerical schemes based on our findings, and finally apply these schemes to our zero-dimensional model as well as higher-dimensional systems from statistical physics and QFT.

Concretely, we begin in Section II, by discussing the Wetterich equation and its functional derivatives, with a particular focus on the flow equation of the two-point function in Section II B. We demonstrate that the flow equation of the two-point functions takes the form of a functional (infinite-dimensional), viscous Hamilton-Jacobi-Bellman (HJB) equation. This structure/form is also present in the explicit PDEs derived from this equation – which in fact prompted us to make the identification on the functional level. When working with the flow equation for the two-point function as a HJB equation, the advective and diffusive nature of FRG flows become directly apparent. Furthermore this form allows a more rigorous treatment of nonconservative terms, which arise in computational fluid dynamics (CFD) formulations based on the flow equation of the one-point function, *cf.* Section II A. Apart from practical implications for numerical schemes for the derived PDEs the identification of a HJB structure opens questions of a more general nature, such as the existence and uniqueness of solutions, their stability, convergence, as well as the relation of the FRG to other fields like optimal transport theory, CFD, and infinite-dimensional stochastic optimal control problems. We elaborate on some of these questions and relations in Section II C and Section IV D.

Following the general discussion of Section II, we turn to the construction and introduction of the zero-dimensional fermion-boson model in Section III. The presented model is both minimal and solvable, yet structurally rich enough to be a suitable testing ground for the following numerical developments. Its FRG formulation, presented in Section IV, ties in directly into the conceptual observations of Section II and extends on it using the explicit zero-dimensional setting. It aligns with our previous works [2–4, 6] on purely bosonic, zero-dimensional models with  $N \in \mathbb{N}$  scalar degrees of freedom, which are also called vector models with or without  $O(N)$  symmetry, see, *e.g.*, Refs. [7–24].

In Section V we adapt and combine a numerical scheme [25] developed for the solution of viscous HJB equations with the finite volume methods [26] used in our previous works [2–4, 6].

In Section VI, we apply this scheme to a set of test(case)s constructed within the zero-dimensional fermion-boson model. This model turned out to be a rather rich setting to explore the interplay between fermionic and bosonic fluctuations in a coupled system of field-dependent, flowing couplings. Besides discussing the convergence, stability, and accuracy of our numeri-

cal scheme we also discuss how a “sign-problem” – the problem of probability distributions with “negative probability” – can manifest itself in FRG flow equations of the model under consideration. The related nonanalytic structures in field-space – *i.e.* Yang-Lee zeros – are also discussed in the context of the construction of a reference solution for the FRG flow.

Finally, in Section VII, we extend the discussion to two higher-dimensional models in order to illustrate the broader applicability of our approach. Of particular interest for us are higher-dimensional models and LEFTs of QCD in the high-density regime, where a good and numerically stable resolution of the dynamics in field-space, for example the field-dependent flow of Yukawa couplings, wave-function renormalization, and the effective potential, are crucial [27, 28]. To this end, we investigate the flow of field-dependent wave-function renormalizations in a  $\mathbb{Z}_2$ -symmetric scalar theory in Section VII A in three dimensions and the Gross-Neveu-Yukawa model in 1 + 1 dimensions at nonzero temperature and density in Section VII B. These examples show the applicability of the formulation based on the two-point function/HJB equations and the adapted numerical schemes to physically relevant systems.

In summary, the scope of this work is to connect conceptual advances with concrete applications: beginning with the identification of HJB structures in derivatives of the Wetterich equation, moving to the construction and analysis of a zero-dimensional fermion-boson model as a testbed, and finally adapting and testing numerical schemes both in the toy-model and in selected higher-dimensional applications.

## II. THE WETTERICH EQUATION AND ITS FUNCTIONAL DERIVATIVES

In this section, we discuss the Wetterich equation and its functional derivatives, which play a central role in the FRG approach. The following discussion is focused on the functional dependencies in the Wetterich equation and their consequences and implications. This section does not include a derivation of the Wetterich equation, which can be found in the literature [29–34]. For a more detailed discussion and introduction of the FRG, we refer the interested reader to the nonexhaustive list of Refs. [1, 35–41].

The Wetterich equation for the renormalization group (RG)-time-dependent effective average action (EAA)  $\bar{\Gamma}(t, \Phi)$  is given by

$$\partial_t \bar{\Gamma}(t, \Phi) = \quad (1)$$

$$\begin{aligned} &= \text{STr} \left[ \left( \frac{1}{2} \partial_t R(t) \right) \left( \bar{\Gamma}^{(2)}(t, \Phi) + R(t) \right)^{-1} \right], \\ &\equiv \text{STr} \left[ \left( \frac{1}{2} \partial_t R(t) \right) G(t, \Phi) \right]. \end{aligned} \quad (2)$$

The generic multi-field  $\Phi$ , collects the field content of the theory under consideration, while RG-time  $t \equiv -\ln(k/\Lambda) \in [0, \infty)$  parametrizes the RG-scale  $k$  with respect to a UV reference scale  $\Lambda$ .  $R(t)$  is a matrix-valued regulator and  $\text{STr}$  denotes the supertrace in the conventions of Appendix C of Ref. [42]. In Eq. (2), we have introduced the notation  $G(t, \Phi) \equiv (\bar{\Gamma}^{(2)}(t, \Phi) + R(t))^{-1}$  for the inverse of the second functional derivative of the effective action with respect to the fields  $\Phi$  – the full scale-dependent propagator of the theory. At this point we may note, that the right hand side (r.h.s.) of the Wetterich equation (1) is a functional of the second functional derivative of the EAA with respect to the fields,  $\bar{\Gamma}^{(2)}(t, \Phi)$ , and the regulator function  $R(t)$ , motivating the form

$$\partial_t \bar{\Gamma}(t, \Phi) = \mathcal{F}_R(t, \Phi) [\bar{\Gamma}^{(2)}]. \quad (3)$$

The r.h.s. does notably not depend on the EAA  $\bar{\Gamma}(t, \Phi)$  itself, but only on its functional derivatives in a highly nonlinear fashion. This is a well-known feature shared among implementation of the RG and is a manifestation of the fact, that the vacuum energy (zero-point function) does not affect correlation functions and its absolute value is not relevant<sup>3</sup> for the dynamics of the theory and its renormalization, *cf.* Refs. [43, 44]. At this point we can also see the typical  $n, n+2$  problem posed within flow equations in the FRG: a flow equation for the  $n$ -th moment of the EAA (here explicitly the zeroth moment) depend on the r.h.s. on moments up to order  $n+2$  (here explicitly on the two-point function). This structure is rooted in the inherently nonperturbative nature of the FRG which on the level of Eq. (2) manifests itself by the appearance of the full scale-dependent propagator  $G(t, \Phi)$  on the r.h.s..

#### A. Functional flow equation for the one-point function

Motivated by the fact, that the Wetterich equation (3) for the EAA depends only on derivatives of the latter, we consider the first functional derivative of Eq. (3) with

respect to the field  $\Phi^4$ :

$$\begin{aligned} \partial_t \bar{\Gamma}^{(1)}(t, \Phi) &= \\ &= \frac{\delta}{\delta \Phi} \mathcal{F}_R(t, \Phi) [\bar{\Gamma}^{(2)}] = \\ &= \text{STr} \left[ \left( -\frac{1}{2} \partial_t R(t) \right) G(t, \Phi) \bar{\Gamma}^{(3)}(t, \Phi) G(t, \Phi) \right]. \end{aligned} \quad (4)$$

Equation (4) takes the form of a functional flow/convection<sup>5</sup> equation for the one-point function  $\bar{\Gamma}^{(1)}(t, \Phi)$  and diagrammatically reads

$$\partial_t \left( \text{loop with tadpole} \right) + \frac{\delta}{\delta \Phi} \left( \text{loop with cross} \right) = 0. \quad (6)$$

This form of the Wetterich equation is central to the works [2–6, 27, 28, 42, 45–60] considering (truncations of) the Wetterich equation as conservative equations. Note, that here and in the following, we absorb a minus sign in the symbolic representation of the regulator insertion,  $\otimes = -\frac{1}{2} \partial_t R(t)$  in order to better visualize the relation to CFD and HJB equations.

The highly nonlinear dependence of the propagator  $G(t, \Phi)$  on the Hessian  $\bar{\Gamma}^{(2)}(t, \Phi)$  of the EAA can manifest in advective, diffusive, and most challengingly nonconservative contributions to the flow of the one-point function. Nonconservative contributions are very difficult to handle in explicit numerical schemes, without a deeper understanding of the underlying mathematical structure. To gain further insight into the nature of such contributions and the Wetterich equation itself, we propose to consider the second functional derivative of the Wetterich equation (1) with respect to the field  $\Phi$ .

#### B. Functional flow equation for the two-point function

Taking another functional derivative of Eq. (4) using the explicit form (5) yields the functional flow equation for the two-point function:

<sup>3</sup> Note, however, that in thermodynamic computations  $\lim_{t \rightarrow 0} \bar{\Gamma}(t, \Phi)$  acts as a grand potential and thus differences in the zero-point functions are linked to the pressure.

<sup>4</sup> For compactness and illustrative purposes, we opted for a very compact notation for the functional derivatives and involved signs and permutations, where we hide complexity in the implicit field-space matrix notation and the supertrace  $\text{STr}$ . For a complete derivation we refer the interested reader to App. C.2.4. of Ref. [42].

<sup>5</sup> In the following we use the term convection in the fluid-dynamical sense as a phenomenon including both advection and diffusion.

$$\begin{aligned} & \partial_t \bar{\Gamma}^{(2)}(t, \Phi) + \text{STr} \left[ \left( -\frac{1}{2} \partial_t R(t) \right) G(t, \Phi) \bar{\Gamma}^{(3)}(t, \Phi) G(t, \Phi) \bar{\Gamma}^{(3)}(t, \Phi) G(t, \Phi) \right] = \\ & = \text{STr} \left[ \left( -\frac{1}{2} \partial_t R(t) \right) G(t, \Phi) \bar{\Gamma}^{(4)}(t, \Phi) G(t, \Phi) \right], \end{aligned} \quad (7)$$

which takes the form of a functional (infinite-dimensional), viscous Hamilton-Jacobi-Bellman (HJB) equation, see Refs. [25, 61–68] for a non-exhaustive list of references on HJB equations, their widespread use, and first applications to RG flow equations. Diagrammatically Eq. (7) can be symbolized as

$$\partial_t \left( \text{---} \bigcirc \text{---} \right) + \text{---} \bigcirc \text{---} = \text{---} \bigcirc \text{---} \quad (8)$$

The scale-dependent two-point function  $\bar{\Gamma}^{(2)}(t, \Phi)$  acts as primitive variable and thus Eq. (7) may be formulated as

$$\begin{aligned} & \partial_t \bar{\Gamma}^{(2)}(t, \Phi) + \mathcal{H}_R(t, \Phi) [\bar{\Gamma}^{(2)}, \bar{\Gamma}^{(3)}] = \\ & = \varepsilon_R(t, \Phi) [\bar{\Gamma}^{(2)}, \bar{\Gamma}^{(4)}], \end{aligned} \quad (9)$$

The tadpole diagram manifests as a nonlinear, viscous diffusion term  $\varepsilon_R(t, \Phi) [\bar{\Gamma}^{(2)}, \bar{\Gamma}^{(4)}]$ , where

$$G(t, \Phi) \left( -\frac{1}{2} \partial_t R(t) \right) G(t, \Phi) \quad (10)$$

acts as a nonlinear diffusion coefficient, while the bubble diagrams manifest as a nonlinear advective/drift contribution, encoded by the Hamiltonian  $\mathcal{H}_R(t, \Phi) [\bar{\Gamma}^{(2)}, \bar{\Gamma}^{(3)}]$ . The dependence on the primitive variable/the two-point function remains highly nonlinear through the products of propagators in the super-traces, while the higher moments of  $\bar{\Gamma}^{(2)}$  – namely the three- and four-point functions  $\bar{\Gamma}^{(3)}$  and  $\bar{\Gamma}^{(4)}$  appear only squared and linearly, respectively. The  $n, n+2$  problem (in this subsection explicitly with  $n=2$ ) is therefore directly apparent. In the present context it may be seen not as a technical obstacle, but as a structural feature that invites reformulation and reinterpretation. The HJB equation is nonconservative but allows for a more rigorous classification of the flow equation, even on functional level. Both CFD and HJB formulations provide ways to work the  $n, n+2$  problem

by providing frameworks on how to deal with the higher derivatives, without the explicit need for a truncation in the canonical vertex-expansion sense or ad-hoc approaches to compute the higher derivatives numerically, which both can be very limited due to properties of  $\bar{\Gamma}$  like convexity (in the IR), phase transitions, and/or the emergence of nonanalytic points. From the HJB perspective, entropy solutions – central in the conservative/CFD formulations – may find a more natural and robust generalization within the viscosity solution framework of HJB theory [63, 69]. This could open new directions for both the analysis and numerical treatment of FRG equations, suggesting (numerical) approximation schemes and concepts that are better aligned with the fundamental nature of the FRG.

The classification of Eq. (7) in Eq. (9) as a functional HJB equation is of central importance for this work and might have even further reaching consequences beyond the scope of this work.

For the remainder of this subsection, we outline the impact of this identification and formulation on the present work, while in the next Section II C we elaborate and, to some extent, speculate on further conceptual implications of identifying a functional HJB equation as governing equation of the FRG. In Section IV we will discover a direct manifestation of Eq. (9) as a system of PDEs describing the zero-dimensional model of Section III, while in Section VII PDEs of HJB-type arise in truncations of higher-dimensional models and projections involving the two-point function. Considering the PDEs as HJB equations allows us to combine at this point established finite volume methods used in the CFD-based formulations of the Wetterich equation with methods developed for HJB equations. We use a HJB-approach for nonconservative contributions while maintaining a finite volume formulation for conservative contributions. The reason for this split is based *a posteriori* on our explicit numerical tests in Section VI, and especially in Section VII, rather than on conceptual arguments.

### C. The FRG as an infinite dimensional stochastic optimal control problem

An intriguing perspective for future research emerges from the observation that the FRG flow equation (7) for the two-point function manifests as a functional HJB equation, which naturally decomposes into drift and diffusion terms. Considering  $G(t, \Phi) \left( -\frac{1}{2} \partial_t R(t) \right) G(t, \Phi)$  as



a diffusion coefficient of a McKean-Vlasov-type stochastic process, it might be possible to interpret the FRG as an infinite dimensional stochastic optimal control problem [63, 64, 69]. In this context, the nonlinear but instantaneous dependence of the diffusion coefficient on the evolving two-point function reflects the endogeneity of the system, where noise and control are governed by the current effective description, highlighting the semigroup and nonperturbative nature of the FRG flow: all relevant information is encoded in the present, not in explicit memory of the past. Wilson’s RG approach of integrating out fluctuations momentum shell by momentum shell might be interpreted as an implementation of Chapman-Kolmogorov/Bellman’s principle in the stochastic optimal control/dynamic programming framework.

In the context of the RG ideas in this/similar directions are not new, *cf.* Refs. [67, 70, 71], but to our knowledge an attempt of a formulation/strong link for/between the FRG formulated in terms of the EAA governed by the Wetterich equation (2) and stochastic optimal control has not been made yet. Making such a link and studying connections to optimal transport, dynamic programming, and related concepts could yield a deeper understanding of the mathematical structure of (functional) renormalization group ((F)RG)<sup>6</sup> flows and inspire new conceptual insights as well as more powerful numerical and analytical methods. Further work and remarks to this end are beyond the scope of the present study, which ultimately focuses on numerical methods, but we believe the connections sketched above warrant closer examination in future studies.

### III. TESTBED: A ZERO-DIMENSIONAL FERMION-BOSON MODEL

In this section, we introduce a toy model that is simple enough to allow for a detailed comparison of numeric calculations with analytical solutions, while being rich enough to serve as a nontrivial test for RG dynamics in field space with fermions. Furthermore, it allows us to study the aforementioned mathematical structure of the FRG flow equations in a concrete setting.

We consider a zero-dimensional QFT with a single bosonic and two fermionic degrees of freedom, which are coupled to each other. The (moment) generating function of the model under consideration reads

$$\mathcal{Z}(J, \tilde{\eta}, \eta) = \mathcal{N} \int_{-\infty}^{+\infty} d\phi \int d\tilde{\theta} d\theta \times \exp(-\mathcal{S}(\phi, \tilde{\theta}, \theta) + J\phi + \tilde{\eta}\theta + \tilde{\theta}\eta), \quad (11)$$

where  $\phi$  is the bosonic field,  $\tilde{\theta}$  and  $\theta$  are the fermionic fields, and  $J$ ,  $\tilde{\eta}$ , and  $\eta$  are the sources for the bosonic and fermionic fields, respectively, and  $\mathcal{N}$  is the normalization factor. Of course, the term “field” is a bit misleading in this context, because bosonic fields are simply real numbers, while the fermionic fields are two different ordinary Grassmann numbers ( $\tilde{\theta}$  and  $\theta$  are not complex conjugate to each other). In our following discussion we will however maintain the term field even though mathematically we are just discussing numbers. The Grassmann numbers  $\tilde{\theta}$  and  $\theta$  obey

$$\theta^2 = \tilde{\theta}^2 = 0, \quad \theta\tilde{\theta} + \tilde{\theta}\theta = 0. \quad (12)$$

with the usual conventions, see, *e.g.*, the textbooks [44, 72, 73], for Berezin integration [72] over Grassmann-variables, *e.g.*,

$$\int d\theta_a 1 = 0, \quad \int d\theta_a \theta_a = 1, \quad \theta_a \in \{\theta, \tilde{\theta}\}. \quad (13)$$

The most general action, that is at least quadratic in the fields, reads

$$\mathcal{S}(\phi, \tilde{\theta}, \theta) = \tilde{\theta} H(\phi) \theta + U(\phi), \quad (14)$$

where  $H(\phi)$  and  $U(\phi)$  are arbitrary functions of  $\phi$  that are supposed to be invariant under the transformation  $\phi \rightarrow -\phi$ . This model shares some similarities with the zero-dimensional supersymmetric model in Ref. [16] but is in the present form and context novel to our knowledge. We will also assume that  $H(\phi) \neq 0$  at least for some values of  $\phi$  – otherwise the partition function would vanish and the model would be trivial. Note that for constant  $H(\phi)$  fermions and bosons decouple and we are left with a bosonic  $\mathbb{Z}_2$ -symmetric model. We studied such bosonic  $\mathbb{Z}_2$ -symmetric models in detail in our previous works [2–4] and we refer to these works for an in-depth discussion of this limit/sector of the present model. To ensure convergence of the integrals in the partition function (11) and the related expectation values, *cf.* Section A 1,  $U(\phi)$  should asymptotically at least grow like  $\phi^2$  and  $H(\phi)$  should not grow faster than polynomial. However, the functions  $U(\phi)$  and  $H(\phi)$  do not need to be analytic. In the following we denote  $H(\phi)$  as a (generalized) Yukawa coupling that can involve a mass term for the fermions as well as couplings to the bosonic field.<sup>7</sup> The function  $U(\phi)$  is the (self-interaction) potential for the bosonic field. To resolve the entire field-space  $\phi$  one can introduce an explicit term in the potential which breaks  $\phi \rightarrow -\phi$  symmetry or work with nonzero sources  $J$  to sample different values of  $\phi$ . For this work we practically choose to do the latter. However, this is mentioned explicitly.

<sup>6</sup> We use the abbreviation (F)RG in statements that apply both to the functional renormalization group and to the nonperturbative renormalization group in general.

<sup>7</sup> Note, that for the sake of simplicity and in contrast to Yukawa couplings in higher spacetime dimensions our field-dependent Yukawa coupling is supposed to be an even function of  $\phi$ . Furthermore due to the field-dependency  $H(\phi)$  does not act as a simple two-fermion-one-boson coupling like the name would canonically suggest. Nonvanishing derivatives  $\partial_\phi^n H(\phi)$  correspond to two-fermion- $n$ -boson couplings, *cf.* Eq. (34).

### A. Expectation values and generating functions

Next, we turn to the calculation of expectation values and generating functions for the model. We start with the normalization factor, which is given by

$$\mathcal{N}^{-1} = \int_{-\infty}^{\infty} d\phi H(\phi) \exp(-U(\phi)), \quad (15)$$

in order to have  $\mathcal{Z}(0,0,0) = 1$ , where we applied the rules (13) for integration over Grassmann numbers (Berezin integrals). The remaining  $\phi$ -integration may be performed by hand for specific choices of  $H(\phi)$  and  $U(\phi)$ . Otherwise, the integral can be evaluated to preferred precision using standard methods for numerical integration.

Now, we study two classes of correlation functions. First, we consider purely bosonic expectation values. The expectation value of some function  $f(\phi)$  is given by

$$\langle f(\phi) \rangle = \mathcal{N} \int_{-\infty}^{\infty} d\phi H(\phi) f(\phi) \exp(-U(\phi)), \quad (16)$$

where we already integrated out the fermionic fields. Second, we consider expectation values involving fermionic fields. Since there are only two fermionic fields, the only nonvanishing type of expectation value is the product of a function  $g(\phi)$  times  $\tilde{\theta}\theta$ ,

$$\langle g(\phi) \tilde{\theta}\theta \rangle = -\mathcal{N} \int_{-\infty}^{\infty} d\phi g(\phi) \exp(-U(\phi)). \quad (17)$$

This also includes the fermionic two-point correlation function<sup>8</sup>, for which  $g(\phi) = 1$ . Again, the remaining  $\phi$ -integrations are easily calculated for specific choices of  $H(\phi)$  and  $U(\phi)$  either analytically or numerically. Note, that the expectation value of a single fermionic field as well as higher-order fermionic expectation values vanish due to the Berezin integration, *i.e.*, the Grassmann-nature of  $\tilde{\theta}$  and  $\theta$ . On the other hand, the functions  $f$  and  $g$  can be arbitrary functions of  $\phi$ , however, expectation values that are odd in  $\phi$  vanish for vanishing source  $J$  – without the additional term  $-c\phi$  in the potential.

Before we continue, let us mention that on the level of the above integrals also functions with  $H(\phi) < 0$  for some values of  $\phi$  are allowed and may lead to negative expectation values. From the perspective of a probability distribution and partition function this seems to be problematic and can be considered as a simple model for the “sign-problem” in QFT and statistical physics, which we will also analyze from the FRG perspective.

Furthermore, it is interesting to remark the following: As long as one is solely interested in purely bosonic expectation values, one may integrate out the fermionic fields

right from the start and obtain an effective action<sup>9</sup>

$$\tilde{\mathcal{S}}(\phi) = U(\phi) - \ln(H(\phi)) \quad (18)$$

for the bosonic field and a partition function

$$\tilde{\mathcal{Z}}(J) = \int_{-\infty}^{\infty} d\phi \exp(-\tilde{\mathcal{S}}(\phi) + J\phi). \quad (19)$$

This is also standard in QFT problems, while it is usually not possible to further evaluate the remaining  $\phi$ -integrals because of the general spacetime dependence of the fields and derivative-terms in the fermion determinant.

Introducing the Schwinger functional (in the present context a simple function)

$$\mathcal{W}(J, \tilde{\eta}, \eta) = \ln \mathcal{Z}(J, \tilde{\eta}, \eta), \quad (20)$$

one can calculate connected correlation functions by taking functional derivatives of  $\mathcal{W}$  with respect to the sources. Explicit expressions for the first few relevant connected correlation functions can be found in App. A 1.

Since the FRG is formulated in terms of the EAA, we are also interested in the vertex functions of the model. Otherwise, direct comparison between the FRG and the exact results is not possible. First, we introduce the effective action as the Legendre transform of the Schwinger functional,

$$\Gamma(\varphi, \tilde{\vartheta}, \vartheta) = \sup_{J, \tilde{\eta}, \eta} \{J\varphi + \tilde{\eta}\vartheta + \tilde{\eta}\eta - \mathcal{W}(J, \tilde{\eta}, \eta)\}. \quad (21)$$

Here,  $\varphi$ ,  $\tilde{\vartheta}$ , and  $\vartheta$  are the mean-fields. Then, the vertex functions are defined as the functional derivatives of the effective action with respect to the fields,

$$\Gamma^{(l,m,n)}(\varphi, \tilde{\vartheta}, \vartheta) = \frac{\delta^{(l+m+n)} \Gamma(\varphi, \tilde{\vartheta}, \vartheta)}{\delta \varphi^l \delta \vartheta^m \delta \tilde{\vartheta}^n}, \quad (22)$$

which need to be evaluated at the physical point – here  $\varphi = 0 = \tilde{\vartheta} = \vartheta$  – corresponding to the minimum of the effective action and is in agreement with the expectation values of  $\langle \phi \rangle = 0 = \langle \tilde{\theta} \rangle = \langle \theta \rangle$  in the absence of explicit symmetry breaking terms. Explicit expressions for the first few relevant vertex functions can be found in App. A 2.

### B. Full field-dependence of the two-point vertex functions

Factually, during our FRG calculations we will not only obtain the vertex functions at the physical point, but we even have to resolve the full field-dependence of the vertex functions for solving the corresponding PDEs. Oftentimes, the full field-dependence of the vertex functions is

<sup>8</sup> Again, we use the names from standard QFT even though the term “two-point” does not really make sense in a model that lives in a single spacetime point.

<sup>9</sup> This is only directly possible, where  $H(\phi) > 0$ , while where  $H(\phi) < 0$  one may use  $\ln(|H(\phi)|) + i\pi$ .

of minor interest, because the physical point is the only relevant one, and it only becomes important with explicit symmetry breaking terms *etc.*. However, we could also compare the solution of the RG flows globally, at every point in field space, to the exact results to benchmark our methods.

In order to do so, we first need the relation between  $\varphi$  and  $J$  from the Legendre transformation (21),

$$\begin{aligned}\varphi(J) &= \frac{\delta\mathcal{W}(J, 0, 0)}{\delta J} = \\ &= \frac{1}{\mathcal{Z}(J, 0, 0)} \frac{\delta\mathcal{Z}(J, 0, 0)}{\delta J} = \langle\phi\rangle_J.\end{aligned}\quad (23)$$

This quantity can be computed numerically for arbitrary  $J$  from Eq. (11). (For  $J = 0$  we recover the expectation value of the bosonic field  $\langle\phi\rangle$  that vanishes for symmetric  $U(\phi)$  and  $H(\phi)$ .) The inversion of this dependence is  $J(\varphi)$ , which can be computed (numerically) from  $\varphi(J)$ . However, from the Legendre transformation (21) we also have

$$J(\varphi) = \frac{\delta\Gamma(\varphi, 0, 0)}{\delta\varphi}.\quad (24)$$

Hence, we also directly obtain the full field-dependence of  $J$  as the field-dependent bosonic one-point vertex function. This already allows for a global comparison of the FRG results to the exact results.

However, we can also go a step further and consider the field-dependence of the two-point vertex functions. For the bosonic one, we have

$$\begin{aligned}\Gamma^{\varphi\varphi}(\varphi) &= \frac{\delta^2\Gamma(\varphi, 0, 0)}{\delta\varphi^2} = \\ &= \left(\frac{\delta^2\mathcal{W}(J, 0, 0)}{\delta J^2}\right)^{-1}\Big|_{J=J(\varphi)} = \\ &= \left(\frac{1}{\mathcal{Z}(J, 0, 0)} \frac{\delta^2\mathcal{Z}(J, 0, 0)}{\delta J^2} + \right. \\ &\quad \left. - \underbrace{\left(\frac{1}{\mathcal{Z}(J, 0, 0)} \frac{\delta\mathcal{Z}(J, 0, 0)}{\delta J}\right)^2}_{\varphi}\right)^{-1}\Big|_{J=J(\varphi)},\end{aligned}\quad (25)$$

which reduces to Eq. (A5) at the physical point. It can be calculated from the numerical solution of the RG flow equations for all discretization points in field space directly. The reference values are obtained by calculating the respective  $J(\varphi)$  with Eq. (24) and then evaluating the r.h.s. of Eq. (25) numerically with Eq. (11).

Lastly, we find the full field-dependence of the fermionic two-point function

$$\Gamma^{\tilde{\vartheta}\vartheta}(\varphi) = \frac{\delta^2\Gamma(\varphi, 0, 0)}{\delta\tilde{\vartheta}\delta\vartheta} = \quad (26)$$

$$= - \left(\frac{\delta^2\mathcal{W}(J, 0, 0)}{\delta(-\eta)\delta\tilde{\eta}}\right)^{-1}\Big|_{J=J(\varphi)}.$$

Again, we can calculate this quantity for all discretization points in field space from the numeric solution of the PDE of the RG flow equations and compare it to the reference values. The latter are obtained the same way as for the bosonic two-point vertex function. Note, that we directly dropped vanishing terms in all of the above formulae for the sake of the readability.

Finally, let us remark that one can use exactly the same formulae to extract the exact field-dependent two-point functions during the RG flow at nonzero regulator to compare them to our numerical results or simply study their scale-dependence. Here, one merely has to add the regulator insertion (see next paragraphs and Eq. (29)) to the classical action  $\mathcal{S}$  in Eq. (11) and repeat the above steps for finite RG time  $t$ .

Having these quantities at hand, we are now well equipped to turn to the FRG approach and compare the results of the FRG to the exact results of the toy model.

#### IV. THE FRG APPROACH TO THE ZERO-DIMENSIONAL MODEL

In this section, we turn to the FRG formulation of the toy model. Here, we shall however not repeat the general derivation of the Wetterich equation, which was presented numerous times in the literature. The same applies to the above discussion on the flow-equation for the two-point vertex function and its relation to the HJB equation. Still, because we are working in the unconventional context of zero spacetime dimensions, we discuss the main differences to the standard approach. Let us therefore summarize the fields in the field-space vector  $\Phi = (\varphi, \vartheta, \tilde{\vartheta})^T$ . Then, the FRG flow equation (1) reads

$$\begin{aligned}\partial_t\bar{\Gamma}(t, \Phi) &= \\ &= \text{STr} \left[ \left(\frac{1}{2}\partial_t R(t)\right) (\bar{\Gamma}^{(2)}(t, \Phi) + R(t))^{-1} \right],\end{aligned}\quad (27)$$

where  $R(t)$  is the matrix-valued regulator function and  $\text{STr}$  denotes the supertrace in the conventions of Appendix C of Ref. [42]. Furthermore,  $\bar{\Gamma}^{(2)}(t, \Phi)$  is the matrix of second derivatives of the EAA with respect to the fields. Remember, that the EAA is defined as a shift of the scale-dependent effective action by the regulator insertion,

$$\bar{\Gamma}(t, \Phi) = \Gamma(t, \Phi) - \Delta\mathcal{S}(t, \Phi),\quad (28)$$

which both approach the full effective action Eq. (21) in the limit  $t \rightarrow \infty$ . The regulator insertion for our zero-dimensional model is given by

$$\Delta\mathcal{S}(t, \Phi) = \frac{1}{2} r_b(t) \varphi^2 + \tilde{\vartheta} r_f(t) \vartheta.\quad (29)$$



The mathematical nature of the regulator is, where one main difference to FRG in nonzero dimension arises. In our zero-dimensional setup, the regulator shape functions  $r_b(t)$  and  $r_f(r)$  are plain monotonically decreasing functions of the RG time  $t \in [0, \infty)$  with

$$r_{b/f}(t=0) = \Lambda, \quad \lim_{t \rightarrow \infty} r_{b/f}(t) = 0, \quad (30)$$

where  $\Lambda$  is the ultraviolet cutoff that is supposed to be much larger<sup>10</sup> than any other scales in the problem. In general, regulator shape functions also depend on the momentum and in some setups even on the fields themselves, see, *e.g.*, Refs. [37, 40, 51, 74–76] for a general discussion. In our zero-dimensional model, momenta do not exist and we do not consider regulator insertions with additional field-dependencies beyond Eq. (29). Additionally, the RG scale is usually of energy dimension, while in our case it is dimensionless. One can simply think of the regulator shape functions as scale-/RG-time-dependent (dimensionless) mass terms for the fields – similar to the Callan-Symanzik-type regulators in higher dimensions [37, 77–83]. Otherwise and structurally, the FRG flow equation is the same as in the higher-dimensional case (within a truncation), especially with respect to (w.r.t.) its structure as a PDE system in field space. To be specific, we use

$$r_{b/f}(t) = \Lambda e^{-\gamma_{b/f} t}. \quad (31)$$

It is also possible to use other monotonically decreasing functions, due to reparameterization invariance of the FRG in zero dimensions. In fact, we use the same regulator shape functions for fermions and bosons  $r_b(t) = r_f(t)$  with  $\gamma_{b/f} = 1$ . However, it is also possible to shift the regulators against each other, which we also did during testing by setting  $\gamma_b = 1$  and  $\gamma_f \neq 1$ . Similar shifts between the fermionic and bosonic RG-scale/-time have recently gained some attention in FRG studies of LEFTs of QCD, see, *e.g.*, Ref. [28]. A shift of dynamics between fermions and bosons is *a priori* difficult to motivate in the present zero-dimensional study and after semi-successful tests, we decided to keep the focus on other aspects of our novel approach. Still, it might be an interesting aspect from a numerics perspective for further studies beyond the scope of this work.

Finally, let us remark that  $\Gamma(t, \Phi)$  from the r.h.s. of Eq. (28), as being the Legendre transform of the scale-dependent Schwinger functional  $\mathcal{W}(t, \mathcal{J})$ , has to be a convex function for all  $t$ , such that  $\Gamma^{(2)} = \bar{\Gamma}^{(2)} + R$  has to be positive for finite  $t$  and positive or zero for  $t \rightarrow \infty$ . The former ensures invertibility in the Wetterich equation (27). For finite UV cutoff  $\Lambda$  this of course restricts the space of admissible initial actions  $\mathcal{S}(\Phi)$  to those that yield a convex  $\Gamma(t, \Phi)$  at  $t = 0$ . During the flow, the

Wetterich equation is self-healing and always ensures convexity of  $\Gamma(t, \Phi)$  for  $t > 0$ , if it is convex at  $t = 0$ . However, also note that in contrast to higher-dimensional examples, where it is not always possible to enlarge the UV cutoff trivially, this can indeed be done in our zero-dimensional models, such that here, we do not have to worry about this restriction in practice and simply sufficiently enlarge  $\Lambda$ .

### A. An exact truncation

Normally it is not possible to solve the Wetterich equation (1) exactly and one has to resort to truncation schemes, such as the derivative, vertex or operator expansions. This is usually done by specifying a set of relevant fields and interactions and then truncating the EAA  $\bar{\Gamma}(t, \Phi)$  at a certain order in the fields or derivatives. Within this approximation, a particular subset of these couplings/vertices is treated as scale-dependent. Thereby one has to ensure, that  $\bar{\Gamma}(t, \Phi)$  matches the classical action  $\mathcal{S}(\Phi)$  (or the one-loop correction to  $\mathcal{S}$ ) at the ultraviolet cutoff scale  $\Lambda$  for  $\Lambda \rightarrow \infty$ . However, zero-dimensional models are special in this respect, because all possible interactions can be included in the EAA via a simple ansatz. It is therefore theoretically possible to solve the Wetterich equation exactly for the toy model. The particular ansatz is of similar shape as the most general form for the classical action (14),

$$\bar{\Gamma}(t, \Phi) = \tilde{\vartheta} H(t, \varphi) \vartheta + U(t, \varphi). \quad (32)$$

The difference is, that we promote the functions  $H(\phi)$  and  $U(\phi)$  to scale-dependent functions  $H(t, \varphi)$  and  $U(t, \varphi)$  and exchange the fluctuating quantum fields  $\phi, \tilde{\theta}, \theta$  from the (functional) integral (11) with mean-fields  $\varphi, \tilde{\vartheta}, \vartheta$  from the Legendre transformation (21). Note again that reference values for  $H(t, \varphi)$  and  $U(t, \varphi)$  can be calculated directly for all  $t$  from Eqs. (25), (26), and (28) by adding the regulator insertion Eq. (29) to the classical action in Eq. (11) and repeating the steps from Section III B.

In the next step, one would have to insert the ansatz (32) into the Wetterich equation (1) and solve the PDE with the initial condition  $\bar{\Gamma}(t=0, \Phi) = \mathcal{S}(\Phi)$ . Of course, this is a nontrivial task, because the Wetterich equation is a nonlinear PDE in field space and especially the exact inversion of the full matrix-valued and field-dependent two-point function is rarely possible. In practice, one projects the flow equation onto the couplings/vertices contained in the truncation, here  $H(t, \varphi)$  and  $U(t, \varphi)$ , and then solves the resulting system of coupled PDEs and/or ODEs. Usually, this is done by taking derivatives of Eq. (1) with respect to the fields and then evaluating the resulting expressions on a particular field configuration. We will also follow this approach. However, due to the momentum-independence of the model, we can also extract the flow equations for  $H(t, \varphi)$  and  $U(t, \varphi)$

<sup>10</sup> Actually one should send  $\Lambda \rightarrow \infty$ , which is not possible in practice for numerical calculations.

directly from the Wetterich equation. Indeed, in zero dimensions, it is possible to exactly invert the full two-point function and afterwards to evaluate the trace on the right hand side of the Wetterich equation exactly. Both approaches are presented in detail in the Appendices B and C, respectively. Hence, a clear advantage of this zero-dimensional model is that a truncation of the Wetterich equation is not necessary but still possible, which allows for a direct comparison of the results of the exact and truncated solutions as well as the numerical solution to the exact results. Within this work, we solely focus on the numerical solution of the exact flow equations without testing artificial truncations. This might be subject of future work. (Nonetheless, first unsystematic tests already suggest that significant truncation artifacts can be expected for most interesting test cases and applications.) A surplus is that it also allows to easily analyse the mathematical structure of the flow equations as coupled PDEs.

### B. FRG flow equations

Applying either the exact inversion approach, see Appendix B, or the common projection approach, see Appendix C, we obtain two coupled PDEs as RG flow equations for our model from the Wetterich equation (1). These are the flow equation of the (scale-dependent) effective potential,

$$\partial_t U = - \left( -\frac{1}{2} \partial_t r_b \right) \frac{1}{r_b + \partial_\varphi^2 U} + \left( -\partial_t r_f \right) \frac{1}{r_f + H} = \quad (33)$$

$$= - \text{[diagram: blue zigzag loop with a crossed circle vertex]} + \text{[diagram: orange solid loop with a crossed circle vertex]},$$

and the flow equation of the (scale-dependent) (generalized) Yukawa coupling

$$\partial_t H = -2 \left( -\frac{1}{2} \partial_t r_b \right) \frac{1}{(r_b + \partial_\varphi^2 U)^2} \frac{1}{r_f + H} (\partial_\varphi H)^2 + \quad (34)$$

$$+ \left( -\frac{1}{2} \partial_t r_b \right) \frac{1}{(r_b + \partial_\varphi^2 U)^2} \partial_\varphi^2 H +$$

$$-2 \left( -\frac{1}{2} \partial_t r_f \right) \frac{1}{r_b + \partial_\varphi^2 U} \frac{1}{(r_f + H)^2} (\partial_\varphi H)^2 =$$

$$= - \text{[diagram: blue zigzag loop with a crossed circle vertex and two fermion lines]} + \text{[diagram: orange solid loop with a crossed circle vertex and two fermion lines]} +$$

$$- \text{[diagram: blue zigzag loop with a crossed circle vertex and two fermion lines]}.$$

Here, we used the abbreviated form  $U \equiv U(t, \varphi)$ ,  $H \equiv H(t, \varphi)$  as well as  $r_b \equiv r_b(t)$  and  $r_f \equiv r_f(t)$  and introduced a common diagrammatic notation for the flow equations in terms of Feynman diagrams: Regulator insertions,  $-\frac{1}{2} \partial_t r_{b/f}$ , are represented by crossed circles, bosonic/fermionic propagators,

$$\frac{1}{r_b + \partial_\varphi^2 U}, \quad \frac{1}{r_f + H}, \quad (35)$$

by zigzag/solid blue/orange lines, respectively, and vertices,  $\partial_\varphi^2 H$  and  $\partial_\varphi H$ , by dots. Solving this system of PDEs with the initial conditions  $U(t=0, \varphi) = U(\varphi)$  and  $H(t=0, \varphi) = H(\varphi)$  to  $t \rightarrow \infty$  is indeed mathematically equivalent to calculating the vertex functions from the partition function.<sup>11</sup> However, as is directly apparent from the flow equations, the system is highly nonlinear and a solution nontrivial, while the (numerical) calculation of the vertex functions from the partition function is in contrast straightforward. In realistic QFTs in higher dimensions, this is not the case and the direct calculation of expectation values and vertex functions from the functional integral is challenging. In this case, solving nonlinear PDE systems might be a reasonable alternative, which is why the FRG was developed in the first place and why we are testing adequate numerical methods for the solution of the flow equations in this work.

### C. Comments on the FRG flow equations and their nonconservative form

Before we continue with specific solution methods for the PDE system, we want to make some remarks on its form.

1. The flow equations have almost exactly the same structure as the flow equations in higher space-time dimensions for systems of bosons and fermions that are interacting via a local, field-dependent Yukawa coupling and bosonic self-interactions. In higher dimensions, however, considering solely a field-dependent Yukawa coupling (all quark-antiquark- $n$ -boson scattering processes) and the field-dependent bosonic potential (all  $n$ -boson scatterings) constitutes a truncation – the lowest order in the derivative expansion.<sup>12</sup> Still, working

<sup>11</sup> Hereby, the vertex functions have to be extracted from  $U(t \rightarrow \infty, \varphi)$  and  $H(t \rightarrow \infty, \varphi)$  by calculating derivatives w.r.t.  $\varphi$  at the minimum of the entire action, which is without explicit symmetry breaking at  $\varphi = 0 = \tilde{\vartheta} = \vartheta$ .

<sup>12</sup> In Ref. [28] referred to as self-consistent local potential approximation (scLPA) in the context of the quark-meson (QM) model.

within this truncation requires a nontrivial numerical solution of the flow equations. Examples for studies that work within this approximation are Refs. [27, 28, 84]. Some of these face severe challenges in the solution of the PDE system, especially in the presence of a chemical potential. At the end of this work, we also apply our developments to a particular higher-dimensional model – the Gross-Neveu-Yukawa model – within this truncation to demonstrate the applicability.

2. The system is of first order in  $t$ - and up to second order in  $\varphi$ -derivatives. Since  $t$  serves as the evolution parameter its interpretation and denotation as a time  $t \in [0, \infty)$  in the context of the PDE system is rather natural and we call it the RG time. On the other hand, this implies that  $\varphi \in (-\infty, \infty)$  can be seen as the spatial domain, which has, however, to be mapped or truncated to a finite domain for numerical purposes.
3. It was already pointed out in previous works [2–4, 6, 27, 45, 47, 51], that, as a consequence of the latter, the bosonic contribution to Eq. (33) can indeed be interpreted as a (advection-)diffusion equation. The most simple way to see this is by taking

$$\begin{aligned} \partial_t M &= \frac{d}{d\varphi} \left( - \left( \frac{1}{2} \partial_t r_b \right) \frac{1}{(r_b + M)^2} \partial_\varphi M + (\partial_t r_f) \frac{1}{(r_f + H)^2} \partial_\varphi H \right) = \\ &= - \left( \frac{1}{2} \partial_t r_b \right) \frac{1}{(r_b + M)^2} \partial_\varphi^2 M + 2 \left( \frac{1}{2} \partial_t r_b \right) \frac{1}{(r_b + M)^3} (\partial_\varphi M)^2 + (\partial_t r_f) \frac{1}{(r_f + H)^2} \partial_\varphi^2 H - 2 (\partial_t r_f) \frac{1}{(r_f + H)^3} (\partial_\varphi H)^2. \end{aligned} \quad (37)$$

The first line is again the conservative form of the flow equation for  $M$ , while the second line has the structure of an advection-diffusion equation for  $M$  with nonlinear coefficients. Hereby, the first term on the right hand side is a diffusion term with a manifestly positive nonlinear diffusion coefficient, while the second term is interpreted as an advection term with a fluid velocity that depends itself on  $\partial_\varphi M$  as well as the other prefactors. The terms proportional to the derivatives of  $H$  enter as source terms in the evolution equation of  $M$  but have in

another  $\varphi$ -derivative of Eq. (33), see also Eq. (6),

$$\begin{aligned} \partial_t u &= \frac{d}{d\varphi} \left[ \left( \frac{1}{2} \partial_t r_b \right) \frac{1}{r_b + \partial_\varphi u} - (\partial_t r_f) \frac{1}{r_f + H} \right] = \\ &= - \left( \frac{1}{2} \partial_t r_b \right) \frac{1}{(r_b + \partial_\varphi u)^2} \partial_\varphi^2 u + \\ &\quad + (\partial_t r_f) \frac{1}{(r_f + H)^2} \partial_\varphi H, \end{aligned} \quad (36)$$

and define  $u(t, \varphi) \equiv \partial_\varphi U(t, \varphi)$ . The first term on the right hand side of Eq. (36) is a nonlinear diffusion term with a manifestly positive nonlinear diffusion coefficient that itself is a function of  $t$  and  $\partial_\varphi u$ . The fermionic contribution, however, is of source type in the time evolution of  $u$ . However, let us also recapitulate that using the  $\varphi$ -derivative without explicitly evaluating it, Eq. (36) can also be seen as rewriting the flow equation for  $u$  in a conservative form, which is a common technique in the context of diffusion-advection equations, which was leveraged in the previously mentioned works.

Another way of dealing with the flow equation for  $U$  is to even go one derivative higher and work with the flow of the field dependent mass (squared)<sup>13</sup>  $M(t, \varphi) = \partial_\varphi^2 U(t, \varphi)$ , as it was for example done in Refs. [28, 56, 57]. Then, the flow equation for  $M$  reads

general the same structure as the bosonic advection and diffusion terms. Overall, the clear advantage of this version is that none of the coefficients in front of derivatives of  $M$  and  $H$  contain denominators that depend on spatial derivatives of  $M$  or  $H$ . In particular, this is advantageous when the propagators have to be evaluated close to their poles or velocities on the level of the PDE have to be calculated.

4. A similar interpretation can be given to the flow equation for the Yukawa coupling  $H(t, \varphi)$ , see Eq. (34). There is also a diffusion term with manifestly positive nonlinear diffusion coefficient, the second term, which is the tadpole contribution in FRG language. The first and third terms, which correspond to the fermion self-energies, are inter-

<sup>13</sup> Note, despite calling it a mass,  $M$  can be negative and is not necessarily the mass of a particle in the sense of a physical interpretation.

preted as advective contributions, since they depend on the first derivative of  $H$ . Again, the velocity field is proportional to  $\partial_\varphi H$  itself. However, the flow equation for the Yukawa coupling – to the best of our knowledge – cannot be rewritten in a manifestly conservative form. A similar observation was made in Ref. [27], where the authors rewrote the flow equation of a similar system into a conservative part and nonconservative fluxes, which are then treated separately in the numerics.

Playing the same trick as for the flow equation of the potential and defining  $h(t, \varphi) \equiv \partial_\varphi H(t, \varphi)$ , such that

$$\begin{aligned} \partial_t h = & \frac{d}{d\varphi} \left( 2 \left( \frac{1}{2} \partial_t r_b \right) \frac{1}{(r_b + \partial_\varphi^2 U)^2} \frac{1}{r_f + H} h^2 + \right. \\ & - \left( \frac{1}{2} \partial_t r_b \right) \frac{1}{(r_b + \partial_\varphi^2 U)^2} \partial_\varphi h + \\ & \left. + 2 \left( \frac{1}{2} \partial_t r_f \right) \frac{1}{r_b + \partial_\varphi^2 U} \frac{1}{(r_f + H)^2} h^2 \right), \end{aligned} \quad (38)$$

does indeed not lead to the desired conservative form. As one can see, the problem here is that the flux on the r.h.s. as well as the fluxes in the first lines of Eqs. (36) and (37) still depend on  $H$ , which is no longer the variable that is evolved in the equation, but has to be reconstructed from  $h$  via integration over the spatial domain or a constraint equation. Hence, the problem formally turned into an integro-differential equation, which prevents us from directly applying techniques developed in previous works and is in general an involved numerical

problem.

In our previous works and the works of colleagues, where RG flow equations were already analyzed using (computational) fluid dynamics, the respective PDEs were studied in their conservative form (or forms that are close to conservative forms). This drastically simplifies the search for suitable numerical methods as well as their applicability, because lots of numerical schemes are designed for (hyperbolic/parabolic) conservation laws, *e.g.*, finite volume methods, discontinuous Galerkin methods, *etc.* [85–88]. As already mentioned, for flow equations involving field-dependent Yukawa couplings [27, 28, 84, 89], this is not always possible and similar issues arise for flow equations of field-dependent wave-function renormalizations in higher-dimensional systems [48, 56, 90–94]. Consequently, we deemed it necessary to develop a new understanding/interpretation of the respective RG flow equation paired with adequate numerical methods based on the resulting structural insights. In Section II B we already established the interpretation of the flow Eq. (7) as a functional (infinite-dimensional), viscous HJB Eq. (9), which is central for our practical developments in the following. In the next Section IV D we will elaborate on the practical implications of this structural insight and introduce a suitable numerical scheme based on it.

#### D. FRG flow equations as coupled viscous Hamilton-Jacobi systems

In order to explicitly introduce our new ideas for the (numerical) solution of the FRG flow equations, let us slightly rearrange Eqs. (34) and (37) in their primitive form,

$$\partial_t M - \frac{\partial_t r_b}{(r_b + M)^3} (\partial_\varphi M)^2 + \frac{2 \partial_t r_f}{(r_f + H)^3} (\partial_\varphi H)^2 = - \frac{\frac{1}{2} \partial_t r_b}{(r_b + M)^2} \partial_\varphi^2 M + \frac{\partial_t r_f}{(r_f + H)^2} \partial_\varphi^2 H, \quad (39)$$

$$\partial_t H - \frac{1}{r_b + M} \frac{1}{r_f + H} \left( \frac{\partial_t r_b}{r_b + M} + \frac{\partial_t r_f}{r_f + H} \right) (\partial_\varphi H)^2 = - \frac{\frac{1}{2} \partial_t r_b}{(r_b + M)^2} \partial_\varphi^2 H, \quad (40)$$

and compare these equations to the standard form of (nonautonomous) (viscous) Hamilton-Jacobi (HJ)-(Bellman)-type problems introduced in Section II,

$$\partial_t u + \mathcal{H}(t, \vec{x}, u, \vec{\nabla}_x u) = \varepsilon \Delta u. \quad (41)$$

Clearly, the RG flow equations are each of rather similar form, where the terms on the left hand side (l.h.s.) play the role of the respective Hamiltonians and the terms on the r.h.s. are the diffusion terms with more general diffu-

sion coefficients.<sup>14</sup> HJ-(Bellman)-type problems appear in many areas of physics, but also in the context of finance, optimal control/transport, and many other fields. A first systematic concept of their solution (originally in the absence of the diffusion term) was developed by

<sup>14</sup> The rightmost diffusion-term  $\propto \partial_\varphi^2 H$  in the PDE (39) for  $M$  has negative coefficient. This is not a problem, because it factually acts like a source in the evolution of  $M$  and does not lead to instabilities. The same applies to the last term  $\propto (\partial_\varphi H)^2$  on the l.h.s. of Eq. (39).

Crandall and Lions [95] in terms of so-called viscosity solutions. This was generalized by Jensen [96] to the static second-order nonlinear degenerate elliptic PDEs of the form<sup>15</sup>

$$F(x, u, \vec{\nabla}u, \Delta u) = 0. \quad (42)$$

According to Barles [97] also parabolic/first-order evolution equations like the viscous HJ equation (41) and our RG flow equations can be considered as degenerate elliptic for  $\varepsilon \geq 0$ , which allows to find viscosity solutions. Without going too much into the mathematical details, which is beyond the scope of this work, let us briefly try to sketch the notion of viscosity solutions and their connection to weak and entropy solutions of conservation laws.

First, we recapitulate the difference between a strong and a weak solution of a PDE. A strong solution is a function that satisfies the PDE pointwise, while a weak solution is a function that satisfies the PDE in a distributional sense. A weak solution is a solution of the integral form of the equation and is often obtained by multiplying the PDE with a test function and integrating over the domain. This allows to relax the requirements on the differentiability of the solution and to consider a larger class of functions, such as functions with nonanalytic structures. Since nonlinear PDEs in general tend to form nonanalyticities in the solution, weak solutions are often the only practically relevant solutions.

Second, weak solutions are not unique and one has to impose additional conditions to obtain a unique solution. One way to do this is to consider entropy solutions, which are weak solutions that satisfy the entropy condition. It ensures that entropy – ideally defined from physics considerations – is non-decreasing. This implies that the solution is stable under small perturbations. It further singles out the correct physical solution for shocks via the Rankine-Hugoniot condition. For conservation laws, the entropy condition is often formulated in terms of the entropy flux and the entropy production, which have to satisfy certain inequalities [85, 86]. Though, usually it is hard or not clear, how to find a suitable entropy for a given conservation law and the entropy condition is not always applicable. Still, decent numerical schemes for conservation laws converge to the entropy solution, even if the entropy is not known, because they usually introduce a small amount of numerical diffusion. Convergence, however, is only achieved for numerical schemes that are based on the conservative form of the PDE.

Third, a viscosity solution is a concept that was developed to find a unique and stable solution to degenerate elliptic PDEs and HJ-(Bellman)-type problems that are in nonconservative form. They are defined in terms of the comparison principle, which states that the solution

is the largest subsolution and the smallest supersolution of the PDE. In general, viscosity solutions do not have to be smooth and can have nonanalyticities and singularities and can therefore be regarded as a generalization of weak solutions.

The connection between these concepts is that both, entropy and viscosity solutions, emerge as the unique and physically meaningful solutions. Oftentimes this is practically achieved with vanishing viscosity methods (especially when an entropy is not known for conservation laws): One adds a small diffusion term to the PDE by hand or via numerical diffusion of the discretization scheme and then takes the limit of the diffusion coefficient to zero and  $\Delta x \rightarrow 0$ . For conservation laws, this is the Lax-Friedrichs method, which is used to stabilize and single out the correct numeric solution also for shocks. For HJ-type problems, this is the vanishing viscosity method of Crandall and Lions. In both cases, the underlying idea is that the diffusion term regularizes the PDE and turns it into a parabolic problem with a unique smoothed solution. Then, in one or the other way, the limit of the diffusion coefficient to zero is taken, which defines the unique solution of the original PDE. For some PDEs, such as Burgers equation, there exists a formulation in terms of a conservation law as well as a formulation in terms of a HJ-type problem and entropy and viscosity solutions are equivalent [98]. The same seems to be the case for the flow equation for the effective potential alone. Maybe, recent developments, see Ref. [99] and Refs. therein, might even help to identify a suitable entropy for FRG problems.

However, it is important to note that for PDEs that cannot be converted into a conservative form, such as general HJ-type problems, the viscosity solution is only unique in the sense that it is unique for a particular choice of artificial diffusion. This implies that the numeric solution of a HJ-problem that is dominated by the advection terms and has nonanalyticities in the solution depends on the choice of the numeric scheme, *e.g.*, the choice of limiter functions. For the present FRG problems, however, there are always diffusive terms – the tadpole contributions, which gives hope that the solution is unique and stable. This is also expected, because the solution is in general also obtainable from the path integral, which, in the presence of sufficient regularization, should mean that it exists and is unique.

Let us discuss this in more detail for the full FRG problem. Here, of course, things are more involved, because we have a dynamical system with time-dependent coefficients. However, what the FRG flow equations actually seem to do is very similar to the vanishing viscosity method – but automatically and in a self-consistent way. As long as and wherever the diffusion coefficients are positive, the flow equations are parabolic and the solution should be unique. However, for late times, where  $\partial_t r_{b/f}$  and  $r_{b/f}$  both tend to zero, we have to distinguish between two different scenarios:

1. Wherever the denominator of the diffusion coefficient

<sup>15</sup> In fact, FRG flow equations in higher spacetime dimensions in the fixed-point limit are of this type.



cient does not approach its pole, the diffusion term vanishes and the flow approaches its viscosity solution. The reason is that also the coefficients in front of the advective terms (first-derivative-square terms in the Hamiltonian) approach zero and the dynamic overall stops.

2. If the denominators in the diffusion coefficient as well as in the prefactors of the advective terms approach their poles, there is in general a lot of dynamics and velocities are high. Even in the presence of diffusion we expect shocks to form, because the number of propagators in advective terms is larger than in the diffusion terms. However, the presence of diffusion should ensure that the solution is unique and stable and converges against the viscosity solution.

The interesting points in the solution of the FRG flow equations are those points, where the behavior changes, *i.e.*, where  $M$  and  $H$  change their sign as a function of  $\varphi$  while the regulator  $r_{b/f}$  approaches zero. Here, we expect the solution to form nonanalyticities and singularities. Another region, where we expect nonanalytic behavior is, where the diffusion coefficient in Eq. (40) vanishes for late times (positive  $M$ ), while  $r_f + H$  approaches zero (negative  $H$ ). However, also here, we expect a self-regulation of the system towards the correct solution.

We close the present discussion with three remarks:

1. In general, nonanalytic behavior is also physically totally expected, if one considers for example the flow equation of the effective potential of a  $\mathbb{Z}_2$ -model in its symmetry broken regime in nonzero spacetime dimensions. Here, the IR potential consists of a flat plateau and a steep slope starting at the field-expectation value. For  $M = \partial_\varphi^2 U$  this implies that it takes negative values for small  $|\varphi|$  and positive values for large  $|\varphi|$  during the flow and approaches the region with  $M = 0$  (the plateau of the potential) from below.

Another scenario, where nonanalytic behavior is totally expected is in the presence of a chemical potential that introduces an external shock into the system.

2. The attentive reader might have noticed that our analysis of the FRG flow equations in terms of coupled HJ-type problems is based on the flow equations for the field-dependent two-point functions. One might therefore ask, if this structure and analogy is more general. Indeed, as already mentioned in Section II B, for full field-dependent FRG flow equations that are extracted from the two-point vertex function (*e.g.*, the field-dependent wave-function renormalization), the same structure can be found. The reason is rather simple: Diagrammatically one always has contributions from

tadpole-type diagrams, which are proportional to second derivatives of vertices and are therefore diffusion type operators, and contributions from self-energy diagrams, which are proportional to two first derivatives of vertices and are therefore advective operators. We come back to this point in Section VII in the context of applications to higher-dimensional systems.

3. Before we turn to the explicit numerical scheme let us return to the remark that the flow equation for the effective potential alone can also be rewritten as a conservation law. Indeed, we experienced that it is numerically advantageous in terms of convergence and stability to treat the purely bosonic contributions in the flow equation for the field-dependent bosonic mass conservatively, while the fermionic source-type contribution are handled within the HJ framework that is also used for the Yukawa coupling.

## V. NUMERICAL SCHEME

Having reformulated the PDE system of the FRG flow equations as a system of coupled viscous HJ-type problems, we can now think about suitable numerical methods to solve these. Since we are not experts on the construction of numerical methods, we follow our own repeatedly stated advise and search for and adapt well-tested methods from the literature.

Hence, we suggest to use a high-resolution semi-discrete central scheme for (viscous) HJ equations that was developed by Kurganov and Tadmor [25]. This scheme shares some similarities with the semi-discrete Monotonic Upstream-Centered Schemes for Conservation Laws (MUSCL) that we previously used for the solution of local potential approximation (LPA) flow equations in their conservative formulation [2–6, 42, 47, 49] as well the scheme presented in Appendix B of Ref. [100]. The diffusive part of the former scheme is still used for the conservative contributions to the flow equation of the field-dependent boson mass in this work.

However, before we briefly present the scheme and all necessary expressions for an implementation, we introduce the following notation for partial derivatives:

$$u_t \equiv \partial_t u(t, x), \quad (43)$$

$$u_x \equiv \partial_x u(t, x), \quad (44)$$

$$u_{xx} \equiv \partial_x^2 u(t, x). \quad (45)$$

In their publication, Kurganov and Tadmor consider problems of the form

$$u_t + \mathcal{H}(u_x) = \varepsilon u_{xx}, \quad (46)$$

with additional initial and boundary conditions. As already discussed at the end of the previous section, our flow equations are more general, which calls for several modifications of the original scheme. However, let us first present the original scheme and then discuss the necessary modifications afterwards.

### A. Original semi-discrete scheme

Most of the finite-volume and finite-element schemes for PDEs are based on a multi-step procedure: The spatial domain is subdivided into cells and the solution within each cell is approximated by a low-order polynomial. This approximated solution is what is actually evolved by the time stepper. Then, for each time step the fluxes at the cell interfaces have to be computed. To this end, it is necessary to reconstruct the solution at the cell interfaces or some staggered grid. Usually, this reconstruction involves a limiting procedure of the gradients of the solution to avoid spurious oscillations. Another limiting procedure is applied to the fluxes, which involves an estimation of the local wave speeds. Finally, the fluxes are computed and the solution is updated. The entire procedure is, however, strongly dependent on the conservative form of the PDE.

Nevertheless, also the high-resolution semi-discrete central scheme of Kurganov and Tadmor – in the following Kurganov-Tadmor-Hamilton-Jacobi (KT-HJ)-scheme – is based on the same concepts. First, one dis-

cretizes the solution on an equidistant grid

$$x_j = x_0 + j \Delta x \quad (47)$$

with  $j = 0, \dots, N$ ,  $x_{\min} = x_0$ ,  $x_{\max} = x_0 + N \Delta x$ , and  $\Delta x = \frac{x_{\max} - x_{\min}}{N}$ ,

$$u_j = u(x_j, t). \quad (48)$$

Here,  $x_{\min}$  is the left boundary of the spatial domain and  $x_{\max}$  the right boundary and in total there are  $N+1$  grid points. Additionally, one defines midpoints between the grid points – the staggered grid,

$$x_{j+\frac{1}{2}} = x_j + \frac{1}{2} \Delta x, \quad (49)$$

which is the analogue to the cell interfaces in the finite-volume method. Instead of reconstructing the solution itself on  $x_{j+\frac{1}{2}}$  using slope-limiters for  $u_x$ , the KT-HJ-scheme is based on the use of limiters on the level of the second derivatives of the solution,  $u_{xx}$ . Hence, using the definition of the first-order forward and backward differences

$$\frac{(\Delta u)_{j+\frac{1}{2}}}{\Delta x} \equiv \frac{u_{j+1} - u_j}{\Delta x}, \quad (50)$$

one can estimate the forward and backward reconstruction of the first derivatives by

$$u_{x,j}^{\pm} = \frac{(\Delta u)_{j\pm\frac{1}{2}}}{\Delta x} \mp \frac{(\Delta u)'_{j\pm\frac{1}{2}}}{2\Delta x}, \quad (51)$$

Here,  $(\Delta u)'_{j\pm\frac{1}{2}}$  is the limited second derivative of the solution on the midpoints.

$$(\Delta u)'_{j+\frac{1}{2}} = \min\text{mod}\left(\theta (\Delta u_{j+\frac{3}{2}} - \Delta u_{j+\frac{1}{2}}), \frac{1}{2} (\Delta u_{j+\frac{3}{2}} - \Delta u_{j-\frac{1}{2}}), \theta (\Delta u_{j+\frac{1}{2}} - \Delta u_{j-\frac{1}{2}})\right), \quad \theta \in [1, 2]. \quad (52)$$

Smaller values of  $\theta$  lead to more dissipative schemes, while larger values of  $\theta$  lead to less dissipative schemes. In particular, we use the minmod limiter with  $\theta = 1$  for this work as in the original publication, *i.e.*,

$$\min\text{mod}(x_1, x_2, \dots) = \quad (53)$$

$$= \begin{cases} \min_j \{x_j\}, & \text{if } \forall j : x_j > 0, \\ \max_j \{x_j\}, & \text{if } \forall j : x_j < 0, \\ 0, & \text{otherwise.} \end{cases}$$

Additionally, we test the superbee and MUSCL<sup>16</sup> limiters [87, 101], for which Eq. (52) may be expressed As

$$(\Delta u)'_{j+\frac{1}{2}} = \quad (54)$$

$$= (\Delta u_{j+\frac{3}{2}} - \Delta u_{j+\frac{1}{2}}) \phi\left(\frac{\Delta u_{j+\frac{1}{2}} - \Delta u_{j-\frac{1}{2}}}{\Delta u_{j+\frac{3}{2}} - \Delta u_{j+\frac{1}{2}}}\right),$$

with

$$\phi_{\text{superbee}}(r) \equiv \max(0, \min(1, 2r), \min(2, r)), \quad (55)$$

<sup>16</sup> The MUSCL limiter in the present context is sometimes also called monotonized central (MC) limiter.

$$\phi_{\text{MUSCL}}(r) \equiv \max(0, \min(2, 2r, (1+r)/2)). \quad (56)$$

While the minmod limiter is the most dissipative one, the superbee limiter is the least dissipative second-order accurate limiter that is total variation diminishing. The MUSCL limiter is a compromise in between the two, which has the advantage of limiting symmetrically in and opposed to the velocity direction. As an additional ingredient one needs a local estimate of the wave speeds. This is given by

$$a_j = \max(|\mathcal{H}'(u_{x,j}^+)|, |\mathcal{H}'(u_{x,j}^-)|), \quad (57)$$

where  $\mathcal{H}'$  is the derivative of the Hamiltonian with respect to the first derivative of the solution – the canonical momentum. This is rather intuitive to understand, because the coefficient in front of a  $u_x$  term can be considered as the velocity and the respective term as an advection term. Lastly, one needs a discretization of the diffusion/Laplace operator. Since the remaining scheme is of second order in  $\Delta x$  it is natural to use

$$u_{xx,j} = \frac{u_{j+1} - 2u_j + u_{j-1}}{\Delta x^2}. \quad (58)$$

The full semi-discrete scheme is then given by the following equation,

$$u_{t,j} = - \frac{\mathcal{H}(u_{x,j}^+) + \mathcal{H}(u_{x,j}^-) - a_j(u_{x,j}^+ - u_{x,j}^-)}{2} + \varepsilon \frac{(u_{j+1} - 2u_j + u_{j-1})}{\Delta x^2}. \quad (59)$$

Here, however, we abstain from further details of its derivation and refer to the original publication [25] for any details. Before discussing our modifications let us remark that there exists also a first-order accurate version of the KT-HJ-scheme, which is also presented in the original publication. Furthermore, note that due to its semi-discrete nature, the scheme can be combined with any time-stepping method. For this work, we use the implicit time steppers in terms of the IDA<sup>17</sup> method in NDSolve [102] from *Mathematica 14.2* [103] with `PrecisionGoal` and `AccuracyGoal` of  $\geq 10$  and  $\leq 14$ . Time-stepping is not a focus of this work and we refer the interested reader to the excellent Ref. [57] discussing the issue in the context of FRG in detail. Let us also remark at this point that we crosschecked our implementation with the sample cases from the original publication and found good agreement.

<sup>17</sup> We use as options for IDA a `MaxDifferenceOrder` of 5 and `Newton` as an `ImplicitSolver` with `LinearSolverMethod` `Band` and total `BandWidth` of 11 for the two component systems considered in this work. To use such a sparse/band solver it is imperative to implement the discretized PDE systems in ‘point-major’ order ( $[\dots, u_{j,1}, u_{j,2}, \dots]$ ) as opposed to ‘component-major’ order ( $[u_{0,1}, \dots, u_{N,1}, u_{0,2}, \dots, u_{N,2}]$ ), cf. Section V B. The use of a sparse/banded linear solver over a dense one significantly increases the performance/decreases the runtime especially for systems with a large number  $N$  of cells.

## B. Modifications of the KT-HJ scheme for FRG flow equations

For this work, we consider the following modifications of the original KT-HJ-scheme for the solution of the FRG flow equations.

1. We allow for an additional dependence of the Hamiltonian on the time  $t$  and  $u$  itself,

$$\mathcal{H}(u_x) \Rightarrow \mathcal{H}(t, u, u_x), \quad (60)$$

such that

$$\mathcal{H}(u_{x,j}^\pm) \Rightarrow \mathcal{H}(t, u_j, u_{x,j}^\pm), \quad (61)$$

and the new estimate of the wave speeds is given by

$$a_j = \max(|\mathcal{H}'(t, u_j, u_{x,j}^+)|, |\mathcal{H}'(t, u_j, u_{x,j}^-)|). \quad (62)$$

The reason, why we believe that this modification is still valid, is that  $t$  and  $u$  solely appear in prefactors of  $u_x^2$ -terms in the Hamiltonian and there is no other  $u_x$ -dependence.

2. The same applies to the coefficient of the diffusion terms,  $\varepsilon$ ,

$$\varepsilon \Rightarrow \varepsilon(t, u), \quad (63)$$

or on a discrete level

$$\varepsilon \Rightarrow \varepsilon_j = \varepsilon(t, u_j). \quad (64)$$

3. In addition, we consider systems of  $f \in \mathbb{N}$  coupled Hamilton-Jacobi-type PDEs, such that Eq. (46) is replaced by

$$\vec{u}_t + \vec{\mathcal{H}}(t, \vec{u}, \vec{u}_x) = \mathcal{E}(t, \vec{u}) \cdot \vec{u}_{xx}. \quad (65)$$

Hereby,

$$\vec{u} = (u_1, \dots, u_f)^T, \quad (66)$$

and

$$\vec{\mathcal{H}}(t, \vec{u}, \vec{u}_x) = \begin{pmatrix} \mathcal{H}_1(t, \vec{u}, \vec{u}_x) \\ \vdots \\ \mathcal{H}_f(t, \vec{u}, \vec{u}_x) \end{pmatrix}, \quad (67)$$

and  $\mathcal{E}(t, \vec{u})$  is matrix valued. On the discretized level the diffusion term on the r.h.s. generalizes trivially. A good – the best possible – estimate for the local wave speed is very important for convergence and numerical performance. We tested various approaches and have come to the conclusion that the most promising approach is to estimate the local velocities separately for each component of the system by only studying the respective Hamiltonian and its dependence on the first derivatives,

$$a_{j,m,n} = \max_{\vec{u}_{x,j} \in \{\vec{u}_{x,j}^+, \vec{u}_{x,j}^-\}} \left| \frac{\partial \mathcal{H}_m(t, \vec{u}_j, \vec{u}_{x,j})}{\partial u_{x,j,n}} \right|, \quad (68)$$

where  $j$  labels the spatial grid point,  $m$  the component of the Hamiltonian (67), and  $n$  the component of the first derivative  $\vec{u}_x$ . (Another possible

approach can be found in Ref. [100].) Hence, the advective term in Eq. (59) for the  $m$ -th field generalizes to

$$u_{t,j,m} = - \frac{\mathcal{H}_m(t, \vec{u}_j, \vec{u}_{x,j}^+) + \mathcal{H}_m(t, \vec{u}_j, \vec{u}_{x,j}^-) - a_{j,m,n} (u_{x,j,n}^+ - u_{x,j,n}^-)}{2} + \dots, \quad (69)$$

where summation over  $n$  is implied.

Combining this adapted KT-HJ with a conservative treatment for the bosonic contributions to the field-dependent boson mass using the diffusion term of the Kurganov-Tadmor (KT) scheme has proven to be the most promising numerical implementation. To be explicit, for Eqs. (39) and (40) we have

$$\mathcal{H}_1 = \frac{2 \partial_t r_f}{(r_f + H)^3} (\partial_\varphi H)^2, \quad (70)$$

$$\mathcal{H}_2 = - \frac{1}{r_b + M} \frac{1}{r_f + H} \left( \frac{\partial_t r_b}{r_b + M} + \frac{\partial_t r_f}{r_f + H} \right) (\partial_\varphi H)^2, \quad (71)$$

such that the velocities are

$$a_{1,1} = 0, \quad (72)$$

$$a_{1,2} = 4 \frac{\partial_t r_f}{(r_f + H)^3} (\partial_\varphi H), \quad (73)$$

$$a_{2,1} = 0, \quad (74)$$

$$a_{2,2} = -2 \frac{1}{r_b + M} \frac{1}{r_f + H} \left( \frac{\partial_t r_b}{r_b + M} + \frac{\partial_t r_f}{r_f + H} \right) \partial_\varphi H, \quad (75)$$

because the PDE (39) for  $M$  reads in semi-conservative form

$$\begin{aligned} \partial_t M + \frac{2 \partial_t r_f}{(r_f + H)^3} (\partial_\varphi H)^2 &= \\ &= \frac{\partial_t r_f}{(r_f + H)^2} \partial_\varphi^2 H + \frac{\partial}{\partial \varphi} \left( - \frac{\frac{1}{2} \partial_t r_b}{(r_b + M)^2} \partial_\varphi M \right). \end{aligned} \quad (76)$$

For the conservative part, we use the discretization of the diffusion term as in KT scheme [26], where

$$u_t = \dots + \partial_x Q(t, u, u_x) \quad (77)$$

is discretized as follows

$$u_{t,j} = \dots + \frac{1}{\Delta x} (P_{j+\frac{1}{2}} - P_{j-\frac{1}{2}}), \quad (78)$$

$$P_{j+\frac{1}{2}} = \frac{1}{2} \left( Q(t, u_j, \frac{u_{j+1} - u_j}{\Delta x}) + Q(t, u_{j+1}, \frac{u_{j+1} - u_j}{\Delta x}) \right).$$

Note, however, that also treating the entire coupled PDE system as a pure diffusive HJ problem and using solely the here presented KT-HJ scheme with the spectral radius as an estimate for the  $a_j$  lead to satisfactory results for most problems.

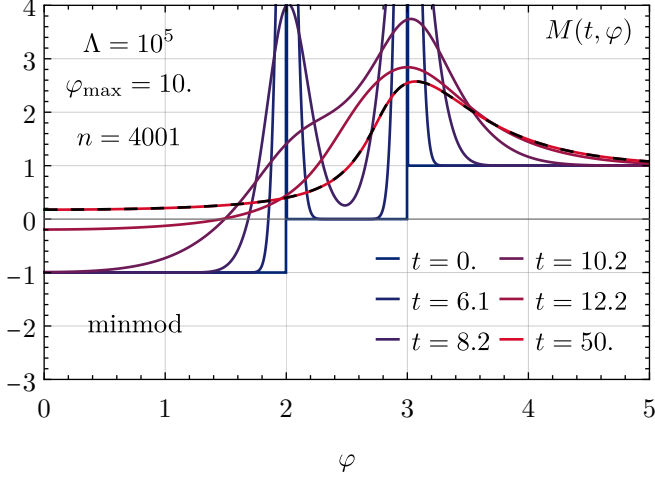
### C. Boundary conditions

Lastly, we have to provide boundary conditions for the flow equations as well as their discretization. Otherwise a PDE problem is ill posed. Within the numerical schemes under consideration, spatial boundary conditions are usually implemented via so-called ghost cells/points, which are located outside the computational domain. The number of ghost cells/points depends on the order of the spatial discretization scheme and is two for the KT-HJ scheme, because it is a second-order accurate scheme. For a detailed discussion of this topic, we refer to Ref. [2]. Here, we only provide a short version that is used in the following.

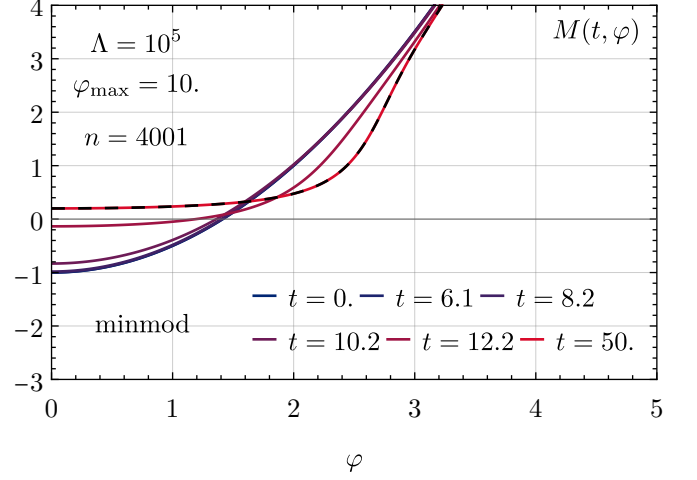
In fact, our PDE problem is defined on  $\mathbb{R}$ , such that there are actually no spatial boundaries and the initial condition suffices to have a well-posed problem. However, to numerically solve the PDEs, we have to discretize the spatial domain and therefore have to use a finite computational domain. Instead of mapping the infinite domain to a finite one, we truncate the domain at some large  $\pm \varphi_{\max}$ , where we can assume that the solution does not change anymore or the change is almost trivial due to the shape of the PDEs and initial conditions. At this artificial boundary, we simply use linear extrapolation<sup>18</sup> of the solution to ghost cells  $\varphi_N$  and  $\varphi_{N+1}$  outside the computational domain, *e.g.*,

$$u_{N+1} = 2u_N - u_{N-1}, \quad (79)$$

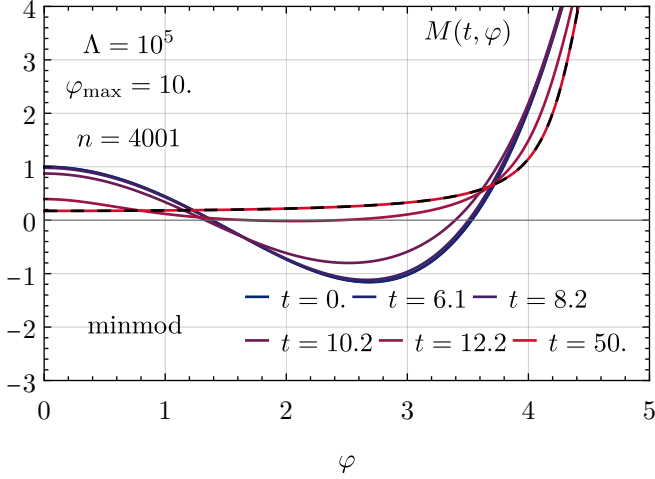
<sup>18</sup> Extrapolation using the asymptotics of the UV initial condition can be a suitable improvement over linear extrapolation for certain problems.



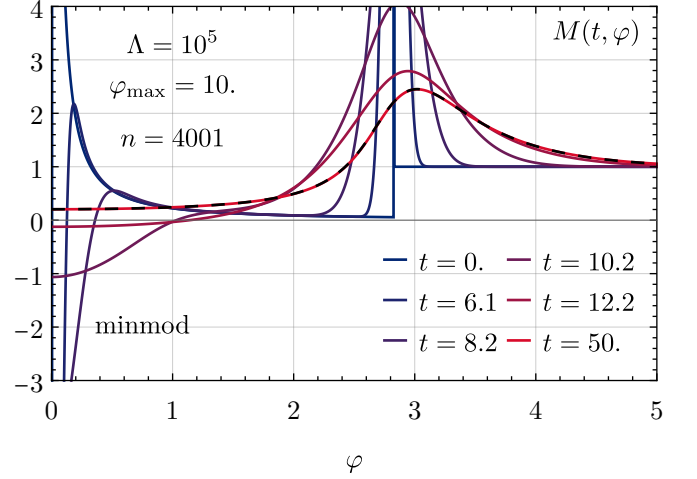
(a) For UV potential (85).



(b) For UV potential (86).



(c) For UV potential (87).



(d) For UV potential (88).

FIG. 1. Test 0: RG flow of  $M(t, \varphi)$  (colored) and the exact IR reference solution (dashed, black).

$$u_{N+2} = 3u_N - 2u_{N-1}, \quad (80)$$

where  $N$  is the last grid point of the computational domain, because the first computational grid point is denoted as  $\varphi_0$ . This boundary condition is used for both fields  $M$  and  $H$ .

However, due to the  $\varphi \rightarrow -\varphi$  symmetry of the entire problem, we can restrict our computational domain to  $\varphi \in [\varphi_{\min} = 0, \varphi_{\max} = \varphi_N]$ . In consequence, we have to provide another boundary condition at  $\varphi = 0$ , which is

$$u_{-1} = u_1, \quad u_{-2} = u_2, \quad (81)$$

without constraints on  $u_0$  for both functions  $M$  and  $H$ .

## VI. TESTS AND DISCUSSION IN ZERO DIMENSIONS

Next, we turn to some explicit tests of the newly introduced interpretation of the FRG problem as a HJ-type system and the numerical KT-HJ scheme. In particular, we consider different test cases (initial conditions), which challenge different aspects of the numerical scheme or simulate various physical situations. Besides the explicit tests, we also discuss the modeled situations on a qualitative level.

As a quantitative measure of the quality of the numerical scheme we mainly use the  $L^1$  and  $L^\infty$  norm/error between the numerical solution from the modified KT-HJ scheme and the exact solution generated via Eqs. (25) and (26). (Note, however, that also the “exact” reference solution involves comparatively small numerical error, which we tried to minimize but could not completely



avoid due to a necessary interpolation of the discrete  $J$ - $\varphi$ -data and the numerical integrations.) To be explicit, the  $L^1$  and  $L^\infty$  norm/error is defined as

$$L_1(u) = \frac{1}{J} \sum_{j=0}^J |u_{\text{KT-HJ},j} - u_{\text{exact},j}|, \quad (82)$$

$$L_\infty(u) = \max_{j \in \{0, \dots, J\}} |u_{\text{KT-HJ},j} - u_{\text{exact},j}|, \quad (83)$$

where  $u \in \{M, H\}$  and  $u_{\text{KT-HJ},j}$  and  $u_{\text{exact},j}$  are the numerical and exact solution at grid point  $j$ , respectively, and  $J$  is the number of grid points included. We choose  $J = \lfloor N/2 \rfloor$ , where  $N$  is the number of grid points in the computational domain  $[\varphi_{\min} = 0, \varphi_{\max}]$ . The latter is much larger than the region with nontrivial dynamics. The reason that we do not use all grid points for benchmarking is that we do not want to include possible numerical errors from the artificial boundary conditions at  $\varphi_{\max}$  and focus on the  $\varphi$ -values in the “physical” region. For initial conditions for  $M$  and  $H$  that are nonlinear for large  $|\varphi|$  one finds some nonnegligible boundary effects close to  $\varphi_{\max}$ . However, if  $\varphi_{\max}$  is sufficiently large, these errors do not propagate at all into the physical region. This is shown in plots that present the relative error of the numerical solution to the exact solution as a function of  $\varphi$  at some resolution  $N$ ,

$$R_N(u_j) = \left| \frac{u_{\text{KT-HJ},j} - u_{\text{exact},j}}{u_{\text{exact},j}} \right|. \quad (84)$$

Furthermore, for some of the tests, it turns out that the  $L_1$  and  $L_\infty$  norms are unsuited as error measures: If the solution develops moving shocks/singularities a slight offset in the position of the shock leads to a huge error in the  $L_1$  and  $L_\infty$  norm. Hence, it is more appropriate to directly compare the numeric and the exact solution by visual inspection.

### A. Test 0: Decoupling

Let us turn to our first minimal test case, which serves as a crosscheck with our previous works that were based on the conservative form of the flow equations [2–4, 6]. To this end, we consider the purely bosonic  $\mathbb{Z}_2$ -symmetric system. This can be achieved in our model by setting the Yukawa coupling to a constant, without loss of generality (w.l.o.g.)  $H(\phi) = 1 \Rightarrow H(t, \varphi) = 1$ , and solely considering the potential for the bosonic field as being RG-time dependent. In this test case we treat the flow equation for  $M$  with the HJ scheme Eq. (59), instead of using the KT conservative formulation of Eq. (78). We tested the latter extensively in previous works [2, 3, 47]. As explicit initial conditions of our test, we choose the test potentials put forward in our previous works [2–4, 6], which were developed as challenging test cases for the numerical solution of the RG flow equations. In particular, these are

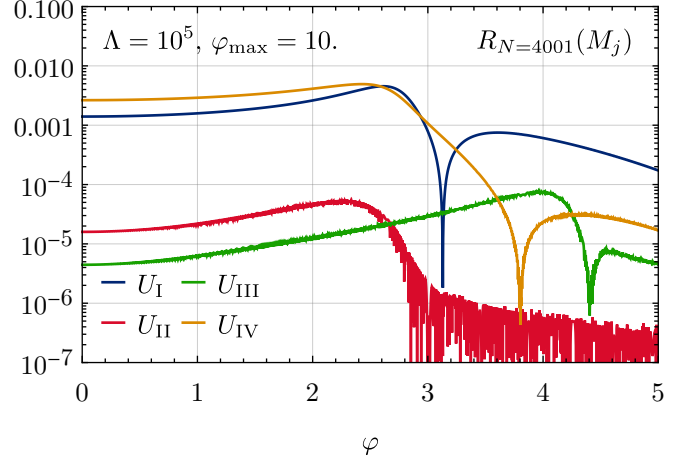


FIG. 2. Test 0: Relative error (84) of the numerical solution to the exact solution as a function of  $\varphi$  for the UV potentials (85)–(88) at a resolution of  $N = 4001$  points for  $\varphi_{\max} = 10$ .

the following four UV initial potentials:

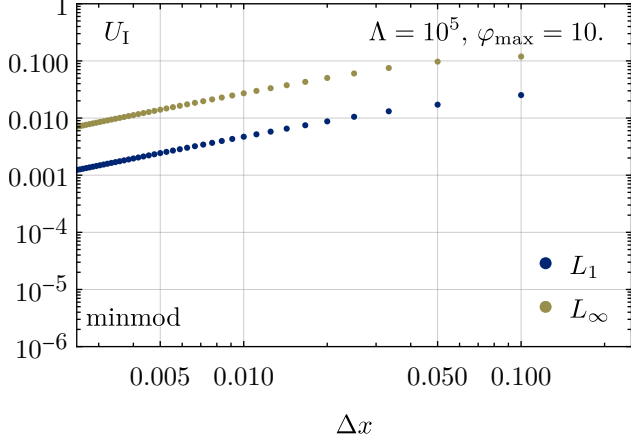
$$U_I(\phi) = \begin{cases} -\frac{1}{2} \phi^2, & \text{if } |\phi| \leq 2, \\ -2, & \text{if } 2 < |\phi| \leq 3, \\ +\frac{1}{2} (\phi^2 - 13), & \text{if } 3 < |\phi|, \end{cases} \quad (85)$$

$$U_{II}(\phi) = -\frac{1}{2} \phi^2 + \frac{1}{4!} \phi^4, \quad (86)$$

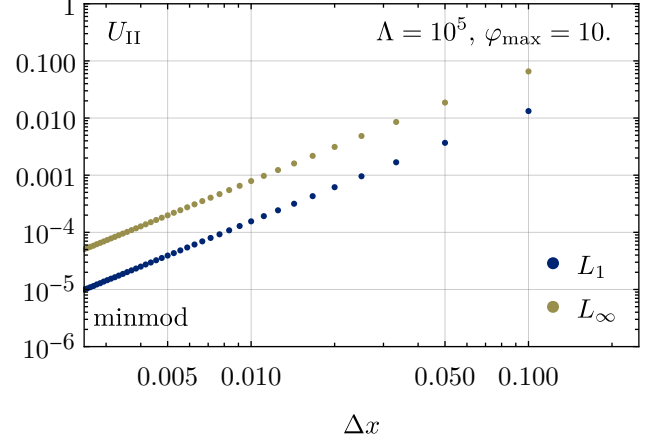
$$U_{III}(\phi) = \frac{1}{2} \phi^2 - \frac{1}{20} \phi^4 + \frac{1}{6!} \phi^6, \quad (87)$$

$$U_{IV}(\phi) = \begin{cases} -(\phi^2)^{\frac{1}{3}}, & \text{if } |\phi| \leq \sqrt{8}, \\ +\frac{1}{2} \phi^2 - 6, & \text{if } \sqrt{8} < |\phi|. \end{cases} \quad (88)$$

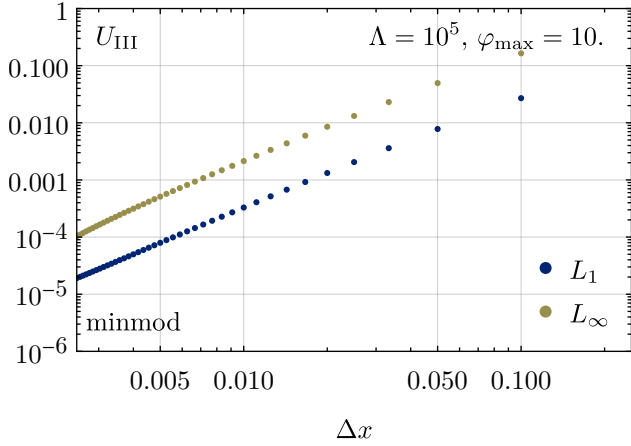
For a detailed discussion on their choice and the simulated dynamics and challenges, we refer to Ref. [2]. Here, let us simply present the corresponding RG flows of  $M(t, \varphi)$  in Fig. 1. Already on a qualitative level, we observe from these plots that the numerical solution from the KT-HJ scheme, shown in red, is in very good agreement with the exact IR reference solution, depicted as dashed black lines. In particular, we stress that despite the nontrivial shape of the initial conditions, the numerical scheme was able to handle all test cases without any problems like spurious oscillations or instabilities. The final IR times  $t = 50$  corresponds to an IR cutoff of  $r(t = 50) \simeq 10^{-17}$ , which is sufficiently small to ensure that all dynamics are frozen out, which is also confirmed by the match with the exact IR reference solution. To get a better quantitative understanding of the quality of the numerical solution, we present the relative error of the numerical solution to the exact solution as a function of  $\varphi$



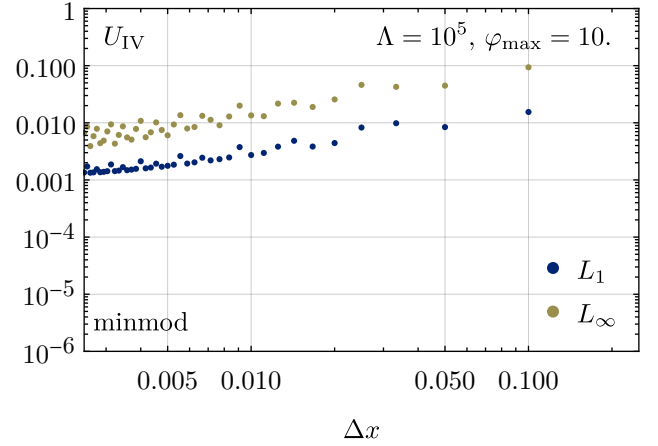
(a) For UV potential (85).



(b) For UV potential (86).



(c) For UV potential (87).



(d) For UV potential (88).

FIG. 3. Test 0:  $L^1$  and  $L^\infty$  norm, see Eqs. (82) and (83), of the deviation between the numerical and the exact solution on the computational domain as a function of the spatial resolution for the UV potentials (85)-(88).

in Fig. 2. One observes that the relative errors are always below 1% and in most cases even significantly smaller at a spatial resolution of  $\Delta x = 0.0025$ . The  $\varphi$ -region, where the deviations of the numerical from the exact solution are largest are always close to those points, where most of the dynamics takes place, *e.g.*, where shocks are smeared out *etc.*. Even more interesting than the pointwise relative error at fixed resolution is the scaling of the error with the resolution. This is shown in Fig. 3, where we present the  $L^1$  and  $L^\infty$  norm of the deviation between the numerical and the exact solution as a function of the spatial resolution. For all test cases one finds that the error decreases with increasing resolution as should be the case. Furthermore, the  $L^\infty$  error is always larger than the  $L^1$  error, which is expected, because the  $L^\infty$  error is the maximum error over all grid points, while the  $L^1$  error is the average error over all grid points. Hence, there

are single grid points which have significantly larger error than the average error, which is already seen from Figs. 1 and 2. Note that the error scaling is always polynomial. However, it never perfectly matches the expected/ideal  $\Delta x^2$  scaling. First, it is seldomly the case that one finds perfect matching of the scaling exponent with the expected one, which explains Figs. 1b and 1c, where the exponent is close to 2 but not exactly 2. For the other two test cases, Figs. 1a and 1d, the scaling is actually closer to  $\Delta x^1$ . Also this is rather natural, because we already imprinted nonanalytic structures in the initial condition. In the vicinity of nonanalyticities it is rather natural that the error scaling reduces to the one of a first-order accurate scheme. Concerning Fig. 1d, we also observe minimal ‘oscillations’ in the scaling. Here we are not sure about the reason for this behavior. However, we suspect that it is not caused by the numerical scheme

itself but by the approximation/discretization of the pole in the initial condition. Furthermore, let us mention that exchanging the slope limiters in the KT-HJ has no effect on the results and the results are almost identical for the superbee and MUSCL limiters. Hence, we conclude that the KT-HJ scheme can be used instead of conservative schemes suggested in Refs. [2] to handle field-dependent flow equations for the second derivative of the effective potential that come as a single PDE.

### B. Test 1: Minimal test

So far, we have only considered the RG flow of the effective potential  $U(t, \varphi)$ , respectively the bosonic mass  $M(t, \varphi) = \partial_\varphi^2 U(t, \varphi)$  in a purely bosonic  $\mathbb{Z}_2$  system. Consequently, let us come to our first test case, where we also include the fermionic degrees of freedom. Hence, let us study the full PDE system Eqs. (39) and (40) for the effective potential  $U(t, \varphi)$  and the Yukawa coupling  $H(t, \varphi)$ . This time and from now on, we deploy Eq. (78) for the conservative part of the PDE for the bosonic mass  $M(t, \varphi)$ , while all other terms as well as the PDE for  $H(t, \varphi)$  are treated with the modified KT-HJ scheme. We start with a rather simple test, which we call the “minimal test” with the following initial conditions:

$$U(\phi) = \phi^2, \quad (89)$$

$$H(\phi) = 20\phi^2. \quad (90)$$

Note, that all expectation values from Section A 1 in fact boil down to the calculation of Gaussian moments, which is easily seen from Eqs. (15)–(17). In terms of an RG flow, the problem is still nontrivial and corresponds to solving a complicated PDE system. The actual RG flows of  $M(t, \varphi)$ ,  $H(t, \varphi)$ , and also  $\partial_\varphi U(t, \varphi)$ , which are obtained via the KT-HJ scheme, are shown in Fig. 4.

#### 1. Qualitative discussion

Qualitatively, one first observes perfect agreement of the numerical solution with the exact reference solutions at late RG times, which are depicted as dashed black lines and obtained via the procedure outlined in Section III B.<sup>19</sup> However, let us also inspect the actual dynamics taking place during the RG flow: We find that caused by the fermion-boson interaction the

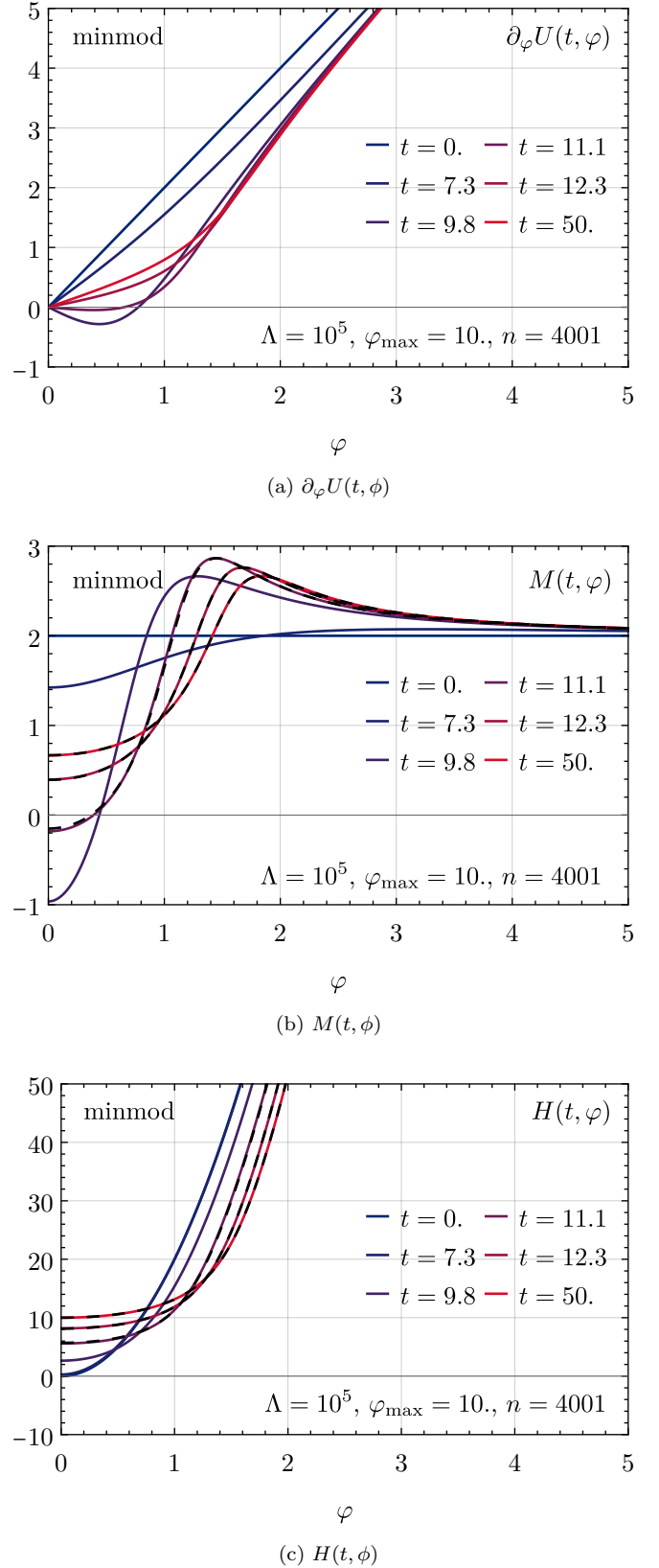
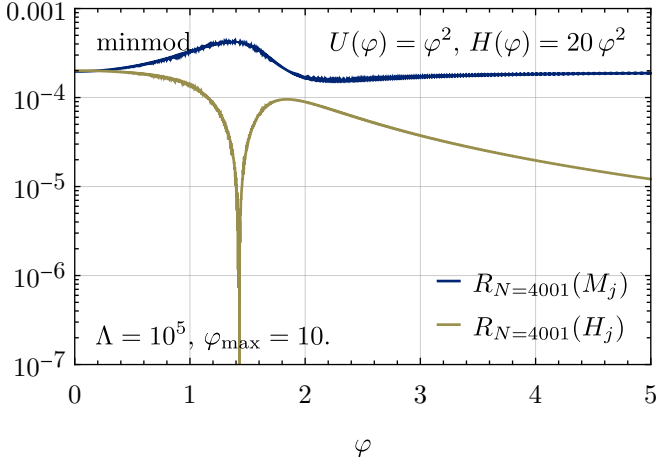
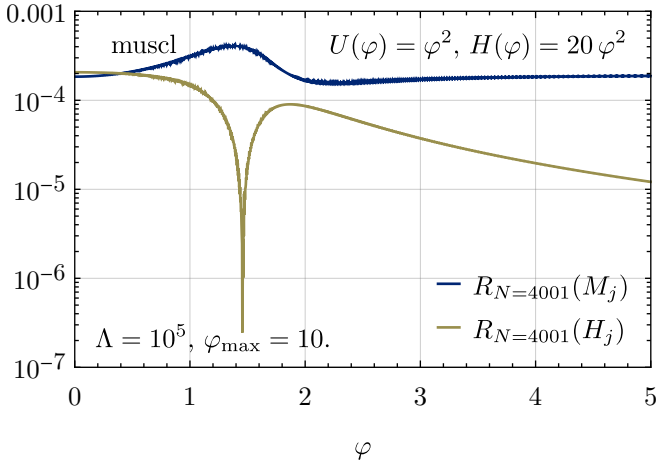


FIG. 4. Test 1: RG flow for the initial conditions (89) and (90). The exact reference solution for the last three times is shown black dashed.

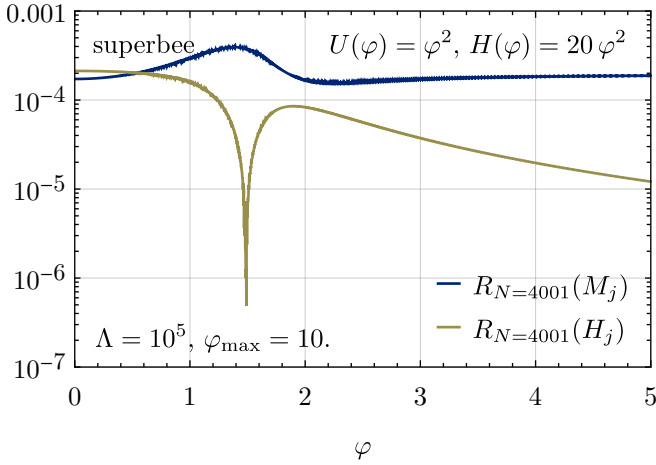
<sup>19</sup> The reason why we solely plot the exact reference solution of the latest three times is that reference solutions for earlier RG times require an excessively large domain in  $J$ -space for the Legendre transformation and the formulae from Section III B because of the large UV cutoff and there is little to learn from these curves.



(a) For the minmod limiter.



(b) For the MUSCL limiter.



(c) For the Superbee limiter.

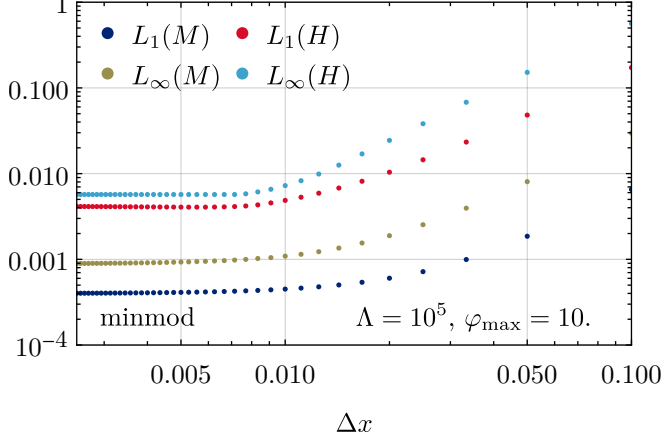
FIG. 5. Test 1: Relative error (84) of the numerical solution to the exact solution as a function of  $\varphi$  for the initial conditions (89) and (90) for different limiters at a resolution of  $N = 4001$  points with  $\varphi_{\max} = 10$ .

effective potential  $U(t, \varphi)$  develops a nontrivial minimum, which is directly seen from the zero-crossing in its derivative  $\partial_\varphi U(t, \varphi)$ , see Fig. 4a at  $t = 9.8$ . At late times, this  $\mathbb{Z}_2$ -symmetry breaking vanishes again – as expected in zero spacetime dimensions – and the potential turns convex, which is easily seen from the positivity of  $M(t, \varphi) = \partial_\varphi^2 U(t, \varphi)$  in the IR. Note that both phase transitions during the flow are of the second order. The behavior of the Yukawa coupling  $H(t, \varphi)$  during the RG flow is rather subdued in comparison. The shape changes, while it is ultimately always positive, which is expected. Still, let us stress that  $r(t) + M(t, \varphi)$  as well as  $r(t) + H(t, \varphi)$  always remain positive during the entire flow, which is a necessary condition for the well-posedness of the scale-dependent version of the effective action  $\Gamma(t, \phi, \tilde{\vartheta}, \vartheta)$  in Eq. (21) being the Legendre transform of the scale-dependent version of the Schwinger functional  $W(t, J, \tilde{\eta}, \eta)$  in Eq. (20).

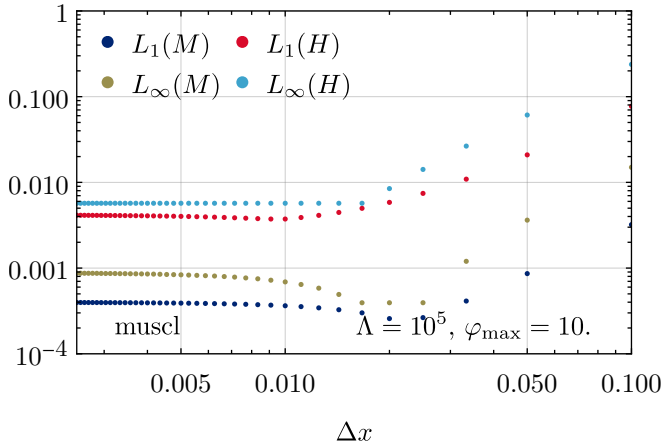
Maybe, the most interesting aspect is that the fermions dynamically acquire some mass during the flow, which manifests as a constant offset in  $H(t, \varphi)$ . Note, that in contrast to nonzero spacetime dimensions a nonzero fermion mass is not in contradiction with the  $\mathbb{Z}_2$ -symmetry restoration in the IR, because here  $H(t, \varphi)$  is in general an even function of  $\varphi$ . Before we turn to the quantitative analysis, let us mention that the strength of the symmetry breaking during the flow is controlled by the prefactor in the initial condition for  $H(t, \varphi)$  and for too small values there is no symmetry breaking and restoration at all, hence our choice of 20 in Eq. (90) to facilitate a more interesting discussion. Note, however, that the IR result is always in the symmetric phase.

## 2. Quantitative discussion

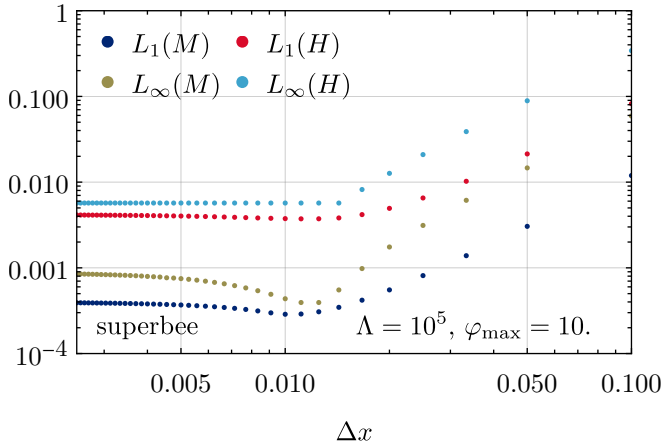
Again, let us first turn to the relative error of the numerical solution to the exact solution as a function of  $\varphi$  in Fig. 5 at constant  $\Delta x = 0.0025$  to get a first impression of the quality of the numerical solution as well as the position-dependence of the error. Overall we find that due to the rather smooth dynamics of the RG flow the relative error is very small for all  $\varphi$ -values, below 0.1% in fact. There are small spatial modulations in the relative error and the largest error is again found in the vicinity of the region in field space with the strongest dynamic during RG flow. Note, that the relative error for  $H(t, \varphi)$  is always smaller than the one of  $M(t, \varphi)$ . We speculate that this is due to the fact that the PDE of  $H(t, \varphi)$  does not depend on derivatives of  $M(t, \varphi)$  such that the velocity estimates (68) are slightly more accurate. Next, we turn to the scaling of the error with the resolution in Fig. 6. For both  $L$  norms and for both fields  $M(t, \varphi)$  and  $H(t, \varphi)$  we find that the error decreases with increasing resolution and the scaling is indeed almost  $\Delta x^2$  for all limiters and rather large  $\Delta x$ . However, we observe that there seems to be some saturation of the error for  $\Delta x \lesssim 0.01$ . We were not able to identify the cause/reason



(a) For the minmod limiter.



(b) For the MUSCL limiter.



(c) For the Superbee limiter.

FIG. 6. Test 1:  $L^1$  and  $L^\infty$  norm between the numerical and the exact solution on the computational domain as a function of the spatial resolution for initial conditions (89) and (90) for different limiters.

for this issue/limitation.

Still, we conclude that the numerical KT-HJ scheme seems to be suited for treating our system of coupled RG flow equations – at least for the rather smooth dynamics of this minimal test case.

### C. Test 2: First order phase transition and shock development

In order to challenge the numerical scheme further, we now consider another test case, where the  $\mathbb{Z}_2$ -symmetry of the ground state is (spontaneously) broken and restored dynamically during the RG flow. Here, however, we trigger a first-order-like phase transition by choosing the following initial conditions

$$U(\phi) = \phi^2, \quad (91)$$

$$H(\phi) = \begin{cases} -2 + 4\phi^6, & \text{if } |\phi| \leq 2, \\ 254, & \text{if } |\phi| > 2. \end{cases} \quad (92)$$

Again, the initial condition for the bosons is of Gaussian type and the nontrivial dynamics is caused by the boson-fermion-interactions. The reason we define  $H(\phi)$  in Eq. (92) as a piecewise function with some cusp at  $\varphi = 2$  is mainly due to the large- $\varphi$  behavior of the entire system: In general, we argued that the only restriction for  $H(\phi)$  for large  $\phi$  from the perspective of the (path) integral (11) is that it should not grow faster than polynomial. Also the PDE system, which is an initial value problem on  $\varphi \in \mathbb{R}$ , is still well-defined for such functions. However, inspecting Eq. (40) one finds that for  $H(t, \varphi)$  which asymptotically grows faster than  $\varphi^2$  the first term on the l.h.s. is not necessarily suppressed for large  $\varphi$  – even at  $t = 0$ , such that initial conditions like  $\lim_{\phi \rightarrow \infty} H(\phi) \sim \phi^6$  would at least lead to large errors from the artificial boundary conditions at  $\varphi_{\max}$ . Since we are not focused on the issue of boundary conditions and correctly handling the asymptotic, but want to benchmark the numeric scheme, we decided to choose a piecewise function with some nonanalyticity as the initial condition.

#### 1. Qualitative discussion

First, we turn to a qualitative discussion of the RG flows of  $M(t, \varphi)$  and  $H(t, \varphi)$  as well as the integrated quantities,  $\partial_\varphi U(t, \varphi)$  and the potential  $U(t, \varphi)$  itself. Overall, especially from Figs. 7a and 7b, we observe that the system exhibits a first-order-like phase transition during the RG flow, while ultimately in the IR the symmetry of the ground state is restored. However, it is much more interesting to inspect the dynamics during the flow on the level of  $M(t, \varphi)$  and  $H(t, \varphi)$ , the quantities that are



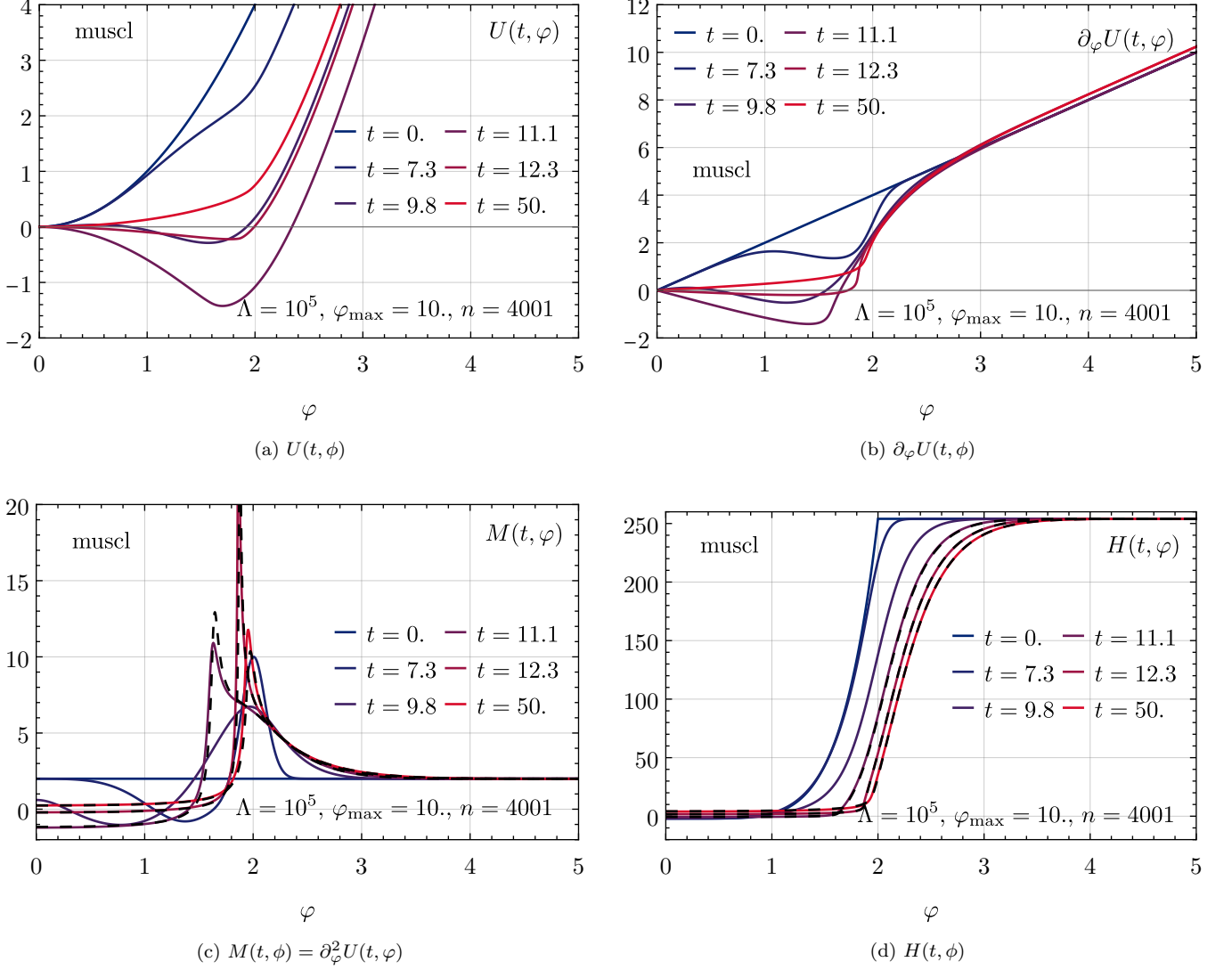


FIG. 7. Test 2: RG flow for the initial conditions (91) and (92). The exact reference solution for the last three times is shown black dashed.

actually evolved by the PDEs, see Figs. 7c and 7d. Here, we find that the contribution of  $H(t, \varphi)$  causes the development of a shock in the bosonic mass  $M(t, \varphi)$ , which is directly seen from the spike that forms at  $\varphi \approx 2$  and slightly moves to the right for increasing  $t$ . Ultimately, this shock is smeared out a bit and freezes, but the remnant is clearly visible in the first derivative of the effective potential  $\partial_\varphi U(t, \varphi)$ , see Fig. 7b, as well as in the potential itself, see Fig. 7a. Also note that the Yukawa coupling  $H(t, \varphi)$  as well as  $M(t, \varphi)$  both get shifted to values larger than zero in the IR. This is consistent with the fact that they are both two-point functions, which should be positive or zero in order to obtain a convex IR effective action (EAA) and well-defined/non-singular propagators. Again, we remark that  $r(t) + M(t, \varphi)$  as well as  $r(t) + H(t, \varphi)$  are always positive during the entire flow. Otherwise one would overshoot the pole of

the propagators in the flow equations (34) and (37) and  $\Gamma(t, \varphi, \vartheta, \bar{\vartheta})$  would not be well-defined in terms of a Legendre transform of  $W(t, J, \eta, \bar{\eta})$ .

Furthermore, we can compare our solutions to the exact reference solution at late RG times, which are depicted as dashed black lines.<sup>20</sup> Here, we find overall convincing agreement between the numerical and the exact solution. Only very close to the spike in  $M(t, \varphi)$  there are deviations, which can, however, be reduced by increasing the spatial resolution.

<sup>20</sup> Again, we only show the last three exact curves, because little new information is gained from also comparing the earlier times, while the computation of the exact reference solutions turns rather costly.

## 2. Quantitative discussion

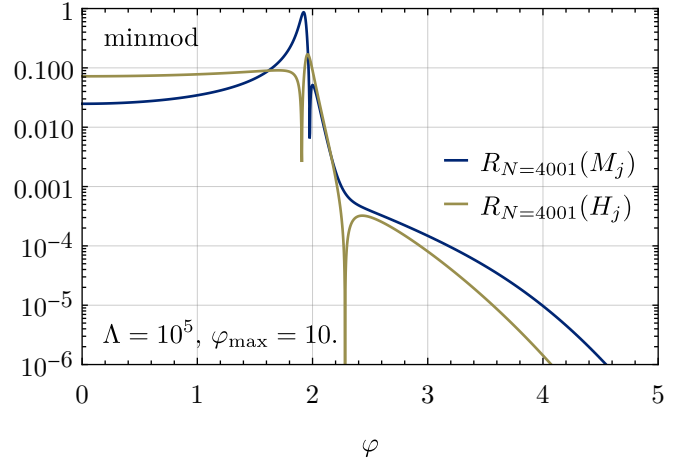
This can be further analyzed on a more quantitative level. First, we turn to the relative error of the numerical solution to the exact solution as a function of  $\varphi$  in Fig. 8 at constant  $\Delta x = 0.0025$ . We find that the large- $\varphi$  numerical error is very small and the numerical solution is comparable to the solution from the numerical evaluation of the expectation values. At small field values,  $|\varphi| < 2$ , in between the smeared shocks at  $\varphi \approx \pm 2$ , we find rather good agreement with the exact solution and relative errors of approximately 1%. Only close to the shock, the relative error increases up to almost 100%. This might sound worrying, but one has to keep in mind that the shock is a nonanalytic structure, which is hard to resolve with a numerical scheme. Additionally, these seemingly large errors can be traced back to a minimal offset and difference in height of the shock position in the numeric solution compared to the exact solution, as can be seen in Fig. 7c. However, for very singular structures, a minimal offset in the position can lead to large relative errors, even though the numeric solution is very close to the exact solution and satisfying for practical purposes.

Finally, we turn to the scaling of the error with the resolution in Fig. 9. Here, we find that for small resolution, thus large  $\Delta x$ , the error scaling is again polynomial. However, the explicit errors are rather large for all limiters – especially the  $L_\infty$  error. Still, this is expected, since it measures the maximum error over all grid points and for low resolutions, the shock is not resolved and its position is off. However, even for small  $\Delta x$  we have already mentioned that the slight offset of the shock position can still lead to rather large relative errors. For the  $L_1$  norm, we find that the error is overall smaller, because it is the absolute deviation averaged over all grid points. In general, we find for both error measures that for rather large  $\Delta x$  they scale approximately like  $\Delta x^2$ . However, for small  $\Delta x$  one even finds scalings that are worse than  $\Delta x$ , which seems to be related to the resolution of the shock structure.

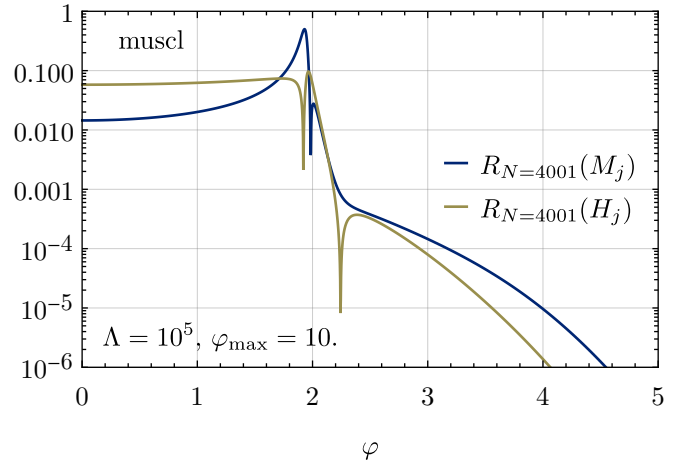
In general, we are satisfied with the performance of the nonconservative scheme for such a challenging test, which motivates us to further investigate the capabilities of the KT-HJ scheme.

### D. Test 3: A “mild” sign problem and “shockingly” hard dynamics

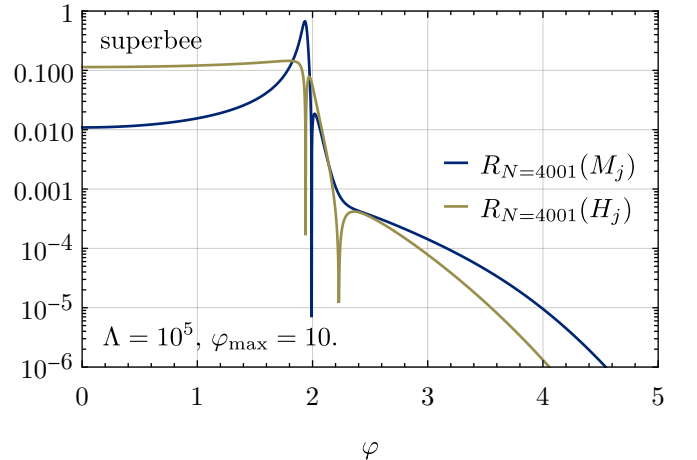
As indicated in the introduction, this work is not only about testing new numerical schemes for FRG flow equations but also about conceptual aspects of the Wetterich equation. Therefore, we now turn to a test case, which is not only extremely challenging for the numerics but also an interesting realization of a sign problem, nonanalyticities, phase transitions, and a prime example of Yang-Lee zeros on the level of RG flows. To study this interesting dynamics and “physical” situation we propose the initial



(a) For the minmod limiter.

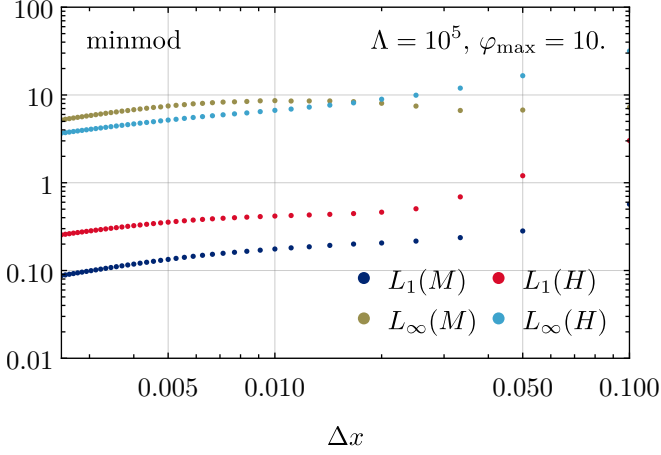


(b) For the MUSCL limiter.

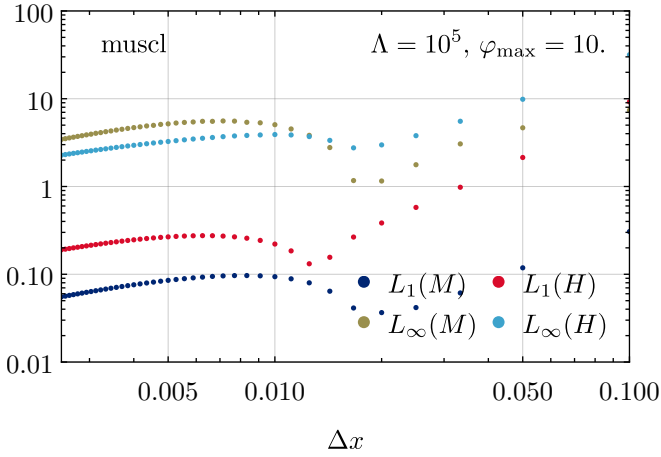


(c) For the superbee limiter.

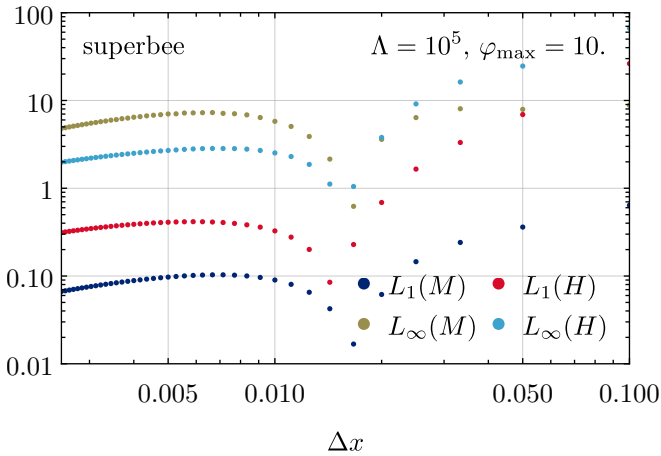
FIG. 8. Test 2: Relative error (84) of the numerical solution to the exact solution as a function of  $\varphi$  for the initial conditions (91) and (92) for different limiters at a resolution of  $N = 4001$  points with  $\varphi_{\max} = 10$ .



(a) For the minmod limiter.



(b) For the MUSCL limiter.



(c) For the superbee limiter.

FIG. 9. Test 2:  $L^1$  and  $L^\infty$  norm between the numerical and the exact solution on the computational domain as a function of the spatial resolution for the initial conditions (91) and (92) for different limiters.

conditions

$$U(\phi) = \phi^2, \quad (93)$$

$$H(\phi) = \begin{cases} \frac{1}{2} \phi^2 - \frac{1}{18} \phi^4 + \frac{1}{720} \phi^6, & \text{if } |\phi| \leq 8, \\ \frac{2528}{15}, & \text{if } 8 \leq |\phi|. \end{cases} \quad (94)$$

Hence,  $U(\phi)$  is again of the Gaussian type, while  $H(\phi)$  is of polynomial type with two dips at  $\phi \approx \pm 4.5$ , where  $H(\phi)$  even turns negative, see also the blue curves in Fig. 11 (right column). The reason, why we choose  $H(\phi)$  as a piecewise function with a cusp at  $\phi = \pm 8$  is the same as explained below Eq. (92) and does only minimally affect the actual dynamics in the interesting region  $|\phi| < 7$ . It simply avoids dealing with the large- $\phi$  boundary conditions in a more sophisticated way.

### 1. Discussion from the path-integral perspective

Before we turn to the discussion of this problem with the RG flow equations, let us first analyze the exact reference solution on the level of the path integral, the (connected) correlation functions and the vertex functions in the presence of sources  $J$ , respectively.

To this end, we directly compute the Schwinger functional  $\mathcal{W}(J) = \mathcal{W}(J, 0, 0)$  and its first and second derivatives w.r.t.  $J$  from Eqs. (20) and (11) and plot the results in Figs. 10a–10c in blue (and red). We immediately observe that the Schwinger functional  $\mathcal{W}(J)$  is smooth and convex for small and large  $|J|$ , while there is a region between  $J = \pm 5.8(6)$  and  $J = \pm 10.3(1)$  where  $\mathcal{W}(J)$  is nonconvex, which is also directly seen from  $\partial_J \mathcal{W}(J)$  and  $\partial_J^2 \mathcal{W}(J)$ . In this region  $\mathcal{W}(J)$  even has poles and gains an imaginary part. From a statistical physics perspective we identify these poles as Yang-Lee (YL) zeros in the partition function (11), which are associated with phase transitions, see Refs. [55, 90, 91, 104] for recent works in the FRG context. Here, these phase transitions are triggered by cranking up the external source  $J$  and should realize as kinks and jumps in the bosonic expectation values. Hence, at this point we already conclude that the fermionic degrees of freedom can indeed cause nonanalytic structures and phase transitions even in zero spacetime dimensions, which is not possible in purely bosonic systems.

Next, we have to ask the question of how these structures in  $\mathcal{W}(J)$  are reflected in  $\Gamma(\varphi, \tilde{\vartheta}, \vartheta)$ , the vertex functions, and consequently the RG flow of  $M(t, \varphi)$  and  $H(t, \varphi)$ . We know, that the result of the Legendre transformation (21) is a convex function, which after Legendre-backtransformation again yields a convex  $\mathcal{W}$ , see Refs. [105, 106] for details. Let us therefore find the convex  $\mathcal{W}(J)$  directly via a Maxwell construction. The corresponding results are depicted in ochre/gold in Figs. 10a–10c. We start with the second derivative, see

Fig. 10c, and argue that it should never turn negative in order to obtain a convex  $\mathcal{W}(J)$ . Hence, the region between the zeros in  $\partial_J^2 \mathcal{W}(J)$  is replaced by  $\partial_J^2 \mathcal{W}_M(J) = 0$ . On the level of the slope,  $\partial_J \mathcal{W}(J)$ , see Fig. 10b, this corresponds to a constant slope, where we simply take the value of  $\partial_J \mathcal{W}(J)$  at  $J = \pm 5.8(6)$  and  $J = \pm 10.3(1)$  and extrapolate (integrate  $\partial_J^2 \mathcal{W}_M(J)$ ) to the left/right. The points  $J = \pm 8.1(3)$ , where  $\partial_J \mathcal{W}_M(J)$  jumps are obtained via  $\mathcal{W}_M(J)$  itself: It is simply the point, where the two straight lines intersect. In summary, we find the Maxwell construction  $\mathcal{W}_M(J)$ , which contains (for positive  $J$ ) three kinks and two straight lines. The latter are the phase-coexistence regions and we denote the kinks as phase transitions (PT) points.

From  $\mathcal{W}_M(J)$  it is now straight forward to calculate the Legendre transformation and to extract  $U(\varphi)$ ,  $u(\varphi) = \partial_\varphi U(\varphi)$ ,  $M(\varphi) = \partial_\varphi^2 U(\varphi)$  and  $H(\varphi)$  as explained in Section III B. These are the IR reference solutions for the RG flows with Eqs. (93) and (94) as initial conditions. Inspecting Fig. 10d, where we plot  $u(\varphi)$ ,  $M(\varphi)$ , and  $H(\varphi)$ , we immediately recognize that this is prospective IR solution will present a very challenging problem on the level of the FRG and PDE numerics: The IR solution has poles as well as a flat region in between, which is extremely hard to resolve and to flow into.<sup>21</sup> As we discuss in the next paragraphs, we find that on the level of the PDEs this is caused by the  $H(t, \varphi)$  being negative for some  $\varphi$ .

In fact, negative  $H(\phi)$  is exactly what we denoted as a sign problem in Section III. On the level of the (path) integral (11), we have argued that a (partially) negative  $H(\phi)$  leads to (in parts) negative or oscillating probability distributions, cf. Eq. (16). Hence, already before solving the actual RG flows (numerically), we claim that some sign problems in QFTs might show up as challenging nonanalyticities on the level of the FRG flow equations. Similar arguments were already put forward in Refs. [27, 28, 47, 55, 56], where it was seen that a chemical potential causes external shocks in RG flows.

## 2. Discussion from the FRG perspective

Next, let us analyze the same problem within the framework of the FRG and the RG flow equations (39) and (40). The corresponding RG flows for  $M(t, \varphi)$  and  $H(t, \varphi)$  are depicted in Fig. 11 for the three different limiters. However, for the qualitative part of the discussion we simply focus on the plots Figs. 11c and 11d. Since the UV potential  $U(t, \varphi)$  is Gaussian, the RG flow for  $M(t, \varphi)$  starts with a constant function  $M(t=0, \varphi) = 2$ , while the flow of  $H(t, \varphi)$  starts as a polynomial with two

dips below zero (blue curves). During the flow, we observe the following: First, the cusp at  $\varphi = \pm 8$  in  $H(t, \varphi)$  causes a small bump in  $M(t, \varphi)$  at the same position. Both, the cusp and this bump are still visible in the final solution even though they are smeared out and do not significantly influence the other dynamics. The main dynamics takes place at  $\varphi$ -values around the region, where  $H(t, \varphi)$  used to be negative in the UV. Here, the propagator  $1/(r + H)$  is closer to its pole than in other regions, which causes a strong response in the flow of both,  $M(t, \varphi)$  and  $H(t, \varphi)$ . In fact,  $M(t, \varphi)$  is lowered in this region and even turns negative for some  $\varphi$ . In turn, this also causes the propagator  $1/(r + M)$  to be closer to its pole, fostering even faster dynamics. In particular, we observe some strong advective dynamics, which pushes  $M(t, \varphi)$  and  $H(t, \varphi)$  to the left and right of the negative region, while the negative region itself flattens and approaches zero from below. Thereby,  $M(t, \varphi)$  develops two shocks/poles and  $H(t, \varphi)$  develops two cusps, which we immediately identify as the phase transition points from the path-integral perspective, compare with the black-dashed curves and Fig. 10d. Before we turn to some comments on the quantitative performance, let us mention the following interesting aspects: As becomes clear from the final RG times, which correspond to regulator values of  $r \approx 0.1$ , we were not able to flow arbitrarily deep into the IR. The reason for this is that the propagators  $1/(r + M)$  and  $1/(r + H)$  approach their poles for  $r \rightarrow 0$  in the flat region and the PDE system turns into an extremely stiff problem. Even with the advanced implicit time-stepping algorithm, which is still stable, the number of time-steps simply explodes and the computation time becomes unfeasible, which is why we stopped after 600k time steps. The reason, why it was possible to flow deeper to the IR with the minmod limiter, see Figs. 11a and 11b, is that it leads to more diffusive flows. By smearing out the poles,  $M(t, \varphi)$  and  $H(t, \varphi)$  do turn slightly positive in the flat region instead of correctly approaching zero from below, as it is the case for the MUSCL and Superbee limiters. Still, as can be seen from the black dashed curves in Figs. 11a and 11b, which correspond to the exact reference solutions at the respective latest three RG times obtained from the formulae from Section III B, the FRG results almost perfectly agree with the exact ones.<sup>22</sup>

In fact, this general behavior of  $M(t, \varphi)$  approaching zero from below is well-known from higher-dimensional RG problems in their symmetry broken regimes. In the present case, however, we can directly see that this is not only related to condensation, but also to the presence of

<sup>21</sup> Similar highly challenging problems are used as tests for fluid-dynamic numerics. For example, the Sod's shock tube problems [107] with suitable initial conditions can produce rarefaction waves and approach vacuum solutions.

<sup>22</sup> We could have presented the same curves for the MUSCL and Superbee limiters as well as for earlier RG times. However, for earlier RG times we again face the problem of excessively large computational domains in the source field  $J$  to obtain  $\varphi(J)$  in the interesting region. Additionally, for late RG times, after formation of the pole structures, one has to perform the Maxwell construction from Section VID 1 for each RG step. Since new insights are limited, we abstained from both endeavour.

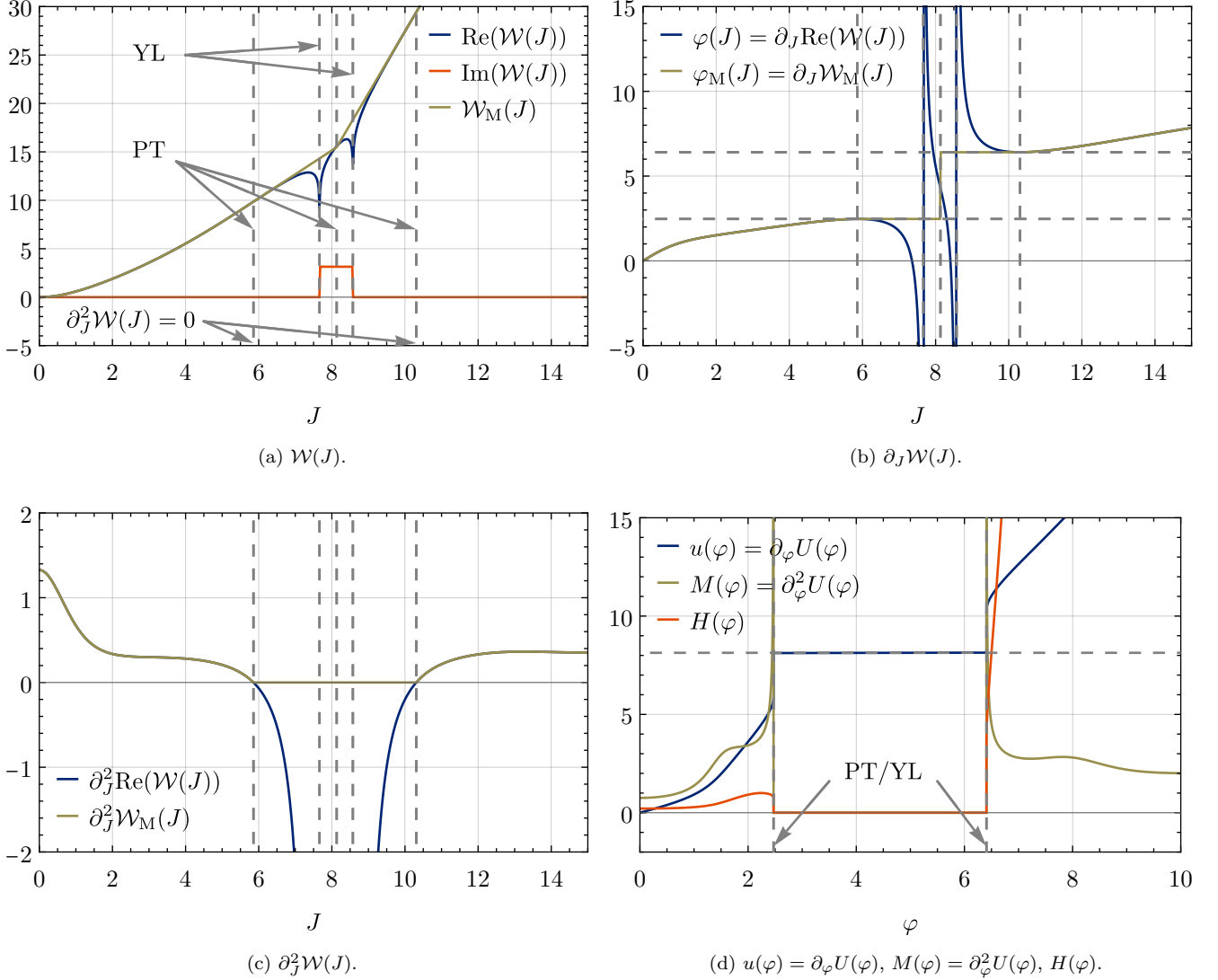


FIG. 10. Test 3: Exact (connected) field-dependent correlation functions and vertex functions in the presence of sources  $J$  for Eqs. (93) and (94).

negative  $H(t, \varphi)$  and the associated sign problem. We therefore conclude that sign problems on the level of the path integral may indeed show up in RG flows as nonanalytic structures and may turn into stiff PDE problems. This definitely questions the common lore that FRG approaches are not affected by sign problems and calls for further investigations. On a conceptual level sign problems might be less apparent in the FRG but on a practical/numerical level they might present severe challenges.

Finally, we comment on the quantitative performance of the KT-HJ scheme for this challenging problem. As mentioned earlier and as it is visible in Fig. 11 it does not really make sense to show relative or  $L_1$  and  $L_\infty$  errors. Even though the scheme is in general able to resolve and propagate the shocks and cusps without spurious oscillations, there are still small offsets in their positions. In addition,  $M(t, \varphi)$  and  $H(t, \varphi)$  will never exactly reach the

final solution, since we cannot flow all the way to  $r = 0$ . Especially in the flat region, this would cause large deviations. Hence, we abstain from a deeper quantitative analysis and are satisfied with the qualitative performance of the scheme for this extremely challenging test case. To this end, we solely compare the solutions at the latest RG time to the exact reference solution in Fig. 12 for different limiters.

Equipped with the insights from our zero-dimensional toy model, we next turn to some higher-dimensional examples.



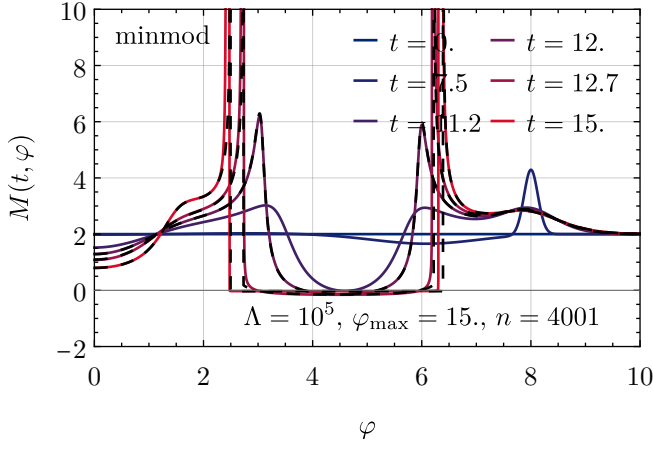
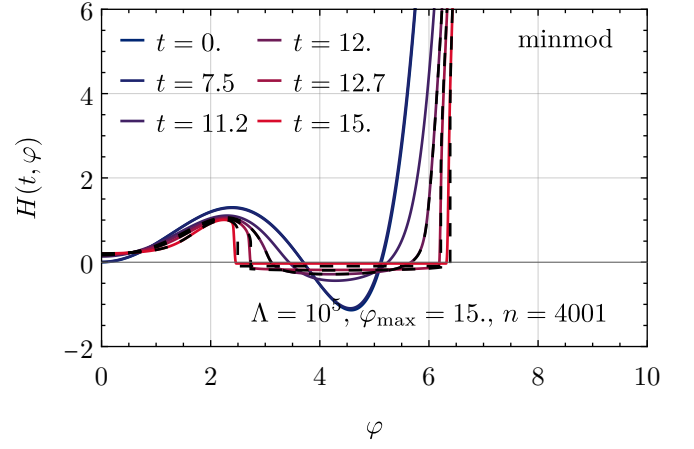
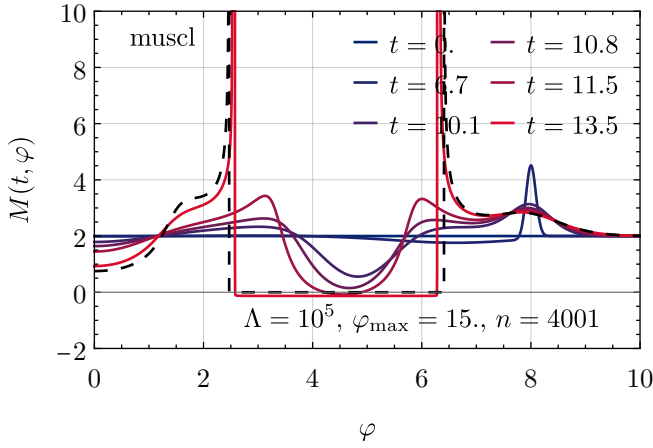
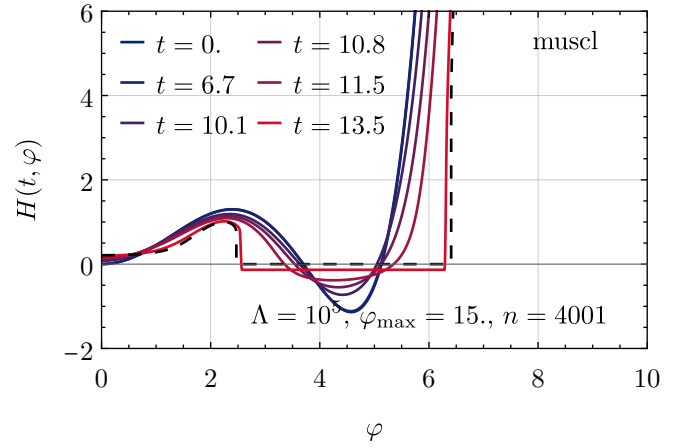
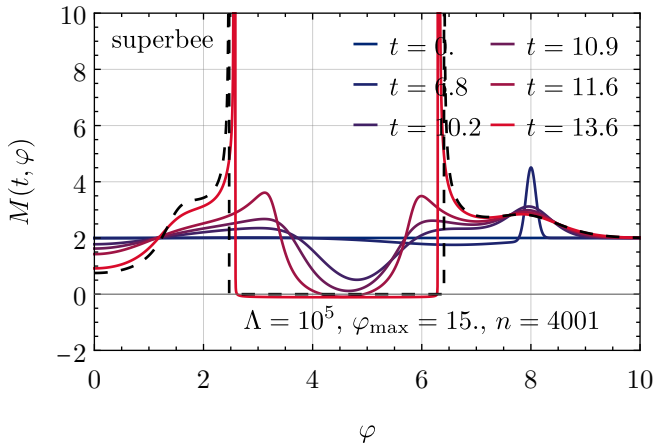
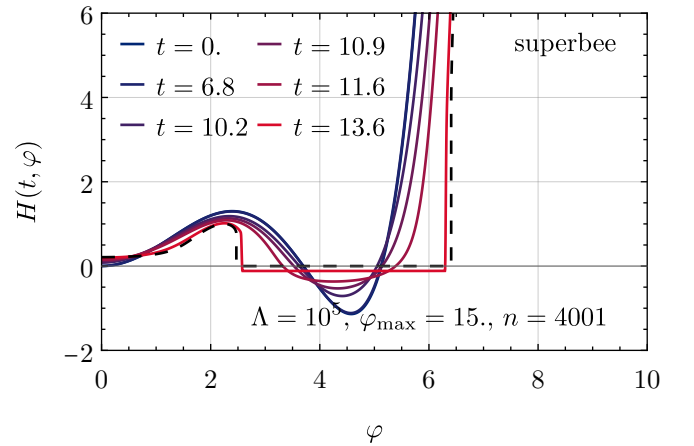
(a)  $M(t, \phi)$  for the minmod limiter.(b)  $H(t, \phi)$  for the minmod limiter.(c)  $M(t, \phi)$  for the MUSCL limiter.(d)  $H(t, \phi)$  for the MUSCL limiter.(e)  $M(t, \phi)$  for the Superbee limiter.(f)  $H(t, \phi)$  for the Superbee limiter.

FIG. 11. Test 3: RG flow with the initial conditions (93) and (94) for different limiters. The analytic solution for the last three RG times in Figs. 11a and 11b as well as the IR ( $t \rightarrow \infty$ ) reference solution in Figs. 11c–11f are shown as black dashed curves.

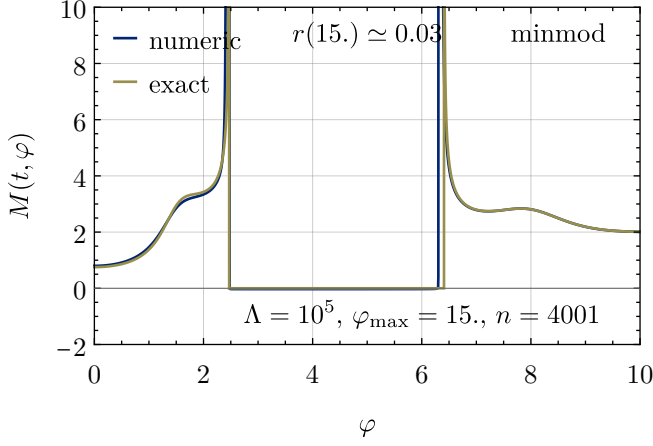
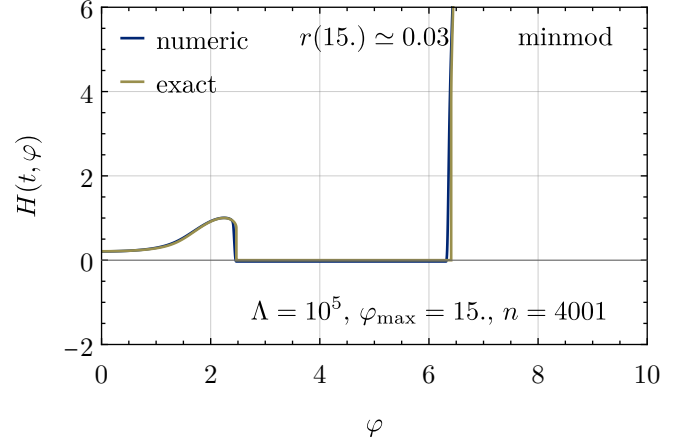
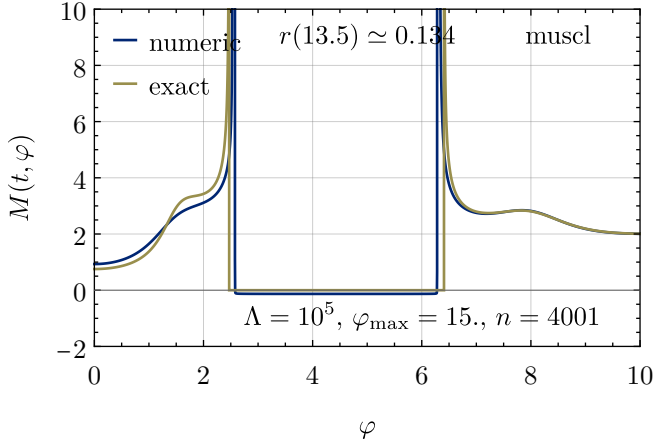
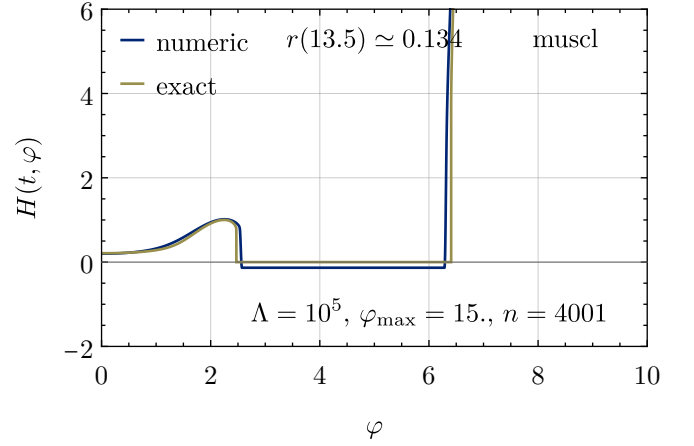
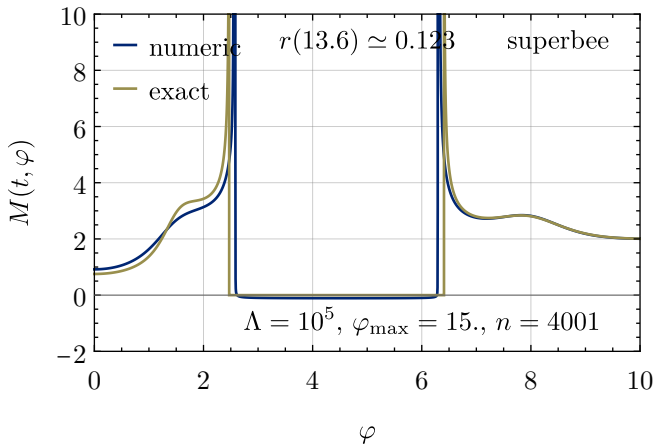
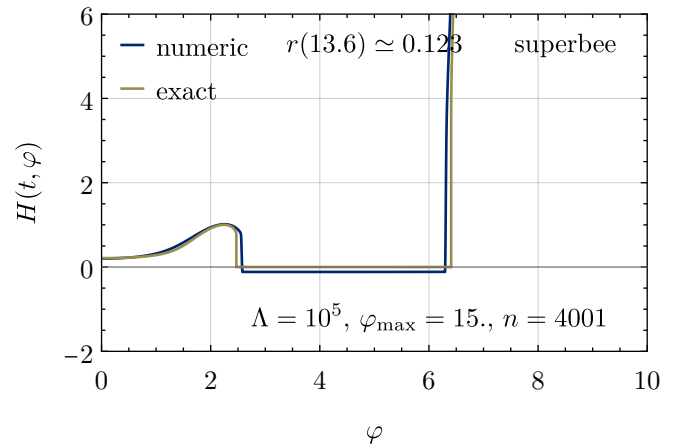
(a)  $M(t, \phi)$  for the minmod limiter.(b)  $H(t, \phi)$  for the minmod limiter.(c)  $M(t, \phi)$  for the MUSCL limiter.(d)  $H(t, \phi)$  for the MUSCL limiter.(e)  $M(t, \phi)$  for the Superbee limiter.(f)  $H(t, \phi)$  for the Superbee limiter.

FIG. 12. Test 3: Comparison of the exact IR reference solution ( $t \rightarrow \infty$ ) from Fig. 10d (gold) to the numerical solution at finite  $t$  (blue) from the RG flow with the initial conditions (93) and (94) for different limiters.

## VII. APPLICATIONS TO HIGHER DIMENSIONAL MODELS

In this section, we turn to some explicit applications of our developments to higher-dimensional systems. Note that within this work we are not aiming at deeper insights into the physics of these systems, but rather at demonstrating the performance of the KT-HJ scheme and the new formulation of the flow equations for more realistic systems. We consider the following two setups:

1. First, we discuss a  $\mathbb{Z}_2$ -symmetric system of a single real scalar field in three Euclidean dimensions. In particular, we study the FRG flow of the effective potential and the wave-function renormalization with full field dependence. Thereby, we use two different types of regulators.
2. Second, we consider another  $\mathbb{Z}_2$ -symmetric system. Here, however, we analyze the RG flow of the effective potential and field-dependent Yukawa coupling in the Gross-Neveu-Yukawa model in  $1+1$  dimensions at nonzero temperature and chemical potential.

### A. Field-dependent wave-function renormalization in the $\mathbb{Z}_2$ -symmetric model

Let us turn to our first example – the  $\mathbb{Z}_2$ -symmetric FRG flow of the effective potential and the wave-function renormalization in three Euclidean dimensions. In terms of a truncation, the EAA for the model is given by

$$\bar{\Gamma}_t[\varphi] = \int d^d x \left[ U_t[\varphi] + Z_t[\varphi] \frac{1}{2} (\partial_\mu \varphi)^2 + \mathcal{O}(\partial^4) \right], \quad (95)$$

with the  $\mathbb{Z}_2$ -symmetric scale-dependent effective potential and wave-function renormalization,

$$U_t[\varphi] = U_t[-\varphi], \quad Z_t[\varphi] = Z_t[-\varphi]. \quad (96)$$

We ignore terms, which are of higher order in the derivatives of  $\varphi(x)$ , hence nonquadratic momentum dependences. Furthermore, we define the RG time

$$t = -\ln\left(\frac{k}{\Lambda}\right), \quad t \in [0, \infty), \quad (97)$$

where  $\Lambda$  is the ultraviolet cutoff and  $k$  is the renormalization group scale, which are both of dimension of energy. For the moment, we keep  $d \geq 1$  arbitrary and only specify it later as  $d = 3$ .

#### 1. Flow equations

The corresponding RG flow equations for the second derivative of the effective potential  $M(t, \sigma) = \partial_\varphi^2 U_t[\varphi]|_{\varphi(x)=\sigma}$  and  $Z(t, \sigma) = Z_t[\sigma]$ , where  $\sigma$  is some constant background field configuration are both directly extracted from the flow equation (98) of the full momentum-dependent bosonic two-point function. The latter is directly derived from the Wetterich equation (1) by taking two functional derivatives with respect to the field  $\varphi$ , cf. Eq. (7). In momentum space, we again recover a HJ-type flow equation, cf. Section II,

$$\begin{aligned} \partial_t \bar{\Gamma}_t^{(2)}(q_2, q_1) = & \\ = - \int_{p_1, \dots, p_4} & \left( \frac{1}{2} \partial_t R_t(p_1, p_2) \right) G_t(p_2, p_3) \bar{\Gamma}_t^{(4)}(p_3, p_4, q_1, q_2) G_t(p_4, p_1) + \\ + 2 \int_{p_1, \dots, p_6} & \left( \frac{1}{2} \partial_t R_t(p_1, p_2) \right) G_t(p_2, p_3) \bar{\Gamma}_t^{(3)}(p_3, p_4, q_1) G_t(p_4, p_5) \bar{\Gamma}_t^{(3)}(p_5, p_6, q_2) G_t(p_6, p_1), \end{aligned} \quad (98)$$

Here, we use the abbreviation

$$\int_{p_1, \dots, p_n} = \int_{-\infty}^{\infty} \frac{d^d p_1}{(2\pi)^d} \cdots \frac{d^d p_n}{(2\pi)^d} \quad (99)$$

and introduced the regulator

$$R_t(p_1, p_2) = (2\pi)^d \delta^{(d)}(p_1 + p_2) R(t, p_1^2), \quad (100)$$

$$R(t, p^2) = p^2 r_t(p^2), \quad (101)$$

where  $r_t(p^2)$  is a suitable regulator shape function. In particular, we use the Callan-Symanzik type regulator

$$r_t(p^2) = \frac{k^2}{p^2}, \quad (102)$$

and the Litim/flat regulator,

$$r_t(p^2) = \left(\frac{k^2}{p^2} - 1\right) \Theta\left(\frac{k^2}{p^2} - 1\right), \quad (103)$$

both without including any dependence on the field, the couplings, or the wave-function renormalization. Let us also note that due to momentum conservation,

$$\bar{\Gamma}_t^{(2)}(q_2, q_1) = (2\pi)^d \delta^{(d)}(q_2 + q_1) \bar{\Gamma}^{(2)}(t, q_1). \quad (104)$$

Inserting the ansatz (95) in Eq. (98), evaluating the equation on a constant background field configuration  $\varphi(x) = \sigma$ , as well as evaluating the integrals, we find the flow equation for  $\bar{\Gamma}^{(2)}(t, q_1)$ . By either evaluating this at  $q_1 = 0$  or taking a derivative with respect to  $q_1^2$  and only afterwards setting  $q_1 = 0$ , we find the flow equations for  $M(t, \sigma)$  and  $Z(t, \sigma)$ , respectively. The symbolic computation is a nontrivial task with some subtle details, which we elaborate on in Appendix D. The final expressions for the flow equations using the regulator shape functions (102) and (103) are rather lengthy and are presented explicitly in Appendix D, see also Refs. [90, 91, 104]. However, note, that overall, we find the following structure of the flow equations for both regulators,

$$\begin{aligned} \partial_t M + \#_1 (M')^2 + \#_2 M' Z' + \#_3 (Z')^2 &= \\ = \#_4 M'' + \#_5 Z'', \end{aligned} \quad (105)$$

and

$$\begin{aligned} \partial_t Z + \tilde{\#}_1 (M')^2 + \tilde{\#}_2 M' Z' + \tilde{\#}_3 (Z')^2 &= \\ = \tilde{\#}_5 Z'', \end{aligned} \quad (106)$$

where  $\#_i$  and  $\tilde{\#}_i$  are coefficients, which depend on  $t$ ,  $M$ , and  $Z$ . Consequently, the structure is – as already anticipated – similar to the one of Eqs. (39) and (40) and the KT-HJ scheme is applicable. However, analogously to the zero-dimensional case, we solely solve the flow equation for  $Z(t, \sigma)$  via the HJ approach, while we treat the entire flow equation for  $M(t, \sigma)$  as a conservation law, see Eqs. (D10) and (D12), and use the conservative KT scheme Eq. (78).

## 2. Discussion

Next, let us turn to the discussion of the RG flows and IR results for  $M(t, \sigma)$  and  $Z(t, \sigma)$ . To this end, we always fix the scales of the problem by setting  $\Lambda = 1$  and consider the UV initial conditions of the type

$$U(t=0, \sigma) = \frac{1}{4} \left( \frac{\sigma^2}{2} - \frac{\sigma_0^2}{2} \right)^2, \quad (107)$$

where we choose different  $\sigma_0$  in order to either end the RG flow in the symmetric or symmetry broken phase.

Furthermore, we set  $Z(t=0, \sigma) = 1$ . For each regulator – Callan-Symanzik and Litim – we do the same analysis: We take two different values for  $\sigma_0$ , one, which ends the flow in the symmetric phase and one, which ends the flow in the symmetry broken phase, close to the phase transition. Then we compute the RG flows of  $M(t, \sigma)$  and  $Z(t, \sigma)$  within two different truncations: First, we use the LPA truncation, where we keep  $Z(t, \sigma) = 1$  fixed on the r.h.s. of the flow equations. Still, we compute the flow of  $Z(t, \sigma)$  evaluated on the LPA solution for  $M(t, \sigma)$  without feeding it back on the r.h.s. of the flow equations. Second, we use the local potential approximation prime (LPA') truncation, where we take into account the full flow of  $Z(t, \sigma)$  on the r.h.s. of the flow equation for  $M(t, \sigma)$  and  $Z(t, \sigma)$  itself. This allows us to study the impact of a dynamic field-dependent wave-function renormalization.

Let us begin the discussion with the results for the Litim regulator, which are shown in Figs. 13 and 14. First, we discuss the IR results shown in Fig. 13. If the flow ends in the symmetric phase, one can flow arbitrarily close to  $k = 0$ . We simply stop the flow at  $t = 20$ , since no significant changes have occurred for some time beforehand. In this case, we find a smooth convex effective potential with a single minimum at  $\sigma = 0$  and a positive mass function  $M(t, \sigma)$ . The wave-function renormalization  $Z(t, \sigma)$  is close to one and only shows a mild field dependence. Deviations between LPA and LPA' are only marginal. Second, we consider the flow into the symmetry-broken phase. Here, the system turns stiff at  $t = 4.14$  in LPA' and while it is still possible to flow further to the IR in LPA, see Fig. 13, where we stopped the flow at  $t = 7$ . However, comparing the IR results of both truncations in the broken phase at the same  $t_{\text{IR}} = 4.14$ , we find significant deviations. In particular, the position of the IR minimum of the effective potential is moved to slightly smaller field values. Even more important is the deviation in the profile of the wave-function renormalization. In LPA,  $Z(t, \sigma)$  sticks to  $Z(t, 0) = 1$  but shows a strong peak in the flat region of the potential, while it falls off very fast at field-values larger than the minimum of the potential. In contrast, in LPA' it develops a nontrivial shape around  $\sigma = 0$ , which we expect to turn into a fully-fledged peak in the IR limit in even better truncations. The peak close to the minimum is still visible but much smaller than in LPA. Still, it is interesting, that the large-field behavior is almost the same in both truncations and especially at the physical point – the minimum itself – the effect of a dynamic wave-function renormalization is only mild.

In order to get a better understanding of the actual dynamics, we show the full RG flows of  $M(t, \sigma)$  and  $Z(t, \sigma)$  in Fig. 14 in the symmetry-broken regime. Here, it should also become clear that the reason for stopping the RG flow at some finite  $t$  is not related to the numeric scheme but rather to the stiffness of the PDE problem itself. It is even unclear to the authors whether the flow can be extended to arbitrarily large  $t$  in principle within a truncation or if the  $t \rightarrow \infty$  limit is only accessible for the

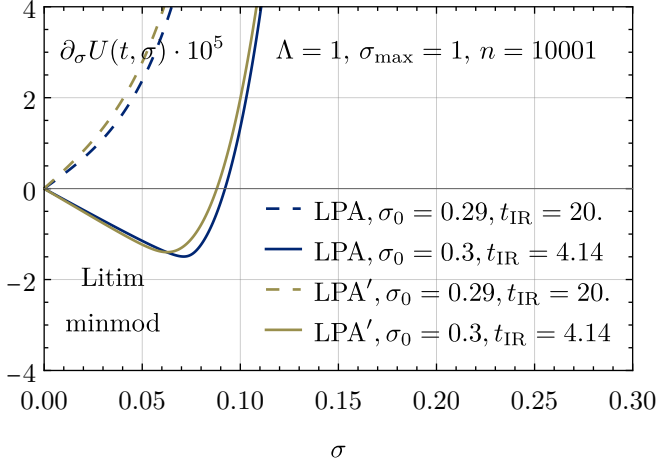
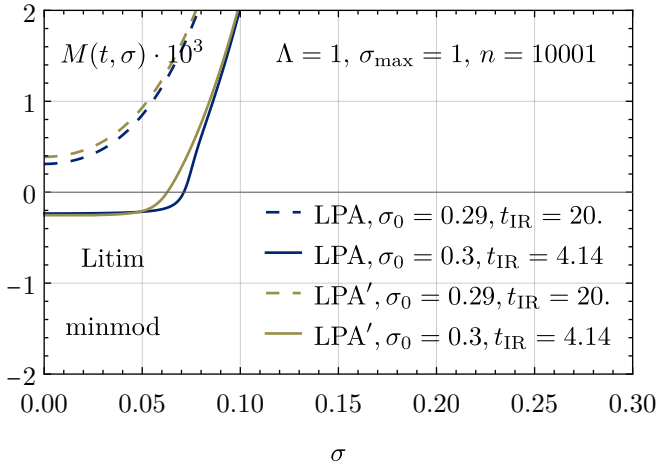
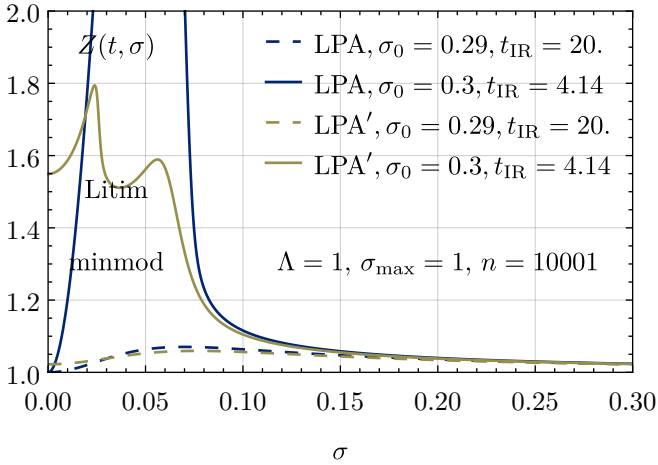
(a)  $u(t, \sigma) = \partial_\sigma U(t, \sigma)$ (b)  $M(t, \sigma) = \partial_\sigma^2 U(t, \sigma)$ (c)  $Z(t, \sigma)$ 

FIG. 13. IR results of RG flows of  $\partial_\sigma U(t, \sigma)$ ,  $M(t, \sigma) = \partial_\sigma^2 U(t, \sigma)$ , and  $Z(t, \sigma)$  with the Litim regulator into the symmetric and symmetry-broken regime in LPA and LPA'.

untruncated Wetterich equation.

Next, let us briefly turn to the results for the Callan-Symanzik regulator, which are shown in Figs. 15 and 16. First, note that the explicit values for  $\sigma_0$  are different than for the Litim regulator, which implies that the critical point is regulator dependent. Next, instead of repeating the entire discussion, let us only highlight the differences. For the Callan-Symanzik regulator we observe that the system is in general much stiffer than for the Litim regulator and we cannot flow deep into the IR in the symmetry-broken phase, independent of the truncation. Apart from this, the results are qualitatively similar to the ones for the Litim regulator and we again find huge differences for the wave-function renormalization in the flat region of the potential between LPA and LPA', while the effect of the wave-function renormalization at the physical point and beyond as well as in the symmetric phase is mild.

Let us conclude this section with the remark that we have demonstrated the general applicability and stability of our new numerical scheme to solve RG flows involving field-dependent wave-function renormalizations. We hope that this will pave the way for more advanced studies of FRG flows including nontrivial momentum dependencies in the future that go far beyond the limited application and discussion presented here.

## B. Gross-Neveu-Yukawa model

Within the next paragraphs, let us turn to our last example of this work. We consider the Gross-Neveu-Yukawa (GNY) model in 1+1 dimensions at nonzero temperature  $T$  and fermion chemical potential  $\mu$ . The GNY model is a well-known prototype QFT, which is used as a toy model for various phenomena in particle physics, condensed matter physics, and statistical physics, *e.g.*, dimensional transmutation, asymptotic freedom, dynamical (chiral) symmetry breaking/restoration, critical phenomena, thermal and quantum phase transitions, phases of spatially inhomogeneous condensation and so on. It is the bosonized version of the Gross-Neveu (GN) model, which describes the interactions of  $N$  species of relativistic fermions via local scattering in the scalar channel. Therefore, it is the perfect testing ground to apply our new numerical scheme and to demonstrate the performance for systems including field-dependent Yukawa couplings. For details on the GN and GNY model, we refer to the nonexhaustive list of Refs. [47, 108–132].

Let us start by providing the ansatz for the EAA of the GNY model within a scLPA,

$$\bar{\Gamma}_t[\bar{\psi}, \psi, \varphi] = \quad (108)$$

$$= \int_{-\infty}^{\infty} dx \int_0^{\frac{1}{T}} d\tau [\bar{\psi} (\gamma^\nu \partial_\nu - \mu \gamma^0 + m_t[\varphi]) \psi +$$



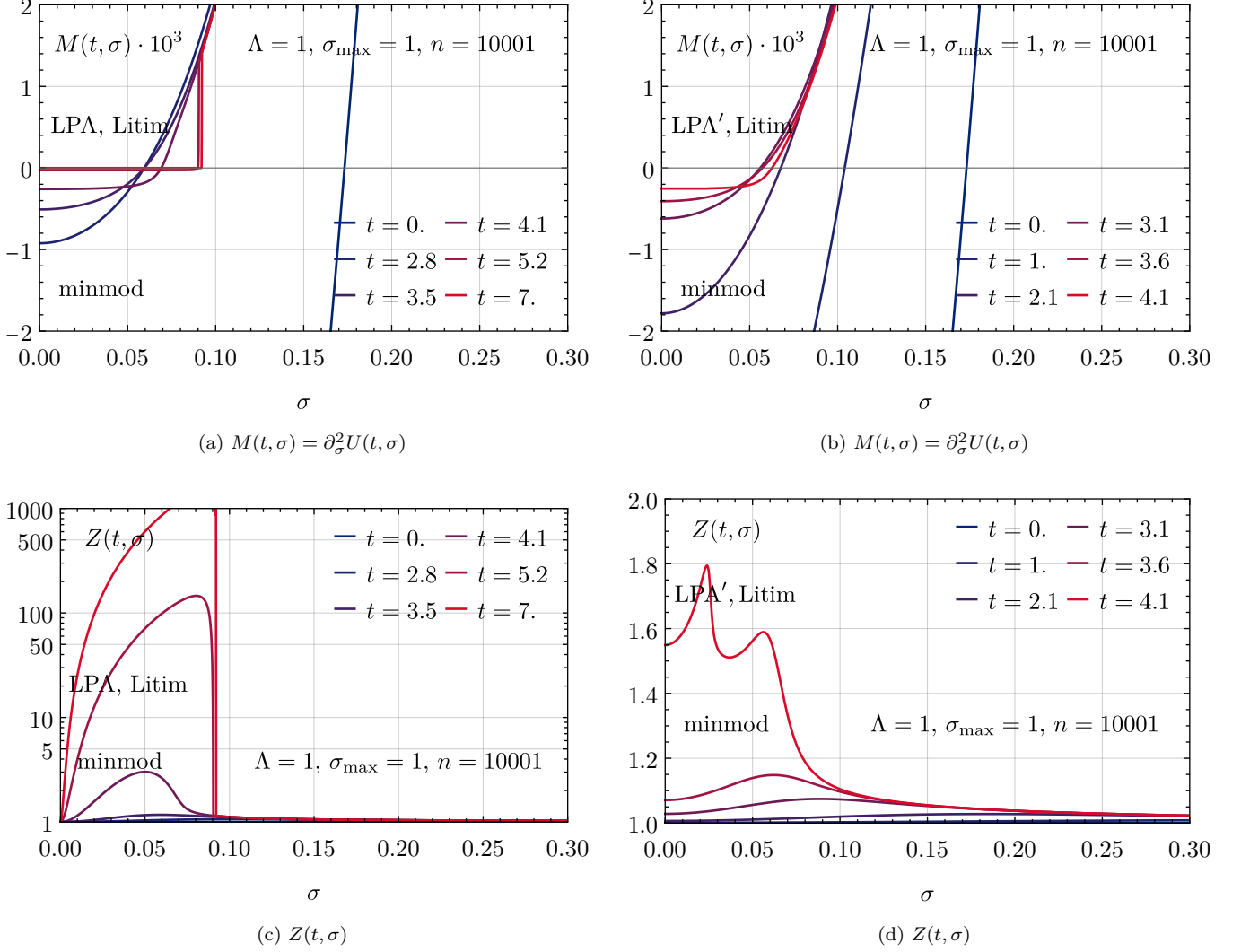


FIG. 14. RG flows of  $M(t, \sigma) = \partial_\sigma^2 U(t, \sigma)$  and  $Z(t, \sigma)$  with the Litim regulator in the symmetry-broken regime in LPA and LPA'.

$$+ \frac{N}{2} (\partial_\mu \varphi)^2 + N U_t[\varphi].$$

Hereby,  $\varphi(\tau, x)$  describes the bosonic scalar field that is generated from the four-fermion interaction via bosonization. The fermionic fields  $\psi(\tau, x)$  and  $\bar{\psi}(\tau, x)$  are two-component spinors, which are defined in the Euclidean spacetime and come in  $N$  species (sometimes called flavors). Hence, the gamma matrices  $\gamma^\nu$  are  $2 \times 2$  matrices with  $\nu \in \{0, 1\}$ . The bosons couple to the fermions via the field- and scale-dependent fermion mass  $m_t[\varphi]$ . In the UV limit, this term is simply given by a Yukawa interaction  $h_\Lambda \varphi$  that can be generated from the four-fermion interaction via a Hubbard-Stratonovich transformation. In general, we work with zero bare fermion mass, hence in the chiral limit. For the sake of the simplicity, we choose  $h_\Lambda = 1$  to set the scales of the model (the Yukawa coupling has dimension energy). Additionally, we have

a kinetic term for the bosonic field as well as a scale-dependent effective potential  $U_t[\varphi]$ , which are both multiplied by the number of fermions,  $N$ , because we are working in  $\frac{1}{N}$ -rescaled quantities to better match the mean-field (infinite- $N$ ) limit. Self-evidently, within a better truncation, one would also include the (field-dependent) wave-function renormalization for all fields or higher-order derivative interactions, which is however, beyond the scope of this work. The bosonic potential is initialized in the UV with the mass term  $U_\Lambda[\varphi] = \frac{1}{2} m_\Lambda^2 \varphi^2$  that is generated from the Hubbard-Stratonovich transformation. From the mean-field-renormalization procedure, we obtain an initial mass [47]

$$m_\Lambda^2 = \quad (109)$$

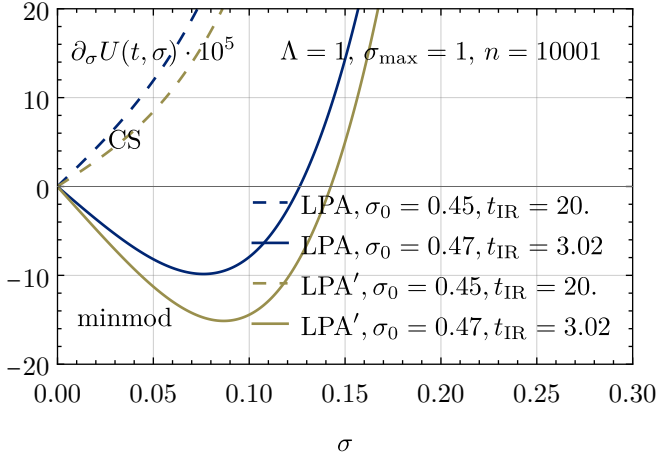
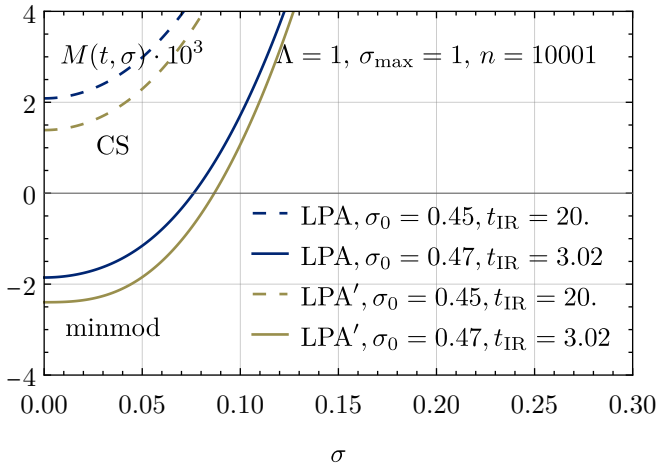
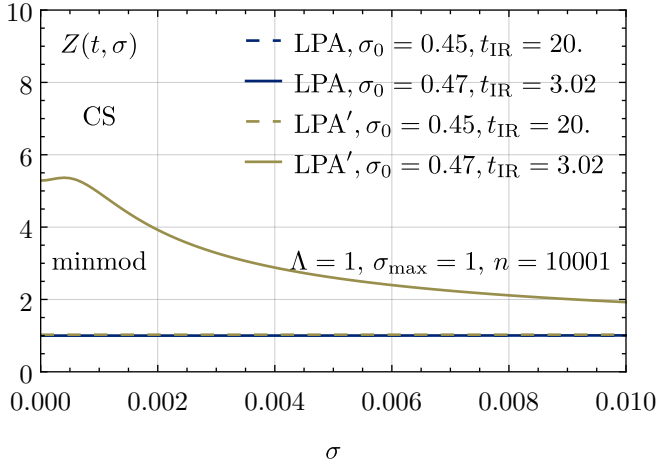
(a)  $u(t, \sigma) = \partial_\sigma U(t, \sigma)$ (b)  $M(t, \sigma) = \partial_\sigma^2 U(t, \sigma)$ (c)  $Z(t, \sigma)$ 

FIG. 15. IR results of RG flows of  $\partial_\sigma U(t, \sigma)$ ,  $M(t, \sigma) = \partial_\sigma^2 U(t, \sigma)$ , and  $Z(t, \sigma)$  with the Callan-Symanzik regulator into the symmetric and symmetry-broken regime in LPA and LPA'.

$$= \frac{d_\gamma}{4\pi} h^2 \left[ \operatorname{arccoth} \left( \sqrt{1 + \left( \frac{\Sigma_0 h}{\Lambda} \right)^2} \right) - \left( 1 + \left( \frac{\Sigma_0 h}{\Lambda} \right)^2 \right)^{-\frac{1}{2}} \right],$$

which yields the typical  $m_\Lambda^2 \propto \frac{1}{\lambda_\Lambda} \sim \ln(\Lambda)$  behavior of the asymptotically free four-fermion interaction. Here,  $d_\gamma$  is the dimensionality of the gamma matrices, which is 2 in our case. Indeed, in the limit  $N \rightarrow \infty$ , where only fermionic quantum fluctuations are taken into account, this reproduces a constant vacuum chiral condensate  $\Sigma_0$  and the limit  $\Lambda \rightarrow \infty$  can be taken to remove the cut-off. Consequently, in the  $N \rightarrow \infty$  limit the renormalized model has a unique phase diagram, whose dimensions are set by  $h \Sigma_0$ . In the following all dimensionful quantities – *i.e.* temperature  $T$ , chemical potential  $\mu$ , and chiral condensate  $\sigma$  – are to be understood in units of  $h \Sigma_0$ . Also the position of the condensate  $\Sigma_0$  in dimensionless field space is conveniently chosen to be  $\Sigma_0 = 1$ .

Since we have already mentioned chiral symmetry breaking/restoration and the vacuum (chiral) condensate, let us briefly mention that the UV theory has a  $\mathbb{Z}_2$  discrete chiral symmetry,

$$\psi \mapsto \gamma_{\text{ch}} \psi, \quad \bar{\psi} \mapsto -\bar{\psi} \gamma_{\text{ch}}, \quad \varphi \mapsto -\varphi, \quad (110)$$

and

$$U_t[\varphi] \mapsto U_t[-\varphi], \quad m_t[\varphi] \mapsto -m_t[-\varphi], \quad (111)$$

where  $\gamma_{\text{ch}}$  is the two-dimensional analog of the chiral gamma matrix  $\gamma^5$ . This chiral symmetry can be spontaneously broken by the attractive fermionic quantum fluctuations and at least in the  $N \rightarrow \infty$  limit one finds a nonzero chiral condensate<sup>23</sup>  $\sigma_0(\mu, T) \neq 0$  for small values of the chemical potential  $\mu$  and temperature  $T$  –  $\Sigma_0 = \sigma_0(0, 0) = 1$ .

A long standing question is whether this condensate is an artifact of the  $N \rightarrow \infty$  limit, because in 1 + 1 dimensions one would not expect condensation at nonzero temperatures, if bosonic fluctuations are taken into account. In preceding works [5, 42, 47], we indeed showed within the FRG framework in the LPA and also with the inclusion of field-independent wave-function renormalization and Yukawa coupling that condensation is an artifact of the  $N \rightarrow \infty$  limit and is only possible at  $T = 0$  in one spatial dimension. However, we also revealed that the imprint of the fermions and the chemical potential on the bosonic effective potential are still tremendous, especially for small temperatures, and necessitate state of the art numerics that can deal with nonanalyticities like shock waves within the FRG flow equations.

Within this work, we are interested in extending the truncation to the inclusion of a field-dependent Yukawa coupling/fermion mass and to inspect their impact on

<sup>23</sup> Within this work we ignore the possibility of spatially inhomogeneous chiral condensation and refer to Refs. [5, 133–136] for further discussion and references.

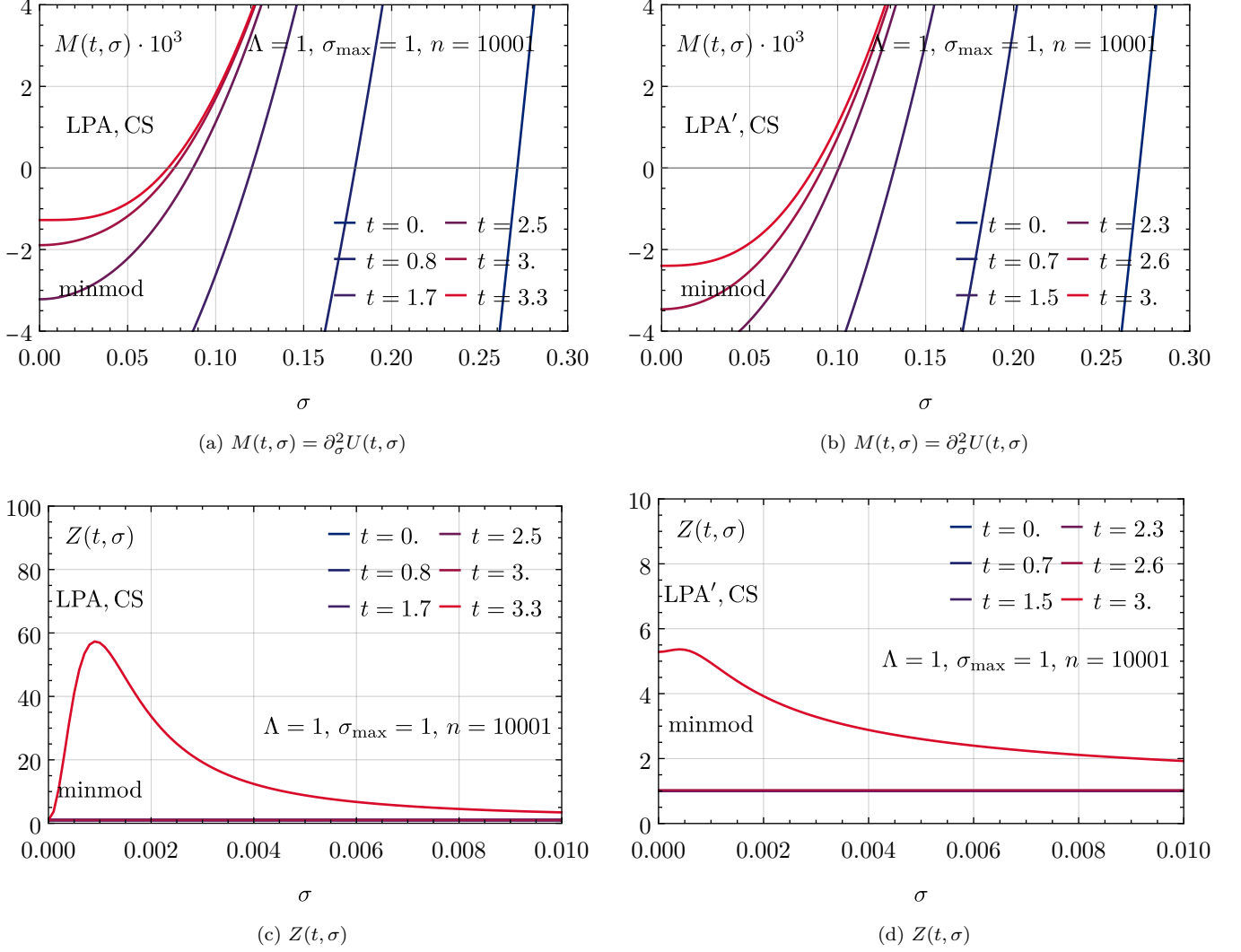


FIG. 16. RG flows of  $M(t, \sigma) = \partial_\sigma^2 U(t, \sigma)$  and  $Z(t, \sigma)$  with the Callan-Symanzik regulator in the symmetry-broken regime in LPA and LPA'.

the dynamics in field-space during the RG flow. Hereby, our strategy is as follows:

First, we recapitulate the RG flow equations for our truncation without explicit derivation. Nevertheless, we briefly discuss their general structure w.r.t. to our new approach and compare it to the zero-dimensional fermion-boson model from Section III. Second, we turn to some explicit RG flows. Here, we will solve the flow equations for a specific point in the  $\mu$ - $T$ -phase diagram and specific choice of  $N$  and compare the results for two different approximations – LPA (constant Yukawa coupling) and scLPA (field-dependent Yukawa coupling).

### 1. Flow equations

Let us start with the RG flow equations for the GNY model. All details of their derivation as well as the cor-

responding results for the Matsubara sums can be found in Refs. [42] and are not repeated here.

For their derivation we have used dimensionally reduced Litim regulators for the bosons and fermions that solely regulate the spatial momenta and keep the Matsubara frequencies untouched. This ensures Silver-Blaze symmetry and the correct pole structure of the propagators, but introduces deviations for the  $T \rightarrow 0$  limit. The flow equation for the scale-dependent effective potential, evaluated for a constant bosonic background field configuration  $\varphi(x) = \sigma$ , reads

$$\begin{aligned} \partial_t U(t, \sigma) = & -A_d \frac{1}{N} k^{d+2} T \sum_{n=-\infty}^{\infty} \frac{1}{\omega_n^2 + E_b^2} + \quad (112) \\ & + A_d d_\gamma k^{d+2} T \sum_{n=-\infty}^{\infty} \frac{1}{(\nu_n + i\mu)^2 + E_f^2}, \end{aligned}$$

where  $d = 1$  is the number of spatial dimensions,

$$A_d = \frac{\Omega_d}{d(2\pi)^d}, \quad \Omega_d = \frac{2\pi^{\frac{d}{2}}}{\Gamma(\frac{d}{2})}, \quad (113)$$

and

$$\omega_n = 2\pi T n, \quad \nu_n = 2\pi T \left(n + \frac{1}{2}\right), \quad (114)$$

are the Matsubara frequencies for bosons and fermions, respectively. The bosonic and fermionic energies are given by

$$E_b^2 = k^2 + \partial_\sigma^2 U(t, \sigma), \quad E_f^2 = k^2 + m^2(t, \sigma). \quad (115)$$

From this, it is straightforward to derive the flow equation for the second derivative of the bosonic potential  $M(t, \sigma) = \partial_\sigma^2 U(t, \sigma)$ ,

$$\begin{aligned} \partial_t M = & \quad (116) \\ = & \frac{\partial}{\partial \sigma} \left( A_d \frac{1}{N} k^{d+2} (\partial_\sigma M) T \sum_{n=-\infty}^{\infty} \frac{1}{[\omega_n^2 + E_b^2]^2} \right) + \\ & - A_d d_\gamma k^{d+2} 2 [m \partial_\sigma^2 m + (\partial_\sigma m)^2] \times \\ & \times T \sum_{n=-\infty}^{\infty} \frac{1}{[(\nu_n + i\mu)^2 + E_f^2]^2} + \\ & + A_d d_\gamma k^{d+2} 8 m^2 (\partial_\sigma m)^2 T \sum_{n=-\infty}^{\infty} \frac{1}{[(\nu_n + i\mu)^2 + E_f^2]^3}. \end{aligned}$$

Similarly, one can derive the flow equation for the field-dependent fermion mass [42, Eq. (E.110) – the sign of the boson tadpole contribution is wrong in the reference],

$$\begin{aligned} \partial_t m(t, \sigma) = & \quad (117) \\ = & A_d \frac{1}{N} (\partial_\sigma^2 m) k^{d+2} T \sum_{n=-\infty}^{\infty} \frac{1}{[\omega_n^2 + E_b^2]^2} + \\ & - 2 A_d \frac{1}{N} m (\partial_\sigma m)^2 k^{d+2} \times \\ & \times \text{Re} \left( T \sum_{n=-\infty}^{\infty} \frac{1}{[\omega_n^2 + E_b^2]^2} \frac{1}{(\nu_n + i\mu)^2 + E_f^2} + \right. \\ & \left. + T \sum_{n=-\infty}^{\infty} \frac{1}{\omega_n^2 + E_b^2} \frac{1}{[(\nu_n + i\mu)^2 + E_f^2]^2} \right), \end{aligned}$$

where we did not indicate the  $t$  and  $\sigma$  dependence of the fermion mass on the r.h.s..

Note that structurally as well as on the level of the Feynman graphs, the RG flow equation of this example

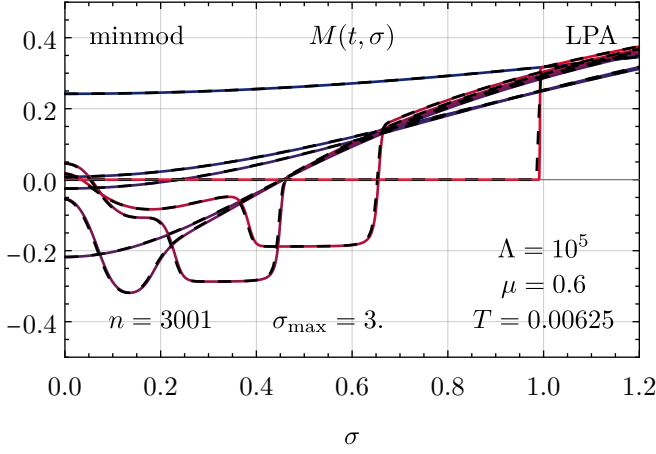
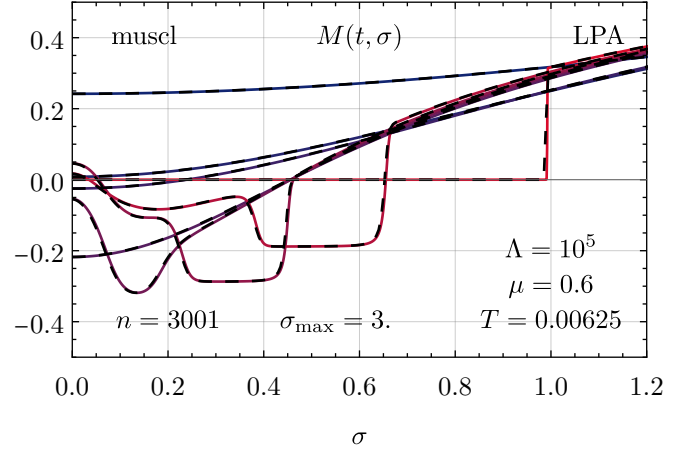
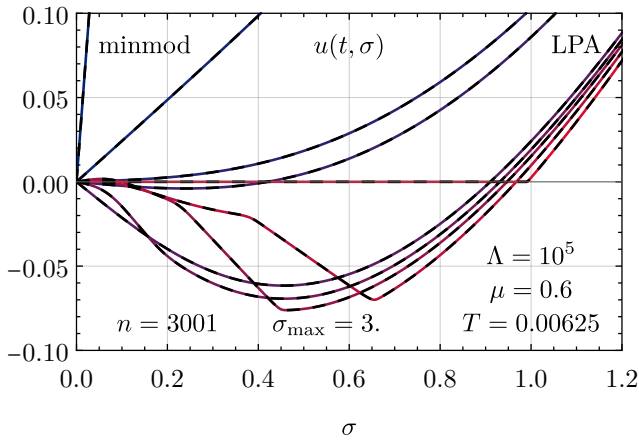
is identical to Eqs. (33) and (34) – apart from the symmetry properties of the fermion mass. Again, we find that the tadpole contributions in both equations correspond to diffusion type operators on the PDE level with complicated diffusion coefficients, while the self-energy diagrams turn out to be of the advective type and can be interpreted as Hamiltonians and therefore be treated with the KT-HJ scheme. However, as before, we experienced slightly better numerical stability and convergence when treating the bosonic contribution on the r.h.s. of Eq. (116) with the conservative KT scheme Eq. (78) and all other parts of the PDE system with the KT-HJ scheme.

## 2. RG flows

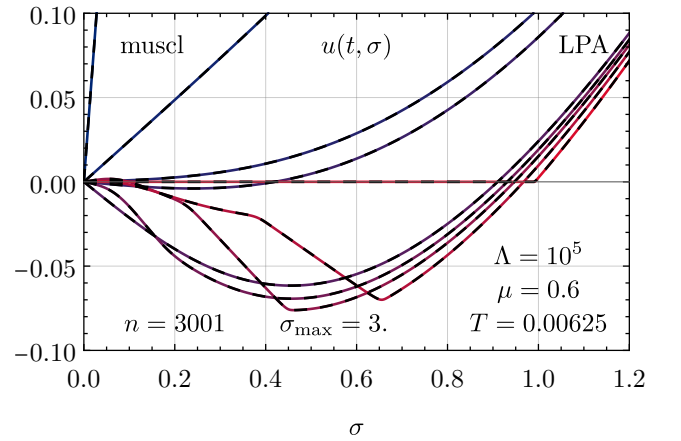
Let us now turn to the RG flows of the GNY model. Here, we shall focus on a single point in the  $\mu$ - $T$ -phase diagram, which is located at  $\mu = 0.6$  and  $T = 0.00625$ . This perfectly suffices to demonstrate the performance of our numerical scheme and a detailed reanalysis of the entire phase diagram with the present numerics is postponed to future work. Furthermore, w.l.o.g. we set the number of fermionic flavors to  $N = 16$ . These parameters turn out to be a challenging test case for our numerical scheme due to the following reasons: We are working at rather large chemical potential and small temperature. Still, the chemical potential is not too large, such that in the  $N \rightarrow \infty$  limit, the GNY model is in the phase of spontaneous discrete chiral symmetry breaking. For  $N = 16$ , however, we expect the condensate to vaporize at nonzero temperature, while the imprint of the fermions on the dynamics of the bosonic effective potential (and field-dependent fermion mass) is still significant. Furthermore, exactly for these values there are reference solutions available from previous works [5, 42, 47], which we can use for comparison. These solutions were obtained in LPA with the KT scheme applied to  $u(t, \sigma) = \partial_\sigma U(t, \sigma)$ .

Hence, let us start with the first test of our new setup. For the start, we work in the LPA and with a constant Yukawa coupling, *i.e.*,  $m(t, \sigma) = \sigma$ . However, in contrast to our previous work and reference solution, we use the flow equation for  $M(t, \sigma) = \partial_\sigma^2 U(t, \sigma)$ , namely Eq. (116), and apply the KT scheme to the conservative part, while the fermionic contributions are treated with the KT-HJ scheme. The results for the RG flow of  $M(t, \sigma)$  and  $u(t, \sigma) = \partial_\sigma U(t, \sigma)$  are shown in Figs. 17–19 for three different flux limiters – minmod, muscl, and superbee, which all show identical results.

We find perfect agreement of our new numerical scheme with the reference solution, which is indicated by the black dashed lines in the plots and which has been computed with the KT scheme for  $u$ . This is a strong cross-check and proves that the conservative KT scheme can also be applied on the level of the field-dependent mass  $M(t, \sigma) = \partial_\sigma^2 U(t, \sigma)$  instead of  $u(t, \sigma) = \partial_\sigma U(t, \sigma)$ . The independence of the results from the flux limiter is

(a)  $M(t, \sigma) = \partial_\sigma^2 U(t, \sigma)$  at  $\mu = 0.6$ ,  $T = 0.015$ (a)  $M(t, \sigma) = \partial_\sigma^2 U(t, \sigma)$  at  $\mu = 0.6$ ,  $T = 0.015$ 

—  $t = 0$ . —  $t = 10.4$  —  $t = 11.2$  —  $t = 11.3$  —  $t = 11.9$   
 —  $t = 12$ . —  $t = 12.1$  —  $t = 12.3$  —  $t = 21$ .

(b)  $u(t, \sigma) = \partial_\sigma U(t, \sigma)$  at  $\mu = 0.6$ ,  $T = 0.0625$ 

—  $t = 0$ . —  $t = 10.4$  —  $t = 11.2$  —  $t = 11.3$  —  $t = 11.9$   
 —  $t = 12$ . —  $t = 12.1$  —  $t = 12.3$  —  $t = 21$ .

(b)  $u(t, \sigma) = \partial_\sigma U(t, \sigma)$  at  $\mu = 0.6$ ,  $T = 0.0625$ 

FIG. 17. RG flow in the LPA of derivative of the effective potential  $u(t, \sigma) = \partial_\sigma U(t, \sigma)$  and the boson mass  $M(t, \sigma) = \partial_\sigma^2 U(t, \sigma)$  of the GNY model with the KT (black dashed) and KT-HJ (blue to red) scheme. For the KT-HJ  $u(t, \sigma)$  is generated by numerical integration of  $M(t, \sigma)$  in  $\sigma$ -direction.

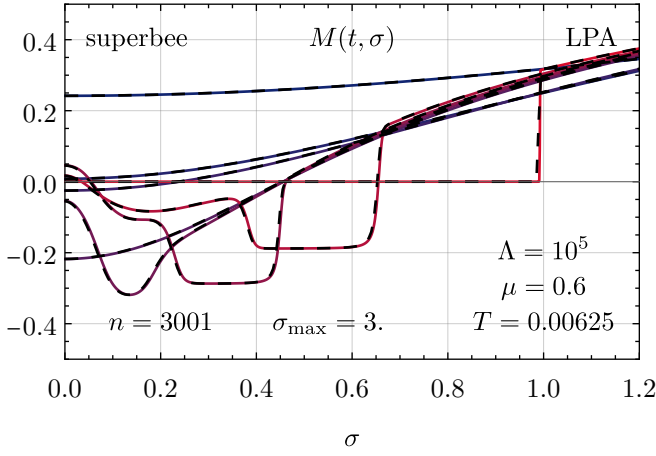
FIG. 18. RG flow in the LPA of derivative of the effective potential  $u(t, \sigma) = \partial_\sigma U(t, \sigma)$  and the boson mass  $M(t, \sigma) = \partial_\sigma^2 U(t, \sigma)$  of the GNY model with the KT (black dashed) and KT-HJ (blue to red) scheme. For the KT-HJ  $u(t, \sigma)$  is generated by numerical integration of  $M(t, \sigma)$  in  $\sigma$ -direction.

expected, since the limiters only enter the Hamilton part of the PDE system with the fermion mass, which does not evolve in LPA. Let us also briefly comment on the dynamics during the RG flow: One starts with a Gaussian potential in the UV, while at some intermediate RG time the fermionic fluctuations induce a negative curvature around the origin in field space, which signals spontaneous chiral symmetry breaking and a nontrivial minimum of the potential. This is also reflected in the zero-crossing of  $u(t, \sigma)$ . At later RG times, where  $k \approx \mu$ , the chemical potential enters from the origin in field space and induces a shock wave in  $M(t, \sigma)$  that travels outwards to larger field values. Meanwhile, the bosonic fluctuations work against the fermionic ones and push to

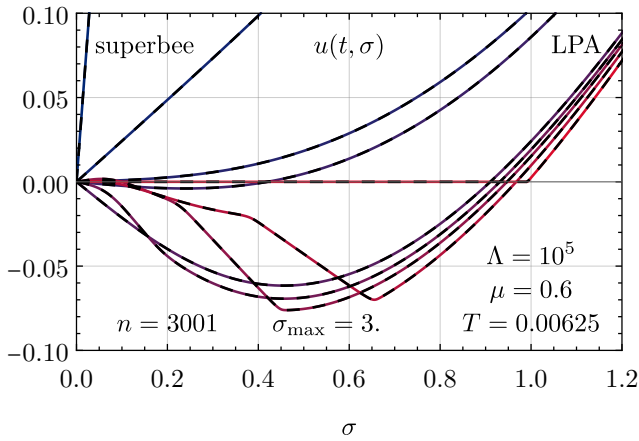
restore chiral symmetry. Finally, at the end of the flow, chiral symmetry is restored and the field-dependent mass  $M(t \rightarrow \infty, \sigma)$  is positive for all field values. The latter is not visible in the plots due to the chosen scales, but was checked in the data. Very similar dynamics was already observed in Ref. [28] for LEFT for QCD.

Next, we turn to the scLPA, where we solve the full system Eqs. (116) and (117) including the field-dependent fermion mass  $m(t, \sigma)$ . Here, of course, there are no longer reference solutions available. The only way to cross-check our results is to work at different resolutions and with different flux limiters and to check the independence of the results from these numerical details. The results for the RG flow of  $m(t, \sigma)$ ,  $M(t, \sigma) = \partial_\sigma^2 U(t, \sigma)$ , and





(a)  $M(t, \sigma) = \partial_\sigma^2 U(t, \sigma)$  at  $\mu = 0.6$ ,  $T = 0.015$



—  $t = 0$ . —  $t = 10.4$  —  $t = 11.2$  —  $t = 11.3$  —  $t = 11.9$   
 —  $t = 12$ . —  $t = 12.1$  —  $t = 12.3$  —  $t = 21$ .

(b)  $u(t, \sigma) = \partial_\sigma U(t, \sigma)$  at  $\mu = 0.6$ ,  $T = 0.0625$

FIG. 19. RG flow in the LPA of derivative of the effective potential  $u(t, \sigma) = \partial_\sigma U(t, \sigma)$  and the boson mass  $M(t, \sigma) = \partial_\sigma^2 U(t, \sigma)$  of the GNY model with the KT (black dashed) and KT-HJ (blue to red) scheme. For the KT-HJ  $u(t, \sigma)$  is generated by numerical integration of  $M(t, \sigma)$  in  $\sigma$ -direction.

$u(t, \sigma) = \partial_\sigma U(t, \sigma)$  are shown in Figs. 20–22 for the three different flux limiters – minmod, muscl, and superbee, which all show identical results. However, note that the computational time for the minmod and superbee limiters increased so drastically while enlarging the number of grid points that we solely show results for  $N = 1001$ , while improving the resolution for the muscl limiter was no problem at all. We speculate that this might be linked to the fact that minmod and superbee are both on the extreme ends (minimal and maximal diffusion respectively) within the class of second-order accurate total variation diminishing limiters and the problem at hand might require a medium amount of numerical diffusion for optimal performance.

Let us now turn to the explicit results. Basically, we find almost the same dynamics for  $M(t, \sigma)$  and  $u(t, \sigma)$  as in the LPA case with constant Yukawa coupling. Especially the final IR shape of  $M(t \rightarrow \infty, \sigma)$  and  $u(t \rightarrow \infty, \sigma)$  is almost identical to the LPA case. For direct comparison, we plotted the LPA results as black dashed lines in the plots. This behavior is not too surprising, if one inspects the flow of the fermion mass  $m(t, \sigma)$ . Here, we solely observe deviations from the linear behavior in the region of small fields  $\sigma < 1$  – hence at field values smaller than the intermediate minimum of the potential. An interesting observation is that the fermion mass  $m(t, \sigma)$  develops a cusp at the position, where the boson mass jumps. Furthermore, it seems as if the fermion mass  $m(t, \sigma)$  tries to approach a constant function at small fields that is given by the chemical potential. Indeed, we found by studying RG flows at different  $\mu$  and even lower  $T$  that the fermion mass  $m(t, \sigma)$  at small fields approaches  $\pm\mu$  in the IR limit, which might be linked to the Silver-Blaze property of the model. However, a more detailed analysis of this behavior is postponed to future work.

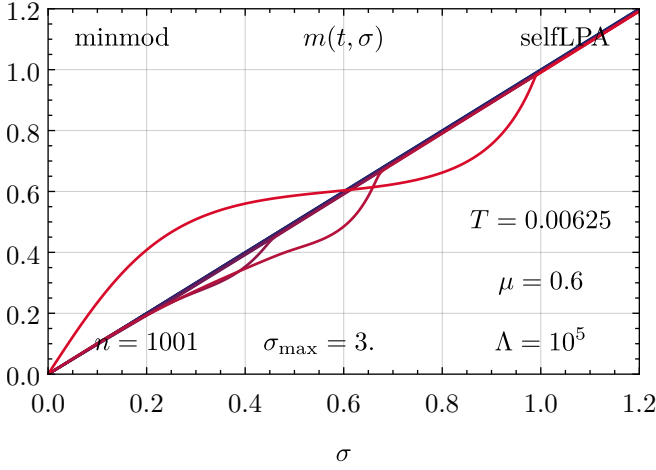
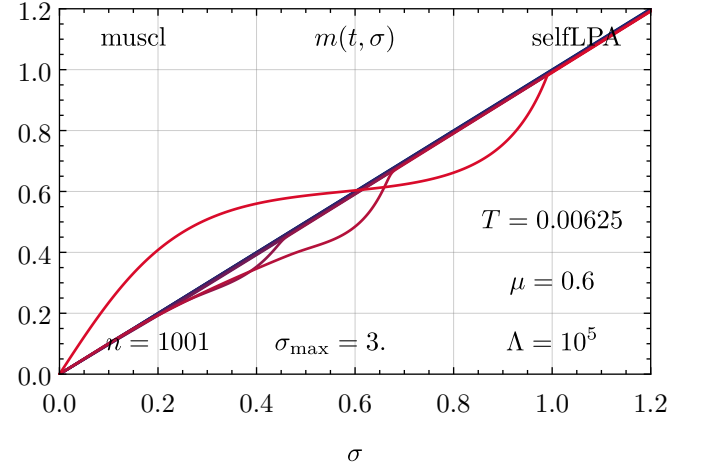
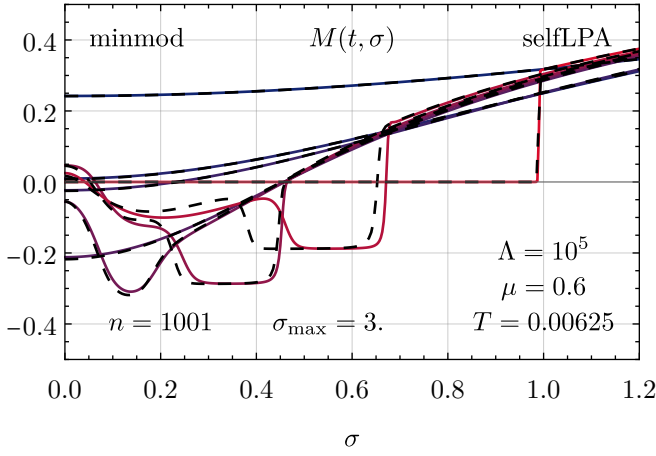
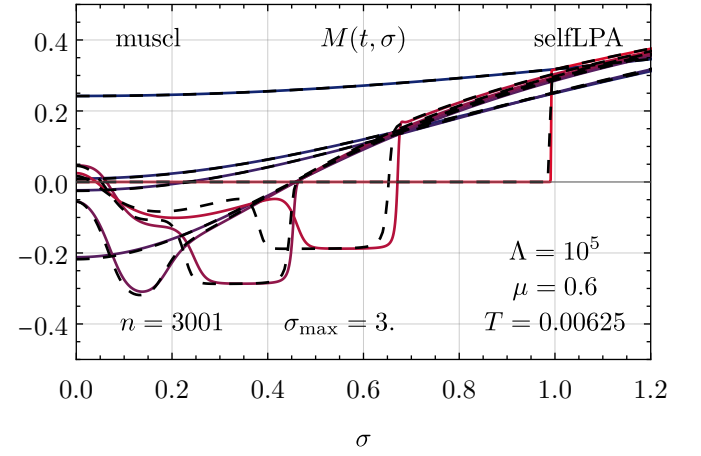
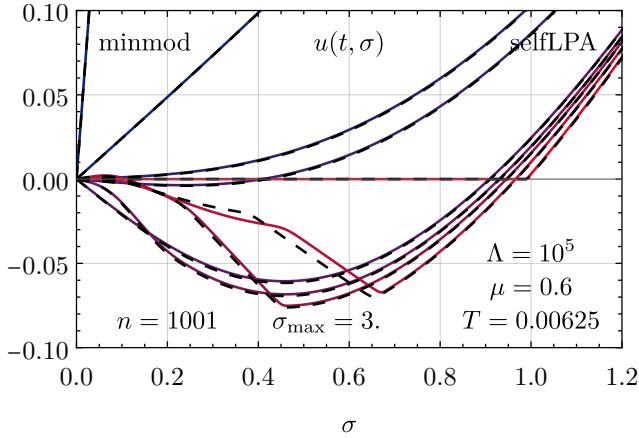
Instead, let us close our discussion by noting that symmetry restoration – even at small temperatures – seems to be a robust feature of the GNY model in  $1+1$  dimensions at finite  $N$  (non)zero chemical potential.

Additionally, we remark that our new interpretation and numerical implementation of RG flow equations in terms of HJ systems and conservation laws works perfectly fine for the inclusion of field-dependent Yukawa couplings.

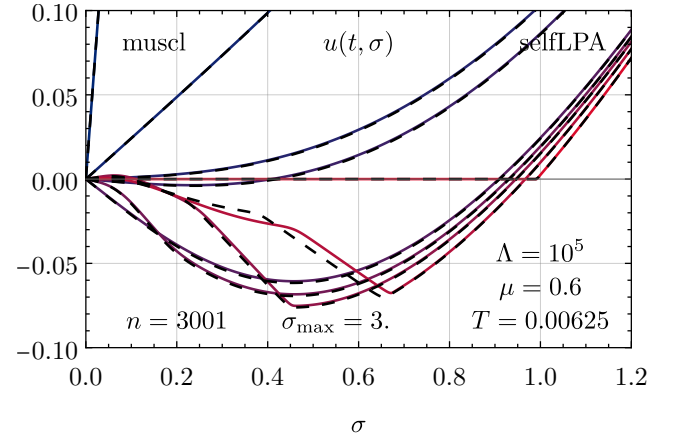
## VIII. CONCLUSIONS AND OUTLOOK

In this work we set out to connect conceptual advances in the understanding of the Wetterich equation with concrete progress on its numerical treatment. Starting from the observation that the flow of two-point functions can be interpreted as a viscous HJB equation, we emphasized that this perspective not only clarifies the advective, diffusive, and nonconservative contributions to FRG flows, but also allows the systematic adaptation of established numerical methods. The structures identified on a functional level carried through a range of projected PDEs, which initially prompted the identification on functional level.

Our primary testbed has been the zero-dimensional fermion-boson model, which proved to be structurally extremely rich. In this setting we developed and benchmarked the presented KT-HJ-hybrid scheme, combining the novel insights with the stability and proven robustness of finite volume methods. Using the KT-HJ scheme to deal with – on the level of the CFD/finite volume formulation – nonconservative contributions has proven very promising. The scheme performed well in zero spacetime dimensions and, within the scope of this work, represents the most reliable approach we were able to

(a)  $m(t, \sigma)$  at  $\mu = 0.6$ ,  $T = 0.0625$ (a)  $m(t, \sigma)$  at  $\mu = 0.6$ ,  $T = 0.0625$ (b)  $M(t, \sigma) = \partial_\sigma^2 U(t, \sigma)$  at  $\mu = 0.6$ ,  $T = 0.0625$ (b)  $M(t, \sigma) = \partial_\sigma^2 U(t, \sigma)$  at  $\mu = 0.6$ ,  $T = 0.0625$ 

—  $t = 0$ . —  $t = 10.4$  —  $t = 11.2$  —  $t = 11.3$  —  $t = 11.9$   
 —  $t = 12$ . —  $t = 12.1$  —  $t = 12.3$  —  $t = 21$ .

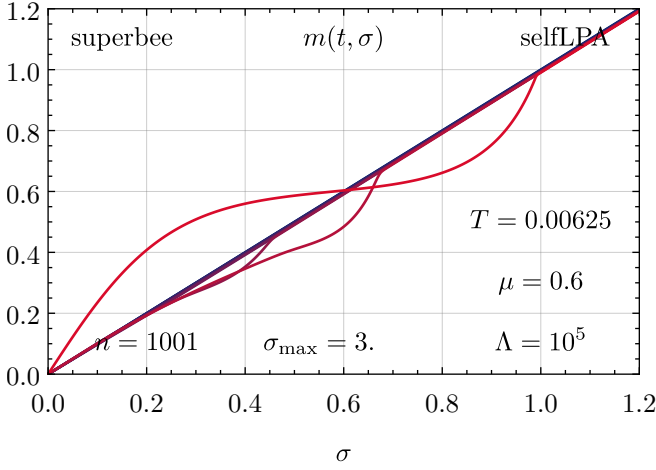
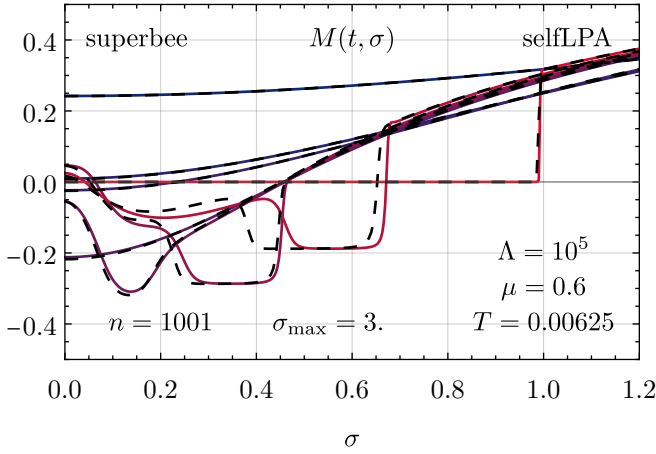
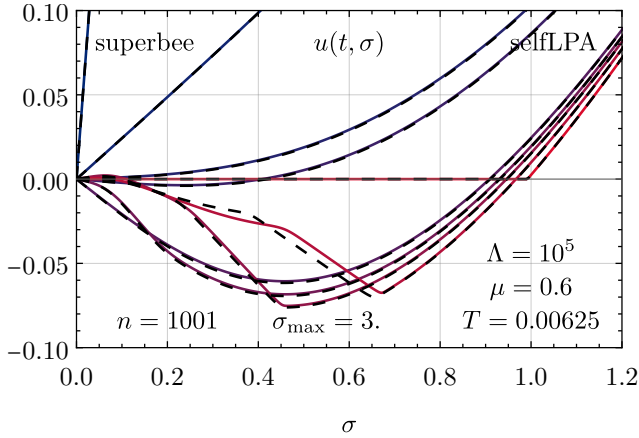
(c)  $u(t, \sigma) = \partial_\sigma U(t, \sigma)$  at  $\mu = 0.6$ ,  $T = 0.0625$ 

—  $t = 0$ . —  $t = 10.4$  —  $t = 11.2$  —  $t = 11.3$  —  $t = 11.9$   
 —  $t = 12$ . —  $t = 12.1$  —  $t = 12.3$  —  $t = 21$ .

(c)  $u(t, \sigma) = \partial_\sigma U(t, \sigma)$  at  $\mu = 0.6$ ,  $T = 0.0625$ 

FIG. 20. RG flow in the scLPA of derivative of the effective potential  $u(t, \sigma) = \partial_\sigma U(t, \sigma)$ , the boson mass  $M(t, \sigma) = \partial_\sigma^2 U(t, \sigma)$ , and the fermion mass  $m(t, \sigma)$  of the GNY model with the KT-HJ (blue to red) scheme compared to the LPA result from the KT scheme (black dashed). For the KT-HJ  $u(t, \sigma)$  is generated by numerical integration of  $M(t, \sigma)$  in  $\sigma$ -direction.

FIG. 21. RG flow in the scLPA of derivative of the effective potential  $u(t, \sigma) = \partial_\sigma U(t, \sigma)$ , the boson mass  $M(t, \sigma) = \partial_\sigma^2 U(t, \sigma)$ , and the fermion mass  $m(t, \sigma)$  of the GNY model with the KT-HJ (blue to red) scheme compared to the LPA result from the KT scheme (black dashed). For the KT-HJ  $u(t, \sigma)$  is generated by numerical integration of  $M(t, \sigma)$  in  $\sigma$ -direction.

(a)  $m(t, \sigma)$  at  $\mu = 0.6$ ,  $T = 0.0625$ (b)  $M(t, \sigma) = \partial_\sigma^2 U(t, \sigma)$  at  $\mu = 0.6$ ,  $T = 0.0625$ 

—  $t = 0$ . —  $t = 10.4$  —  $t = 11.2$  —  $t = 11.3$  —  $t = 11.9$   
 —  $t = 12$ . —  $t = 12.1$  —  $t = 12.3$  —  $t = 21$ .

(c)  $u(t, \sigma) = \partial_\sigma U(t, \sigma)$  at  $\mu = 0.6$ ,  $T = 0.0625$ 

FIG. 22. RG flow in the scLPA of derivative of the effective potential  $u(t, \sigma) = \partial_\sigma U(t, \sigma)$ , the boson mass  $M(t, \sigma) = \partial_\sigma^2 U(t, \sigma)$ , and the fermion mass  $m(t, \sigma)$  of the GNY model with the KT-HJ (blue to red) scheme compared to the LPA result from the KT scheme (black dashed). For the KT-HJ  $u(t, \sigma)$  is generated by numerical integration of  $M(t, \sigma)$  in  $\sigma$ -direction.

construct on the basis of extensive numerical experimentation. First applications to higher-dimensional models, including a  $\mathbb{Z}_2$ -symmetric scalar theory in  $d = 3$  and the Gross-Neveu-Yukawa model in  $d = 1 + 1$ , further indicate that the method can be successfully generalized to physically relevant systems. Extending these developments to other models and deepening the analysis of the  $\mathbb{Z}_2$  and Gross-Neveu-Yukawa systems are natural next steps, and we expect them to provide new insights into both the method as well as the models.

Despite the promising prospects of our developments, they should be regarded as a first step rather than a definitive solution. More advanced or specialized schemes for HJB equations, possibly tailored to the specific non-linear structures encountered in FRG flows, may lead to even more stable and efficient numerical treatments. Exploring these alternatives, and testing them in both toy models and higher-dimensional theories, will be a worthwhile and necessary direction for future work. We made a similar conclusion and in a sense warnings in our previous works [2–4, 6, 47] using adapted KT-finite-volume-schemes for the numerical solution of conservative advection-diffusion-source/sink equations. In the present context we feel obliged to stress this even more: Conceptually we feel that it should be possible to treat the PDE-system of this work numerically as coupled HJB equations without the need to split off parts as conservative equations. The adapted KT-HJ-scheme for the semi-discrete PDE-systems studied in this work is not ideal for this, which prompted us to split off purely conservative parts. The coupling of PDEs, externally driven discontinuities (*e.g.* by the chemical potential), or especially the approximation of velocities/wave speeds might be responsible for that. Our hope is that some ideas and aspects raised in this work will spark further numerical developments. As with our testcases I-IV for the zero dimensional  $O(N)$  model (in this work test 0), we hope that tests 1-3 for our zero dimensional fermion-boson model will be used in the future to benchmark FRG numerics for coupled systems of scale- and field-dependent couplings. We would truly be delighted to see a numerical scheme in future works, outperforming our developments made here. Progress in pushing truncations to ever higher sophistication – often aided by powerful computer algebra systems and significant human effort – can only translate into genuine advances if numerical methods keep pace! At present, we feel that this balance is not yet achieved.

Within the broader landscape of methods for quantum field theory and statistical physics, the FRG both benefits from and suffers under its inherently nonperturbative character. When applied to genuinely nonperturbative problems, truncations are a practical necessity, yet their reliability is difficult to judge. Assessing the quality of a truncation typically requires *a posteriori* knowledge, accumulated experience, and the study of apparent convergence. Such an assessment, however, is only meaningful if based on robust and appropriate numerical schemes – particularly when the aim is to analyze systems on a

fundamental rather than an effective level.

Beyond the numerical aspects, the identification of HJB structures in FRG flow equations may be key for further theoretical developments. The notion of viscosity solutions as physical solutions to (F)RG flow equations seems very natural and in the spirit of the underlying Wilson's RG-approach. The interpretation of the FRG as an infinite-dimensional stochastic optimal control problem might open up connections of the FRG to fields and methods not explored so far. Given the extreme complexity and practical challenges in solving the explicit PDEs derived within the FRG, such structural connections and the insights they provide may become increasingly important for the future of the field.

## ACKNOWLEDGMENTS

The authors are grateful for the support of the following people without whom this work would not have been successful: The authors thank J. Braun, M. Buballa, F. Ihssen, D. H. Rischke, F. Sattler, J. Stoll, and N. Wink for various discussions during different stages of this project. The authors are especially grateful to E. Grossi and N. Zorbach for numerous in depth discussions about numerics for PDE systems and their implementation, critical comments on preliminary results, as well as many inspiring ideas and suggestions for the present work. The authors are also grateful to M. Scherer, R. Grauer, and K. Kormann for interesting discussions on PDEs underlying the FRG and possible numeric approaches. The authors also thank F. Atteneder, S. Bernuzzi, H. Gies, E. Oevermann, C. Schmidt, M. Schröfl, T. Stötzl, A. Wipf for comments and discussions on this project at the ITP in Jena. The authors are grateful to G. Pfeifer for his work on a related project and crosschecking the flow equations of the three-dimensional  $\mathbb{Z}_2$  model. The authors thank B. Alt for literature suggestions and discussions on HJB equations and optimal control theory. The authors thank J. Stoll and N. Zorbach for valuable comments and enlightening discussions on the content and the first drafts of the manuscript.

## Appendix A: Correlation and vertex functions of the zero-dimensional model

In this appendix we present explicit expressions for the correlation and vertex functions at physical point – here  $\varphi = 0 = \bar{\vartheta} = \vartheta$  – of the zero-dimensional model introduced in Section III. The relevant governing equations were introduced in Section III A.

### 1. Connected correlation functions

In this subsection we provide expressions for the first few relevant connected correlation functions based on the

Schwinger function (20).

For example, the connected two-point correlation function for the bosonic field is given by

$$\begin{aligned} \langle \phi^2 \rangle_c &= \left. \frac{\delta^2 \mathcal{W}(\tilde{\eta}, \eta, J)}{\delta J^2} \right|_{J=0, \tilde{\eta}=0, \eta=0} = \\ &= \langle \phi^2 \rangle - \langle \phi \rangle^2 = \langle \phi^2 \rangle. \end{aligned} \quad (\text{A1})$$

Here, we used the fact that the expectation value  $\langle \phi \rangle$  vanishes due to the symmetry of the action under  $\phi \rightarrow -\phi$  (without the additional term  $-c\phi$  in the potential). Similarly, we obtain the connected four-point correlation function for the bosonic field in terms of usual expectation values,

$$\begin{aligned} \langle \phi^4 \rangle_c &= \left. \frac{\delta^4 \mathcal{W}(\tilde{\eta}, \eta, J)}{\delta J^4} \right|_{J=0, \tilde{\eta}=0, \eta=0} = \\ &= \langle \phi^4 \rangle - 3 \langle \phi^2 \rangle^2. \end{aligned} \quad (\text{A2})$$

Quantities like these serve as benchmark values for the FRG calculations in this work. In addition, we use the connected two-point correlation function for the fermionic fields

$$\langle \tilde{\theta} \theta \rangle_c = \left. \frac{\delta^2 \mathcal{W}(\tilde{\eta}, \eta, J)}{\delta(-\eta) \delta \tilde{\eta}} \right|_{J=0, \tilde{\eta}=0, \eta=0} = \langle \tilde{\theta} \theta \rangle \quad (\text{A3})$$

and the connected four-point correlation function of fermionic and bosonic fields

$$\begin{aligned} \langle \tilde{\theta} \theta \phi^2 \rangle_c &= \left. \frac{\delta^4 \mathcal{W}(\tilde{\eta}, \eta, J)}{\delta(-\eta) \delta \tilde{\eta} \delta J^2} \right|_{J=0, \tilde{\eta}=0, \eta=0} = \\ &= \langle \tilde{\theta} \theta \phi^2 \rangle - \langle \tilde{\theta} \theta \rangle \langle \phi^2 \rangle, \end{aligned} \quad (\text{A4})$$

which can be seen as the expectation value of an interaction/scattering of a fermion-antifermion pair with two bosons.

### 2. Vertex functions

In this subsection we provide expressions for the first few relevant vertex functions based on the EAA (21), *i.e.* its derivatives (22).

First, we consider the vertex function for two bosonic fields, which is the inverse of the full propagator. In terms of connected correlation functions, it reads

$$\Gamma^{\varphi\varphi} = \langle \phi^2 \rangle_c^{-1}. \quad (\text{A5})$$

Analogously, we obtain the fermionic two-point vertex function in terms of connected correlation functions,

$$\Gamma^{\bar{\vartheta}\vartheta} = -\Gamma^{\bar{\vartheta}\vartheta} = -\langle \tilde{\theta} \theta \rangle_c^{-1}. \quad (\text{A6})$$

The other components of the full two-point function vanish. For the nonvanishing components of the four-point vertex functions (up to permutations of the fields), we find

$$\Gamma^{\varphi\varphi\varphi\varphi} = -\langle\phi^4\rangle_c \langle\phi^2\rangle_c^{-4}, \quad (\text{A7})$$

$$\Gamma^{\varphi\varphi\vartheta\vartheta} = \langle\phi^2\tilde{\theta}\theta\rangle_c \langle\tilde{\theta}\theta\rangle_c^{-2} \langle\phi^2\rangle_c^{-2}. \quad (\text{A8})$$

Note that these formulae are valid for arbitrary choices of the functions  $H(\phi)$  and  $U(\phi)$  which obey the conditions mentioned above.

## Appendix B: Flow equations from exact inversion of the full field-dependent two-point function

This appendix is devoted to the derivation of the flow equation for the EAA with full field dependence and an explicit calculation of the inverse of the full two-point function as well as the trace on the right hand side of the Wetterich equation. For the sake of clearness, we recapitulate the Wetterich equation (1),

$$\partial_t \bar{\Gamma}(t, \Phi) = \quad (\text{B1})$$

$$= \text{STr} \left[ \left( \frac{1}{2} \partial_t R(t) \right) (\bar{\Gamma}^{(2)}(t, \Phi) + R(t))^{-1} \right].$$

Hence, as the first ingredient, we need the full two-point function  $\Gamma^{(2)}(t, \Phi) = \bar{\Gamma}^{(2)}(t, \Phi) + R(t)$ , which has to be inverted. From our (exact) ansatz and the matrix representation of the regulator,

$$R = \begin{pmatrix} R^{\varphi\varphi} & R^{\varphi\vartheta} & R^{\varphi\tilde{\vartheta}} \\ R^{\vartheta\varphi} & R^{\vartheta\vartheta} & R^{\vartheta\tilde{\vartheta}} \\ R^{\tilde{\vartheta}\varphi} & R^{\tilde{\vartheta}\vartheta} & R^{\tilde{\vartheta}\tilde{\vartheta}} \end{pmatrix} = \begin{pmatrix} r_b & 0 & 0 \\ 0 & 0 & r_f \\ 0 & -r_f & 0 \end{pmatrix}, \quad (\text{B2})$$

we find for the single components in field space,

$$(\bar{\Gamma}^{(2)} + R)^{\Phi\Phi} = \quad (\text{B3})$$

$$\begin{aligned} &= \begin{pmatrix} (\bar{\Gamma}^{(2)} + R)^{\varphi\varphi} & (\bar{\Gamma}^{(2)} + R)^{\varphi\vartheta} & (\bar{\Gamma}^{(2)} + R)^{\varphi\tilde{\vartheta}} \\ (\bar{\Gamma}^{(2)} + R)^{\vartheta\varphi} & (\bar{\Gamma}^{(2)} + R)^{\vartheta\vartheta} & (\bar{\Gamma}^{(2)} + R)^{\vartheta\tilde{\vartheta}} \\ (\bar{\Gamma}^{(2)} + R)^{\tilde{\vartheta}\varphi} & (\bar{\Gamma}^{(2)} + R)^{\tilde{\vartheta}\vartheta} & (\bar{\Gamma}^{(2)} + R)^{\tilde{\vartheta}\tilde{\vartheta}} \end{pmatrix} = \\ &= \begin{pmatrix} r_b + U'' + \tilde{\vartheta} H'' \vartheta & -\tilde{\vartheta} H' & H' \vartheta \\ -\tilde{\vartheta} H' & 0 & r_f + H \\ H' \vartheta & -(r_f + H) & 0 \end{pmatrix} = \\ &= \begin{pmatrix} \mathcal{B}^{-1} & 0 & 0 \\ 0 & 0 & \mathcal{F}^{-1} \\ 0 & -\mathcal{F}^{-1} & 0 \end{pmatrix} + \\ &+ \begin{pmatrix} 0 & -H' & 0 \\ -H' & 0 & 0 \\ 0 & 0 & 0 \end{pmatrix} \tilde{\vartheta} + \begin{pmatrix} 0 & 0 & H' \\ 0 & 0 & 0 \\ H' & 0 & 0 \end{pmatrix} \vartheta + \\ &+ \begin{pmatrix} H'' & 0 & 0 \\ 0 & 0 & 0 \\ 0 & 0 & 0 \end{pmatrix} \tilde{\vartheta} \vartheta, \end{aligned}$$

where we dropped the  $\varphi$  and  $t$  arguments of all functions for brevity and introduced

$$\mathcal{B}^{-1} \equiv r_b + U'', \quad \mathcal{F}^{-1} \equiv r_f + H. \quad (\text{B4})$$

We note that the matrix is antisymmetric in the purely fermionic sector. Furthermore, in the last step, we sorted the expression by powers of Grassmann numbers. This structure is crucial for the inversion of the full two-point function, because it allows us to use the most general ansatz

$$(\bar{\Gamma}^{(2)} + R)^{-1} = A + B \tilde{\vartheta} + C \vartheta + D \tilde{\vartheta} \vartheta. \quad (\text{B5})$$

Here,  $A$ ,  $B$ ,  $C$ , and  $D$  are matrices in field space that depend on  $t$  and  $\varphi$ . The simple reason, why this ansatz is the most general one, is that a series in Grassmann numbers terminates at the term, which is proportional to the product of all involved Grassmann numbers. Now, in order to determine  $A$ ,  $B$ ,  $C$ , and  $D$ , we use that

$$\mathbb{1} \stackrel{!}{=} (\bar{\Gamma}^{(2)} + R) (\bar{\Gamma}^{(2)} + R)^{-1}. \quad (\text{B6})$$

We simply expand the right hand side of this equation in powers of Grassmann numbers and compare the coefficients of the resulting series with the left hand side. Writing out the product of the matrices, we explicitly find

$$\begin{pmatrix} 1 & 0 & 0 \\ 0 & 1 & 0 \\ 0 & 0 & 1 \end{pmatrix} \stackrel{!}{=} \begin{pmatrix} \mathcal{B}^{-1} & 0 & 0 \\ 0 & 0 & \mathcal{F}^{-1} \\ 0 & -\mathcal{F}^{-1} & 0 \end{pmatrix} A + \quad (\text{B7})$$

$$+ \left[ \begin{pmatrix} \mathcal{B}^{-1} & 0 & 0 \\ 0 & 0 & \mathcal{F}^{-1} \\ 0 & -\mathcal{F}^{-1} & 0 \end{pmatrix} B + \begin{pmatrix} 0 & -H' & 0 \\ -H' & 0 & 0 \\ 0 & 0 & 0 \end{pmatrix} A \right] \tilde{\vartheta} + \quad (\text{B8})$$



$$+ \left[ \begin{pmatrix} \mathcal{B}^{-1} & 0 & 0 \\ 0 & 0 & \mathcal{F}^{-1} \\ 0 & -\mathcal{F}^{-1} & 0 \end{pmatrix} C + \begin{pmatrix} 0 & 0 & H' \\ 0 & 0 & 0 \\ H' & 0 & 0 \end{pmatrix} A \right] \vartheta + \quad (\text{B9})$$

$$+ \left[ \begin{pmatrix} \mathcal{B}^{-1} & 0 & 0 \\ 0 & 0 & \mathcal{F}^{-1} \\ 0 & -\mathcal{F}^{-1} & 0 \end{pmatrix} D + \begin{pmatrix} 0 & -H' & 0 \\ -H' & 0 & 0 \\ 0 & 0 & 0 \end{pmatrix} C - \begin{pmatrix} 0 & 0 & H' \\ 0 & 0 & 0 \\ H' & 0 & 0 \end{pmatrix} B + \begin{pmatrix} H'' & 0 & 0 \\ 0 & 0 & 0 \\ 0 & 0 & 0 \end{pmatrix} A \right] \tilde{\vartheta} \vartheta \quad (\text{B10})$$

Now, it is straight forward to solve this system by comparing the coefficients. From the left hand side and line (B7), we find

$$A = \begin{pmatrix} \mathcal{B} & 0 & 0 \\ 0 & 0 & -\mathcal{F} \\ 0 & \mathcal{F} & 0 \end{pmatrix}. \quad (\text{B11})$$

Inserting this in lines (B8) and (B9) one finds

$$\begin{aligned} B &= - \begin{pmatrix} \mathcal{B} & 0 & 0 \\ 0 & 0 & -\mathcal{F} \\ 0 & \mathcal{F} & 0 \end{pmatrix} \begin{pmatrix} 0 & -H' & 0 \\ -H' & 0 & 0 \\ 0 & 0 & 0 \end{pmatrix} \begin{pmatrix} \mathcal{B} & 0 & 0 \\ 0 & 0 & -\mathcal{F} \\ 0 & \mathcal{F} & 0 \end{pmatrix} \\ &= \begin{pmatrix} 0 & \mathcal{B} H' & 0 \\ 0 & 0 & 0 \\ \mathcal{F} H' & 0 & 0 \end{pmatrix} \begin{pmatrix} \mathcal{B} & 0 & 0 \\ 0 & 0 & -\mathcal{F} \\ 0 & \mathcal{F} & 0 \end{pmatrix} = \\ &= \begin{pmatrix} 0 & 0 & -\mathcal{B} H' \mathcal{F} \\ 0 & 0 & 0 \\ \mathcal{F} H' \mathcal{B} & 0 & 0 \end{pmatrix}. \end{aligned} \quad (\text{B12})$$

and

$$\begin{aligned} C &= - \begin{pmatrix} \mathcal{B} & 0 & 0 \\ 0 & 0 & -\mathcal{F} \\ 0 & \mathcal{F} & 0 \end{pmatrix} \begin{pmatrix} 0 & 0 & H' \\ 0 & 0 & 0 \\ H' & 0 & 0 \end{pmatrix} \begin{pmatrix} \mathcal{B} & 0 & 0 \\ 0 & 0 & -\mathcal{F} \\ 0 & \mathcal{F} & 0 \end{pmatrix} \\ &= \begin{pmatrix} 0 & 0 & -\mathcal{B} H' \\ \mathcal{F} H' & 0 & 0 \\ 0 & 0 & 0 \end{pmatrix} \begin{pmatrix} \mathcal{B} & 0 & 0 \\ 0 & 0 & -\mathcal{F} \\ 0 & \mathcal{F} & 0 \end{pmatrix} = \\ &= \begin{pmatrix} 0 & -\mathcal{B} H' \mathcal{F} & 0 \\ \mathcal{F} H' \mathcal{B} & 0 & 0 \\ 0 & 0 & 0 \end{pmatrix}. \end{aligned} \quad (\text{B13})$$

Next, we study the coefficient of  $\tilde{\vartheta} \vartheta$ , thus line (B10) and insert the previous results. Solving for  $D$  results in

$$\begin{aligned} D &= \begin{pmatrix} \mathcal{B} & 0 & 0 \\ 0 & 0 & -\mathcal{F} \\ 0 & \mathcal{F} & 0 \end{pmatrix} \left[ - \begin{pmatrix} 0 & -H' & 0 \\ -H' & 0 & 0 \\ 0 & 0 & 0 \end{pmatrix} C + \begin{pmatrix} 0 & 0 & H' \\ 0 & 0 & 0 \\ H' & 0 & 0 \end{pmatrix} B - \begin{pmatrix} H'' & 0 & 0 \\ 0 & 0 & 0 \\ 0 & 0 & 0 \end{pmatrix} A \right] = \\ &= \left[ \begin{pmatrix} 0 & \mathcal{B} H' & 0 \\ 0 & 0 & 0 \\ \mathcal{F} H' & 0 & 0 \end{pmatrix} C + \begin{pmatrix} 0 & 0 & \mathcal{B} H' \\ -\mathcal{F} H' & 0 & 0 \\ 0 & 0 & 0 \end{pmatrix} B + \begin{pmatrix} -\mathcal{B} H'' & 0 & 0 \\ 0 & 0 & 0 \\ 0 & 0 & 0 \end{pmatrix} A \right] = \\ &= \left[ \begin{pmatrix} 0 & \mathcal{B} H' & 0 \\ 0 & 0 & 0 \\ \mathcal{F} H' & 0 & 0 \end{pmatrix} \begin{pmatrix} 0 & -\mathcal{B} H' \mathcal{F} & 0 \\ \mathcal{F} H' \mathcal{B} & 0 & 0 \\ 0 & 0 & 0 \end{pmatrix} + \right. \\ &\quad + \begin{pmatrix} 0 & 0 & \mathcal{B} H' \\ -\mathcal{F} H' & 0 & 0 \\ 0 & 0 & 0 \end{pmatrix} \begin{pmatrix} 0 & 0 & -\mathcal{B} H' \mathcal{F} \\ 0 & 0 & 0 \\ \mathcal{F} H' \mathcal{B} & 0 & 0 \end{pmatrix} + \\ &\quad \left. + \begin{pmatrix} -\mathcal{B} H'' & 0 & 0 \\ 0 & 0 & 0 \\ 0 & 0 & 0 \end{pmatrix} \begin{pmatrix} \mathcal{B} & 0 & 0 \\ 0 & 0 & -\mathcal{F} \\ 0 & \mathcal{F} & 0 \end{pmatrix} \right] = \end{aligned} \quad (\text{B14})$$

$$= \begin{pmatrix} 2\mathcal{B}H'\mathcal{F}H'\mathcal{B} - \mathcal{B}H''\mathcal{B} & 0 & 0 \\ 0 & 0 & \mathcal{F}H'\mathcal{B}H'\mathcal{F} \\ 0 & -\mathcal{F}H'\mathcal{B}H'\mathcal{F} & 0 \end{pmatrix}$$

Combing the results in our ansatz (B5), we obtain the full inverse of the two-point function,

$$\begin{aligned} (\bar{\Gamma}^{(2)} + R)^{-1} &= \begin{pmatrix} \mathcal{B} & 0 & 0 \\ 0 & 0 & -\mathcal{F} \\ 0 & \mathcal{F} & 0 \end{pmatrix} + \begin{pmatrix} 0 & 0 & -\mathcal{B}H'\mathcal{F} \\ 0 & 0 & 0 \\ \mathcal{F}H'\mathcal{B} & 0 & 0 \end{pmatrix} \tilde{\vartheta} + \begin{pmatrix} 0 & -\mathcal{B}H'\mathcal{F} & 0 \\ \mathcal{F}H'\mathcal{B} & 0 & 0 \\ 0 & 0 & 0 \end{pmatrix} \vartheta + \\ &+ \begin{pmatrix} 2\mathcal{B}H'\mathcal{F}H'\mathcal{B} - \mathcal{B}H''\mathcal{B} & 0 & 0 \\ 0 & 0 & \mathcal{F}H'\mathcal{B}H'\mathcal{F} \\ 0 & -\mathcal{F}H'\mathcal{B}H'\mathcal{F} & 0 \end{pmatrix} \tilde{\vartheta} \vartheta. \end{aligned}$$

Note, that this inversion is exact and does not rely on any approximation! However, usually this exact inversion is not possible. Next, we can insert this result together with the derivative of the regulator into the Wetterich equation

$$\partial_t \bar{\Gamma}(t, \Phi) = \text{STr} \left[ \left( \frac{1}{2} \partial_t R(t) \right) (\bar{\Gamma}^{(2)}(t, \Phi) + R(t))^{-1} \right]. \quad (\text{B15})$$

Remember, that we also have to replace the left hand side with the derivative of the (exact) ansatz,

$$\partial_t \bar{\Gamma}(t, \Phi) = \tilde{\vartheta} \partial_t H(t, \varphi) \vartheta + \partial_t U(t, \varphi). \quad (\text{B16})$$

Again, we compare coefficients of Grassmann numbers on both sides of the equation. For the term without Grassmann numbers we find

$$\partial_t U = \text{STr} \left( \begin{pmatrix} \frac{1}{2} \partial_t r_b & 0 & 0 \\ 0 & 0 & \frac{1}{2} \partial_t r_f \\ 0 & -\frac{1}{2} \partial_t r_f & 0 \end{pmatrix} \begin{pmatrix} \mathcal{B} & 0 & 0 \\ 0 & 0 & -\mathcal{F} \\ 0 & \mathcal{F} & 0 \end{pmatrix} \right) = \left( \frac{1}{2} \partial_t r_b \right) \mathcal{B} - (\partial_t r_f) \mathcal{F}, \quad (\text{B17})$$

which has the well-known structure of a flow equation of the effective potential of a system with Yukawa-type interactions between bosons and fermions. For the terms linear in  $\tilde{\vartheta}$  or  $\vartheta$  we find that there is no contribution on the left hand side and the supertrace on the right hand side vanishes exactly. On the other hand, the coefficients of the  $\tilde{\vartheta} \vartheta$ -term are nontrivial on both sides. Evaluating the supertrace, we find

$$\begin{aligned} \partial_t H &= \text{STr} \left( \begin{pmatrix} \frac{1}{2} \partial_t r_b & 0 & 0 \\ 0 & 0 & \frac{1}{2} \partial_t r_f \\ 0 & -\frac{1}{2} \partial_t r_f & 0 \end{pmatrix} \cdot \begin{pmatrix} 2\mathcal{B}H'\mathcal{F}H'\mathcal{B} - \mathcal{B}H''\mathcal{B} & 0 & 0 \\ 0 & 0 & \mathcal{F}H'\mathcal{B}H'\mathcal{F} \\ 0 & -\mathcal{F}H'\mathcal{B}H'\mathcal{F} & 0 \end{pmatrix} \right) = \\ &= 2 \left( \frac{1}{2} \partial_t r_b \right) \mathcal{B}^2 \mathcal{F} (H')^2 - \left( \frac{1}{2} \partial_t r_b \right) \mathcal{B}^2 H'' + 2 \left( \frac{1}{2} \partial_t r_f \right) \mathcal{B} \mathcal{F}^2 (H')^2. \end{aligned} \quad (\text{B18})$$

Also this equation has a well-known structure: It is the flow equation of a Yukawa-type interaction or the fermionic mass term, respectively.

### Appendix C: Flow equations via projections of the Wetterich equation

In this appendix, we derive the flow equations for the effective potential and the Yukawa coupling from the Wetterich equation. Here, we resort to the standard procedure of projecting the Wetterich equation onto vertices. In our case, we have to project the Wetterich equation onto the effective potential and the Yukawa coupling. Recapitulating that (exact) ansatz for the EAA was given

by

$$\bar{\Gamma}(t, \Phi) = \tilde{\vartheta} H(t, \varphi) \vartheta + U(t, \varphi), \quad (\text{C1})$$

we can directly project onto the scale-dependent effective potential  $U(t, \varphi)$  by evaluating the Wetterich equation for  $\tilde{\vartheta} = \vartheta = 0$ . Thus, we need to evaluate all objects inside the supertrace on the r.h.s. for  $\tilde{\vartheta} = \vartheta = 0$ . Here, it actually does not matter, if one first evaluates the two-point function for vanishing fermion fields and afterwards inverts the matrix or if one proceeds the other

way around.<sup>24</sup> In any case, one finds exactly Eq. (33). However, for the projection onto the Yukawa coupling  $H(t, \varphi)$ , we first have to take derivatives with respect to

$\tilde{\vartheta}$  and  $\vartheta$  first and only afterwards set them to zero.

One obtains,

$$\begin{aligned} \partial_t H &= \left[ \frac{\partial^2}{\partial \vartheta \partial \tilde{\vartheta}} \text{STr} \left[ \left( \frac{1}{2} \partial_t R \right) (\bar{\Gamma}^{(2)} + R)^{-1} \right] \right]_{\tilde{\vartheta}=\vartheta=0} = \\ &= \left[ \text{STr} \left[ \left( \frac{1}{2} \partial_t R \right) (\bar{\Gamma}^{(2)} + R)^{-1} \Gamma^{\tilde{\vartheta}\Phi\Phi} (\bar{\Gamma}^{(2)} + R)^{-1} \Gamma^{\vartheta\Phi\Phi} (\bar{\Gamma}^{(2)} + R)^{-1} \right] - \right. \\ &\quad \left. - \text{STr} \left[ \left( \frac{1}{2} \partial_t R \right) (\bar{\Gamma}^{(2)} + R)^{-1} \Gamma^{\vartheta\tilde{\vartheta}\Phi\Phi} (\bar{\Gamma}^{(2)} + R)^{-1} \right] + \right. \\ &\quad \left. + \text{STr} \left[ \left( \frac{1}{2} \partial_t R \right) (\bar{\Gamma}^{(2)} + R)^{-1} \Gamma^{\tilde{\vartheta}\Phi\Phi} (\bar{\Gamma}^{(2)} + R)^{-1} \Gamma^{\vartheta\Phi\Phi} (\bar{\Gamma}^{(2)} + R)^{-1} \right] \right]_{\tilde{\vartheta}=\vartheta=0}. \end{aligned} \quad (\text{C2})$$

For the full propagators (evaluated for  $\tilde{\vartheta} = \vartheta = 0$ ), we can again directly invert the  $\tilde{\vartheta}$ - and  $\vartheta$ -independent part of the full two-point function (B3) and for the derivative of the regulator, we make use of the matrix representation (B2). It remains to determine the three- and four-point vertices in matrix representation and evaluated for vanishing fermion fields. In fact, these are

$$\Gamma^{\vartheta\Phi\Phi} = \begin{pmatrix} 0 & -H' & 0 \\ -H' & 0 & 0 \\ 0 & 0 & 0 \end{pmatrix}, \quad (\text{C3})$$

$$\Gamma^{\vartheta\Phi\Phi} = \begin{pmatrix} 0 & 0 & H' \\ 0 & 0 & 0 \\ H' & 0 & 0 \end{pmatrix}, \quad (\text{C4})$$

$$\Gamma^{\vartheta\tilde{\vartheta}\Phi\Phi} = \begin{pmatrix} H'' & 0 & 0 \\ 0 & 0 & 0 \\ 0 & 0 & 0 \end{pmatrix}. \quad (\text{C5})$$

Inserting these matrices into the supertraces of Eq. (C2) and evaluating the traces, we find exactly Eq. (34).

#### Appendix D: Flow equations for the $\mathbb{Z}_2$ -symmetric model

In this appendix we include additional expressions related to Section VII A including the explicit expressions for the FRG flow equations for the  $\mathbb{Z}_2$ -symmetric model of the single scalar in three Euclidean dimensions.

The full propagator within our truncation – evaluated

for  $\sigma$  – from Eq. (95) is given by

$$G_t(p_2, p_1)|_{\varphi(x)=\sigma} = (2\pi)^d \delta^{(d)}(p_2 + p_1) \mathcal{G}(t, \sigma, p_1^2), \quad (\text{D1})$$

$$\mathcal{G}(t, \sigma, p^2) = \frac{1}{U''(t, \sigma) + [Z(t, \sigma) + r_t(p^2)] p^2}. \quad (\text{D2})$$

In addition, the three- and four-point functions derived from Eq. (95) read

$$\bar{\Gamma}_t^{(3)}(p_3, p_2, p_1)|_{\varphi(x)=\sigma} = \quad (\text{D3})$$

$$\begin{aligned} &= (2\pi)^d \delta^{(d)}(p_3 + p_2 + p_1) \times \\ &\quad \times [U'''(t, \sigma) - Z'(t, \sigma) (p_3 \cdot p_2 + p_2 \cdot p_1 + p_1 \cdot p_3)], \end{aligned}$$

as well as

$$\bar{\Gamma}_t^{(4)}(p_4, p_3, p_2, p_1)|_{\varphi(x)=\sigma} = \quad (\text{D4})$$

$$\begin{aligned} &= (2\pi)^d \delta^{(d)}(p_4 + p_3 + p_2 + p_1) [U''''(t, \sigma) - Z''(t, \sigma) \times \\ &\quad \times [p_4 \cdot (p_3 + p_2 + p_1) + p_3 \cdot (p_2 + p_1) + p_2 \cdot p_1]]. \end{aligned}$$

Inserting these expressions into Eq. (98), we can evaluate the integrals and find

<sup>24</sup> In our zero-dimensional setup this is explicitly visible from Eqs. (B3) and (B15) where in both cases only the  $\tilde{\vartheta}$ - and  $\vartheta$ -independent term survives.

$$\begin{aligned} \partial_t \bar{\Gamma}^{(2)}(t, q) = & \int_p \left( \frac{1}{2} \partial_t R(t, p^2) \right) \left[ -\mathcal{G}^2(t, \sigma, p^2) [U''''(t, \sigma) + Z''(t, \sigma) (q^2 + p^2)] + \right. \\ & \left. + 2 \int_p \left( \frac{1}{2} \partial_t R(t, p^2) \right) \mathcal{G}^2(t, \sigma, p^2) \mathcal{G}(t, \sigma, (p+q)^2) [U'''(t, \sigma) + Z'(t, \sigma) [p^2 + (p+q) \cdot q]]^2 \right]. \end{aligned} \quad (\text{D5})$$

By evaluating this at  $q = 0$ , we arrive at the flow equation for the boson mass function  $M(t, \sigma)$

$$\begin{aligned} \partial_t M = & \int_p \left( \frac{1}{2} \partial_t R \right) \left[ -\mathcal{G}^2 [M'' + Z'' p^2] + \right. \\ & \left. + 2 \int_p \left( \frac{1}{2} \partial_t R \right) \mathcal{G}^3 [M' + Z' p^2]^2 \right]. \end{aligned} \quad (\text{D6})$$

Here, we stopped indicating the dependences on  $t$ ,  $\sigma$ , and  $p^2$  for the sake of the readability.

For the wave-function renormalization, however, one needs to expand the second contribution in Eq. (D5) up to order  $q^2$  and then take the derivative with respect to  $q^2$ . Lastly, one again evaluates the result at  $q = 0$  and arrives at the flow equation for the wave-function renormalization  $Z(t, \sigma)$

$$\begin{aligned} \partial_t Z = & \int_p \left( \frac{1}{2} \partial_t R \right) \left[ -\mathcal{G}^2 Z'' + \right. \\ & + 2 \mathcal{G}^2 \left( 2 \mathcal{G} Z' [(M'' + Z' p^2) + \frac{1}{2d} Z' p^2] + \right. \\ & + \dot{\mathcal{G}} (M'' + Z' p^2) [(M'' + Z' p^2) + \frac{4}{d} Z' p^2] + \\ & \left. \left. + \ddot{\mathcal{G}} (M'' + Z' p^2)^2 \frac{2}{d} p^2 \right] \right], \end{aligned} \quad (\text{D7})$$

where some propagators  $\mathcal{G}$  are retained in the expression for which the  $p^2$ -derivative is not taken yet, indicated by the dot(s). Before we can evaluate these derivatives and the remaining integrals, we need to specify the regulator shape function. Explicit expressions for Eqs. (D6) and (D7) with Callan-Symanzik regulator and Litim regulator are discussed in the following Appendices D 1 and D 2 respectively.

### 1. Callan-Symanzik regulator in three dimensions

Starting with the Callan-Symanzik regulator (102), we find that the flow equation for  $M$ , Eq. (D6), or respec-

tively for the potential  $U$  itself,

$$\partial_t U = \int_p \left( \frac{1}{2} \partial_t R \right) \mathcal{G}, \quad (\text{D8})$$

still contains an UV divergence in three Euclidean dimensions, since  $d^3 p \propto dp p^2$  and  $\mathcal{G} \propto 1/p^2$  for large momenta, while the Callan-Symanzik regulator does not contain any momentum dependence and therefore does not regulate the UV. For the flow equation of the wave-function renormalization  $Z$ , Eq. (D7), this problem does not occur, because of the higher powers of the propagators – the integrand always falls off at least like  $1/p^2$ .

In any case, we used dimensional regularization with

$$\int_p \frac{1}{(p^2 + \Delta)^n} = \frac{\Gamma(n - \frac{d}{2})}{(4\pi)^{\frac{d}{2}} \Gamma(n)} \Delta^{\frac{d}{2} - n}, \quad (\text{D9})$$

for Eq. (D8) and take two derivatives with respect to  $\sigma$  to obtain the UV renormalized flow equation for  $M$ .

In total, we find the following flow equations for the effective potential and the wave-function renormalization,

$$\partial_t M = \quad (\text{D10})$$

$$\begin{aligned} = & \frac{\partial}{\partial \sigma} \left[ \frac{k^2}{8\pi} \left( \frac{1}{\sqrt{k^2 + M}} \frac{M'}{Z^{\frac{3}{2}}} - 3 \sqrt{k^2 + M} \frac{Z'}{Z^{\frac{5}{2}}} \right) \right] = \\ = & \frac{k^2}{8\pi} \left[ \frac{1}{\sqrt{k^2 + M}} \frac{M''}{Z^{\frac{3}{2}}} - \frac{1}{2} \frac{1}{\sqrt{k^2 + M}^3} \frac{(M')^2}{Z^{\frac{3}{2}}} + \right. \\ & - 3 \frac{1}{\sqrt{k^2 + M}} \frac{M' Z'}{Z^{\frac{5}{2}}} + \frac{15}{2} \sqrt{k^2 + M} \frac{(Z')^2}{Z^{\frac{7}{2}}} + \\ & \left. - 3 \sqrt{k^2 + M} \frac{Z''}{Z^{\frac{5}{2}}} \right], \end{aligned}$$

$$\partial_t Z = \quad (\text{D11})$$

$$\begin{aligned} = & \frac{k^2}{8\pi} \left[ \frac{1}{\sqrt{k^2 + M}} \frac{Z''}{Z^{\frac{3}{2}}} - \frac{49}{24} \frac{1}{\sqrt{k^2 + M}} \frac{(Z')^2}{Z^{\frac{5}{2}}} + \right. \\ & \left. - \frac{7}{12} \frac{1}{\sqrt{k^2 + M}^3} \frac{Z' M'}{Z^{\frac{3}{2}}} + \frac{1}{8} \frac{1}{\sqrt{k^2 + M}^5} \frac{(M')^2}{Z^{\frac{1}{2}}} \right]. \end{aligned}$$

## 2. Litim regulator in three dimensions

For the Litim regulator (103) the problem of UV divergences is not present, since the regulator is local in momentum space and therefore cuts off the UV divergences via the regulator insertion  $\partial_t R$ . However, there is another problem for the Litim regulator, which is that

the regulator is not analytic in the momentum space. Hence, especially the terms involving  $\hat{\mathcal{G}}$  and  $\tilde{\mathcal{G}}$  have to be treated with care. In Ref. [42, Appendix D] one of the authors of this work provided several useful identities for derivatives of the Litim regulator and corresponding integrals, which we also use here. The final result for the flow equations of the effective potential and the wave-function renormalization is

$$\partial_t M = \tag{D12}$$

$$\begin{aligned} &= \frac{\partial}{\partial \sigma} \left( \frac{k^3}{8\pi^2} \left[ 2 \frac{1}{Z-1} \left( -\frac{1}{M+Zk^2} + \frac{1}{M+k^2} \sqrt{\frac{M+k^2}{(Z-1)k^2}} \operatorname{arccot} \left( \sqrt{\frac{M+k^2}{(Z-1)k^2}} \right) \right) M' + \right. \right. \\ &\quad \left. \left. + 2 \frac{1}{(Z-1)^2} \left( 2 + \frac{M+k^2}{M+Zk^2} - 3 \sqrt{\frac{M+k^2}{(Z-1)k^2}} \operatorname{arccot} \left( \sqrt{\frac{M+k^2}{(Z-1)k^2}} \right) \right) Z' \right] \right) = \\ &= \frac{k^3}{8\pi^2} \left[ 2 \frac{1}{Z-1} \left( -\frac{1}{M+Zk^2} + \frac{1}{M+k^2} \sqrt{\frac{M+k^2}{(Z-1)k^2}} \operatorname{arccot} \left( \sqrt{\frac{M+k^2}{(Z-1)k^2}} \right) \right) M'' + \right. \\ &\quad \left. + \frac{1}{Z-1} \frac{1}{(M+k^2)^2} \left( \frac{(M+k^2)[(M+k^2)-(Z-1)k^2]}{(M+Zk^2)^2} - \sqrt{\frac{M+k^2}{(Z-1)k^2}} \operatorname{arccot} \left( \sqrt{\frac{M+k^2}{(Z-1)k^2}} \right) \right) (M')^2 + \right. \\ &\quad \left. + 2 \frac{1}{(Z-1)^2} \left( \frac{3(M+k^2)+5(Z-1)k^2}{(M+Zk^2)^2} - 3 \frac{1}{M+k^2} \sqrt{\frac{M+k^2}{(Z-1)k^2}} \operatorname{arccot} \left( \sqrt{\frac{M+k^2}{(Z-1)k^2}} \right) \right) M' Z' + \right. \\ &\quad \left. - \frac{1}{(Z-1)^3} \left( \frac{15(M+k^2)^2+25(M+k^2)(Z-1)k^2+8[(Z-1)k^2]^2}{(M+Zk^2)^2} + \right. \right. \\ &\quad \left. \left. - 15 \sqrt{\frac{M+k^2}{(Z-1)k^2}} \operatorname{arccot} \left( \sqrt{\frac{M+k^2}{(Z-1)k^2}} \right) \right) (Z')^2 + \right. \\ &\quad \left. + 2 \frac{1}{(Z-1)^2} \left( 2 + \frac{M+k^2}{M+Zk^2} - 3 \sqrt{\frac{M+k^2}{(Z-1)k^2}} \operatorname{arccot} \left( \sqrt{\frac{M+k^2}{(Z-1)k^2}} \right) \right) Z' \right]. \end{aligned}$$

$$\partial_t Z = \tag{D13}$$

$$\begin{aligned} &= \frac{k^2}{288\pi^2} \left[ -72 \frac{1}{Z-1} \left( \frac{k}{M+Zk^2} - \frac{1}{\sqrt{M+k^2}\sqrt{Z-1}} \operatorname{arccot} \left( \sqrt{\frac{M+k^2}{(Z-1)k^2}} \right) \right) Z'' + \right. \\ &\quad \left. + \frac{1}{(Z-1)^2} \left( \frac{k}{(M+Zk^2)^4} [48[(Z-1)k^2]^2 k^2 + 147(M+k^2)^3 + 539(M+k^2)^2(Z-1)k^2 + \right. \right. \\ &\quad \left. \left. + 581(M^2+k^2)[(Z-1)k^2]^2 + 237[(Z-1)k^2]^3] + \right. \right. \\ &\quad \left. \left. - 147 \frac{1}{\sqrt{M+k^2}\sqrt{Z-1}} \operatorname{arccot} \left( \sqrt{\frac{M+k^2}{(Z-1)k^2}} \right) \right) (Z')^2 + \right. \\ &\quad \left. + \frac{1}{Z-1} \frac{1}{M+k^2} \left( \frac{k}{(M+Zk^2)^4} [96(M+k^2)(Z-1)k^4 + 42(M+k^2)^3 - 38(M+k^2)^2(Z-1)k^2 + \right. \right. \end{aligned}$$



$$\begin{aligned}
& -26(M+k^2)[(Z-1)k^2]^2 - 42[(Z-1)k^2]^3 - 42 \frac{1}{\sqrt{M+k^2}\sqrt{Z-1}} \operatorname{arccot}\left(\sqrt{\frac{M+k^2}{(Z-1)k^2}}\right) Z' M' + \\
& + 3 \frac{1}{(M+k^2)^2} \left( \frac{k}{(M+Zk^2)^4} [16(M+k^2)^2 k^2 - 3(M+k^2)^3 + 21(M+k^2)^2 (Z-1)k^2 + \right. \\
& \left. + 11(M+k^2)[(Z-1)k^2]^2 + 3[(Z-1)k^2]^3] + 3 \frac{1}{\sqrt{M+k^2}\sqrt{Z-1}} \operatorname{arccot}\left(\sqrt{\frac{M+k^2}{(Z-1)k^2}}\right) (M')^2 \right].
\end{aligned}$$

Here, however, we have to be careful, when the wave-function renormalization takes the value  $Z = 1$ , because the flow equations contain terms like  $1/(Z-1)$ . Nevertheless, by carefully taking the limit  $Z \rightarrow 1$ , one actually finds that the flow equations are well-defined and do not have poles at  $Z = 1$ . In fact, they reduce to

$$\lim_{Z \rightarrow 1} \partial_t M = \quad (D14)$$

$$= \frac{k^5}{6\pi^2} \left[ \frac{1}{(M+k^2)^2} M'' - 2 \frac{1}{(M+k^2)^3} (M')^2 \right],$$

and

$$\lim_{Z \rightarrow 1} \partial_t Z = \frac{k^5}{6\pi^2} \frac{1}{(M+k^2)^4} (M')^2. \quad (D15)$$

- 
- [1] N. Dupuis, L. Canet, A. Eichhorn, W. Metzner, J. M. Pawłowski, M. Tissier, and N. Wschebor, The nonperturbative functional renormalization group and its applications, *Phys. Rept.* **910**, 1 (2021), [arXiv:2006.04853 \[cond-mat.stat-mech\]](#).
  - [2] A. Koenigstein, M. J. Steil, N. Wink, E. Grossi, J. Braun, M. Buballa, and D. H. Rischke, Numerical fluid dynamics for FRG flow equations: Zero-dimensional QFTs as numerical test cases. I. The  $O(N)$  model, *Phys. Rev. D* **106**, 065012 (2022), [arXiv:2108.02504 \[cond-mat.stat-mech\]](#).
  - [3] A. Koenigstein, M. J. Steil, N. Wink, E. Grossi, and J. Braun, Numerical fluid dynamics for FRG flow equations: Zero-dimensional QFTs as numerical test cases. II. Entropy production and irreversibility of RG flows, *Phys. Rev. D* **106**, 065013 (2022), [arXiv:2108.10085 \[cond-mat.stat-mech\]](#).
  - [4] M. J. Steil and A. Koenigstein, Numerical fluid dynamics for FRG flow equations: Zero-dimensional QFTs as numerical test cases. III. Shock and rarefaction waves in RG flows reveal limitations of the  $N \rightarrow \infty$  limit in  $O(N)$ -type models, *Phys. Rev. D* **106**, 065014 (2022), [arXiv:2108.04037 \[cond-mat.stat-mech\]](#).
  - [5] M. J. Steil, *From zero-dimensional theories to inhomogeneous phases with the functional renormalization group*, *Phd thesis*, Technische Universität Darmstadt (2024).
  - [6] N. Zorbach, A. Koenigstein, and J. Braun, Functional Renormalization Group meets Computational Fluid Dynamics: RG flows in a multi-dimensional field space (2024), [arXiv:2412.16053 \[cond-mat.stat-mech\]](#).
  - [7] D. Bessis, C. Itzykson, and J.-B. Zuber, Quantum field theory techniques in graphical enumeration, *Adv. Appl. Math.* **1**, 109 (1980).
  - [8] J. Zinn-Justin, Vector models in the large  $N$  limit: A Few applications, in *11th Taiwan Spring School on Particles and Fields* (1998) [arXiv:hep-th/9810198](#).
  - [9] P. Di Vecchia, M. Kato, and N. Ohta, Double scaling limit in  $O(N)$  vector models, *Nucl. Phys. B* **357**, 495 (1991).
  - [10] S. Hikami and E. Brezin, Large order behavior of the  $1/N$  expansion in zero and one dimensions, *J. Phys. A* **12**, 759 (1979).
  - [11] S. Nishigaki and T. Yoneya, A nonperturbative theory of randomly branching chains, *Nucl. Phys. B* **348**, 787 (1991).
  - [12] S. Schelstraete and H. Verschelde, Large  $N$  limit of  $O(N)$  vector models, *Phys. Lett. B* **332**, 36 (1994), [arXiv:hep-th/9405158](#).
  - [13] A. G. Catalano, *Application of renormalization group techniques to the solution of integrals and Schrödinger eigenvalue equations*, *Master's thesis*, Politecnico di Torino (2019).
  - [14] S. Flörchinger, Functional Renormalization and Ultracold Quantum Gases, Springer Theses **10.1007/978-3-642-14113-3** (2010).
  - [15] J. Keitel and L. Bartosch, The zero-dimensional  $O(N)$  vector model as a benchmark for perturbation theory, the large- $N$  expansion and the functional renormalization group, *J. Phys. A* **A45**, 105401 (2012), [arXiv:1109.3013 \[cond-mat.stat-mech\]](#).
  - [16] D. Skinner, *Lecture notes: Quantum Field Theory II* (2018), [Online; accessed 2021.01.12].
  - [17] S. Moroz, *Few-body physics with functional renormalization*, *Phd thesis*, University of Heidelberg (2011).
  - [18] J. M. Pawłowski, *Solving integrals with flow equations*, Slides for the lecture *Non-perturbative aspects of gauge theories* winter term 2012/2013 (2013), [Online; accessed 2020.10.29].
  - [19] F. Strocchi, *An introduction to non-perturbative foundations of quantum field theory*, Vol. 158 (Oxford University Press, Oxford, 2013).
  - [20] S. Kemler and J. Braun, Towards a Renormalization Group approach to density functional theory – general formalism and case studies, *J. Phys. G* **40**, 085105 (2013), [arXiv:1304.1161 \[nucl-th\]](#).

- [21] D. S. Rosa, R. L. S. Farias, and R. O. Ramos, Reliability of the optimized perturbation theory in the 0-dimensional  $O(N)$  scalar field model, *Physica A* **464**, 11 (2016), [arXiv:1604.00537 \[hep-ph\]](#).
- [22] P. Millington and P. M. Saffin, Visualising quantum effective action calculations in zero dimensions, *J. Phys. A* **52**, 405401 (2019), [arXiv:1905.09674 \[hep-th\]](#).
- [23] P. Millington, *An alternative flow equation from the regulator-sourced 2PI effective action*, Talk at the 10th International Conference on Exact Renormalization Group 2020 (ERG2020) (2020), [Online; accessed 2021.01.12].
- [24] P. Millington and P. M. Saffin, Benchmarking regulator-sourced 2PI and average 1PI flow equations in zero dimensions, *J. Phys. A* **54**, 465401 (2021), [arXiv:2107.12914 \[hep-th\]](#).
- [25] A. Kurganov and E. Tadmor, New High-Resolution Semi-discrete Central Schemes for Hamilton-Jacobi Equations, *J. Comput. Phys.* **160**, 720 (2000).
- [26] A. Kurganov and E. Tadmor, New High-Resolution Central Schemes for Nonlinear Conservation Laws and Convection-Diffusion Equations, *J. Comput. Phys.* **160**, 241 (2000).
- [27] E. Grossi, F. J. Ihssen, J. M. Pawłowski, and N. Wink, Shocks and quark-meson scatterings at large density, *Phys. Rev. D* **104**, 016028 (2021), [arXiv:2102.01602 \[hep-ph\]](#).
- [28] F. Ihssen, J. M. Pawłowski, F. R. Sattler, and N. Wink, Toward quantitative precision for QCD at large densities, *Phys. Rev. D* **111**, 036030 (2025), [arXiv:2309.07335 \[hep-th\]](#).
- [29] C. Wetterich, The average action for scalar fields near phase transitions, *Z. Phys. C* **57**, 451 (1993).
- [30] C. Wetterich, Exact evolution equation for the effective potential, *Phys. Lett. B* **301**, 90 (1993), [arXiv:1710.05815 \[hep-th\]](#).
- [31] M. Reuter and C. Wetterich, Effective average action for gauge theories and exact evolution equations, *Nucl. Phys. B* **417**, 181 (1994).
- [32] T. R. Morris, The Exact Renormalization Group and approximate solutions, *Int. J. Mod. Phys. A* **09**, 2411 (1994), [arXiv:hep-ph/9308265](#).
- [33] N. Tetradis and C. Wetterich, Critical exponents from effective average action, *Nucl. Phys. B* **422**, 541 (1994), [arXiv:hep-ph/9308214](#).
- [34] U. Ellwanger, Flow equations for  $N$  point functions and bound states, *Z. Phys. C* **62**, 503 (1994), [arXiv:hep-ph/9308260](#).
- [35] J. Berges, N. Tetradis, and C. Wetterich, Nonperturbative renormalization flow in quantum field theory and statistical physics, *Phys. Rept.* **363**, 223 (2002), [arXiv:hep-ph/0005122](#).
- [36] C. Wetterich, Effective average action in statistical physics and quantum field theory, *Int. J. Mod. Phys. A* **16**, 1951 (2001), [arXiv:hep-ph/0101178](#).
- [37] J. M. Pawłowski, Aspects of the functional renormalisation group, *Annals Phys.* **322**, 2831 (2007), [arXiv:hep-th/0512261](#).
- [38] H. Gies, Introduction to the Functional RG and applications to gauge theories, *Lect. Notes Phys.* **852**, 287 (2012), [arXiv:hep-ph/0611146](#).
- [39] P. Kopietz, L. Bartosch, and F. Schütz, *Introduction to the Functional Renormalization Group*, Lecture Notes in Physics, Vol. 798 (Springer-Verlag Berlin Heidelberg, 2010).
- [40] O. J. Rosten, Fundamentals of the Exact Renormalization Group, *Phys. Rept.* **511**, 177 (2012), [arXiv:1003.1366 \[hep-th\]](#).
- [41] B. Delamotte, An introduction to the nonperturbative Renormalization Group, *Lect. Notes Phys.* **852**, 49 (2012), [arXiv:cond-mat/0702365](#).
- [42] A. Koenigstein, *Non-perturbative aspects of (low-dimensional) quantum field theories*, *Phd thesis*, Universitätsbibliothek Johann Christian Senckenberg (2023).
- [43] J. Zinn-Justin, Critical Phenomena: field theoretical approach, *Scholarpedia* **5**, 8346 (2010), revision #148508.
- [44] M. E. Peskin and D. V. Schroeder, *An introduction to quantum field theory* (Addison-Wesley, Reading, USA, 1995).
- [45] E. Grossi and N. Wink, Resolving phase transitions with discontinuous Galerkin methods, *SciPost Phys. Core* **6**, 071 (2023), [arXiv:1903.09503 \[hep-th\]](#).
- [46] N. Wink, *Towards the spectral properties and phase structure of QCD*, *Phd thesis*, University of Heidelberg (2020).
- [47] J. Stoll, N. Zorbach, A. Koenigstein, M. J. Steil, and S. Rechenberger, Bosonic fluctuations in the  $(1+1)$ -dimensional Gross-Neveu(-Yukawa) model at varying  $\mu$  and  $T$  and finite  $N$  (2021), [arXiv:2108.10616 \[hep-ph\]](#).
- [48] L. Batini, E. Grossi, and N. Wink, Dissipation dynamics of a scalar field, *Phys. Rev. D* **108**, 125021 (2023), [arXiv:2309.06586 \[hep-th\]](#).
- [49] F. Murgana, A. Koenigstein, and D. H. Rischke, Reanalysis of critical exponents for the  $O(N)$  model via a hydrodynamic approach to the functional renormalization group, *Phys. Rev. D* **108**, 116016 (2023), [arXiv:2303.16838 \[hep-th\]](#).
- [50] F. J. Ihssen, *Resolving the QCD phase structure*, *Phd thesis*, University of Heidelberg (2023).
- [51] N. Zorbach, J. Stoll, and J. Braun, Optimization and stabilization of functional renormalization group flows, *Phys. Rev. D* **111**, 096022 (2025), [arXiv:2401.12854 \[hep-ph\]](#).
- [52] F. Ihssen, J. M. Pawłowski, F. R. Sattler, and N. Wink, Towards quantitative precision in functional QCD I (2024), [arXiv:2408.08413 \[hep-ph\]](#).
- [53] N. Zorbach, J. P. Klinger, O. Philipsen, and J. Braun, Lattice Monte Carlo meets the lattice functional renormalization group: A quantitative comparison, *Phys. Rev. D* **112**, 076036 (2025), [arXiv:2503.14149 \[hep-lat\]](#).
- [54] F. R. Sattler, *The Phase Diagram of QCD at High Densities*, *Ph.D. thesis*, University of Heidelberg (2025).
- [55] F. Ihssen and J. M. Pawłowski, Functional flows for complex effective actions, *SciPost Phys.* **15**, 074 (2023), [arXiv:2207.10057 \[hep-th\]](#).
- [56] F. Ihssen, J. M. Pawłowski, F. R. Sattler, and N. Wink, Local discontinuous Galerkin for the functional renormalisation group, *Comput. Phys. Commun.* **300**, 109182 (2024), [arXiv:2207.12266 \[hep-th\]](#).
- [57] F. Ihssen, F. R. Sattler, and N. Wink, Numerical RG-time integration of the effective potential: Analysis and benchmark, *Phys. Rev. D* **107**, 114009 (2023), [arXiv:2302.04736 \[hep-th\]](#).
- [58] K. S. Jeong, F. Murgana, A. Dash, and D. H. Rischke, Functional Renormalization Group analysis of the quark-condensation pattern on the Fermi surface: A simple effective-model approach (2024), [arXiv:2407.13589 \[nucl-th\]](#).

- [59] F. R. Sattler and J. M. Pawłowski, DiFFRG: A Discretisation Framework for functional Renormalisation Group flows (2024), [arXiv:2412.13043 \[hep-ph\]](#).
- [60] L. Batini, *Relaxation and tunneling in nonequilibrium quantum field theory*, **Ph.D. thesis**, University of Heidelberg (2025).
- [61] R. Bellman, Dynamic Programming and a new formalism in the calculus of variations, *Proc. Natl. Acad. Sci. U.S.A.* **40**, 231 (1954).
- [62] J. Yong and X. Y. Zhou, *Stochastic Controls* (Springer, New York, NY, USA, 1999).
- [63] W. H. Fleming and H. M. Soner, *Controlled Markov Processes and Viscosity Solutions*, 2nd ed. (Springer, New York, NY, USA, 2006).
- [64] G. Fabbri, F. Gozzi, and A. Swiech, Stochastic Optimal Control in Infinite Dimension, SpringerLink [10.1007/978-3-319-53067-3](#) (2017).
- [65] H. V. Tran, *Hamilton-jacobi Equations: Theory and Applications* (2020), [Online; accessed 2025.11.16].
- [66] J. M. Lizana, T. R. Morris, and M. Perez-Victoria, Holographic renormalisation group flows and renormalisation from a Wilsonian perspective, *JHEP* **03**, 198, [arXiv:1511.04432 \[hep-th\]](#).
- [67] M. G. Ivanov, A. E. Kalugin, A. A. Ogarkova, and S. L. Ogarkov, On Functional Hamilton–Jacobi and Schrödinger Equations and Functional Renormalization Group, *Symmetry* **12**, 1657 (2020), [arXiv:2008.05862 \[hep-th\]](#).
- [68] C. Becchi, S. Giusto, and C. Imbimbo, The Wilson–Polchinski renormalization group equation in the planar limit, *Nucl. Phys. B* **633**, 250 (2002), [arXiv:hep-th/0202155](#).
- [69] B. Kappen and M. Toussaint, *Stochastic optimal control theory - ICML2008 tutorial* (2008).
- [70] A. Carosso, Stochastic Renormalization Group and Gradient Flow, *JHEP* **01** (172), [arXiv:1904.13057 \[hep-th\]](#).
- [71] J. Cotler and S. Rezchikov, Renormalization group flow as optimal transport, *Phys. Rev. D* **108**, 025003 (2023), [arXiv:2202.11737 \[hep-th\]](#).
- [72] F. A. Berezin, *The Method of Second Quantization*, Pure and applied physics : a series of monographs and textbooks. 24 (Academic Press, London, England, UK, 1966).
- [73] W. Greiner and J. Reinhardt, *Field quantization* (Springer, Berlin Heidelberg, 1996).
- [74] J. M. Pawłowski, M. M. Scherer, R. Schmidt, and S. J. Wetzel, Physics and the choice of regulators in functional renormalisation group flows, *Annals Phys.* **384**, 165 (2017), [arXiv:1512.03598 \[hep-th\]](#).
- [75] J. Braun, T. Dörfeld, B. Schallmo, and S. Töpfel, Renormalization group studies of dense relativistic systems, *Phys. Rev. D* **104**, 096002 (2021), [arXiv:2008.05978 \[hep-ph\]](#).
- [76] G. De Polsi and N. Wschebor, Regulator dependence in the functional renormalization group: A quantitative explanation, *Phys. Rev. E* **106**, 024111 (2022), [arXiv:2204.09170 \[cond-mat.stat-mech\]](#).
- [77] K. Symanzik, Small-distance behaviour in field theory, in *Proceedings, KfK Summer School 81 on Quarks and Nuclear Forces: Bad Liebenzell, Germany, September 27-October 3, 1981*, Vol. 57, edited by D. Fries and B. Zeitnitz (1971) pp. 222–236.
- [78] K. Symanzik, Small-distance-behaviour analysis and Wilson expansions, *Commun. Math. Phys.* **23**, 49 (1971).
- [79] J. Alexandre and J. Polonyi, Functional Callan–Symanzik equation, *Annals Phys.* **288**, 37 (2001), [arXiv:hep-th/0010128](#).
- [80] C. G. Callan, Broken Scale Invariance in Scalar Field Theory, *Phys. Rev. D* **2**, 1541 (1970).
- [81] K. Symanzik, Small distance behavior in field theory and power counting, *Commun. Math. Phys.* **18**, 227 (1970).
- [82] J. Braun, Y.-r. Chen, W.-j. Fu, A. Geißel, J. Horak, C. Huang, F. Ihssen, J. M. Pawłowski, M. Reichert, F. Rennecke, Y.-y. Tan, S. Töpfel, J. Wessely, and N. Wink, Renormalised spectral flows, *SciPost Phys. Core* **6**, 061 (2023), [arXiv:2206.10232 \[hep-th\]](#).
- [83] E. Oevermann, A. Koenigstein, and S. Floerchinger, Functional renormalization of QCD in 1+1 dimensions: Four-fermion interactions from quark-gluon dynamics, *Phys. Rev. D* **111**, 074006 (2025), [arXiv:2412.16051 \[hep-ph\]](#).
- [84] G. Fejős and A. Patkós, Field dependence of the Yukawa coupling in the three flavor quark-meson model, *Phys. Rev. D* **103**, 056015 (2021), [arXiv:2011.08387 \[hep-ph\]](#).
- [85] R. J. LeVeque, *Numerical methods for conservation laws*, 2nd ed. (Birkhäuser, Basel, 1992).
- [86] R. J. LeVeque, *Finite-volume methods for hyperbolic problems*, Cambridge Texts in Applied Mathematics (Cambridge University Press, 2002).
- [87] L. Rezzolla and O. Zanotti, *Relativistic hydrodynamics* (Oxford University Press, Oxford, England, UK, 2018).
- [88] J. S. Hesthaven and T. Warburton, *Nodal Discontinuous Galerkin Methods: Algorithms, Analysis, and Applications*, 1st ed. (Springer Publishing Company, Incorporated, 2007).
- [89] J. M. Pawłowski and F. Rennecke, Higher order quark-mesonic scattering processes and the phase structure of QCD, *Phys. Rev. D* **90**, 076002 (2014), [arXiv:1403.1179 \[hep-ph\]](#).
- [90] F. Rennecke and V. V. Skokov, Universal location of Yang–Lee edge singularity for a one-component field theory in  $1 \leq d \leq 4$ , *Annals Phys.* **444**, 169010 (2022), [arXiv:2203.16651 \[hep-ph\]](#).
- [91] G. Johnson, F. Rennecke, and V. V. Skokov, Universal location of Yang–Lee edge singularity in classic  $O(N)$  universality classes, *Phys. Rev. D* **107**, 116013 (2023), [arXiv:2211.00710 \[hep-ph\]](#).
- [92] F. Ihssen and J. M. Pawłowski, Flowing fields and optimal RG-flows (2023), [arXiv:2305.00816 \[hep-th\]](#).
- [93] F. Ihssen and J. M. Pawłowski, Physics-informed renormalisation group flows, *Annals Phys.* **481**, 170177 (2025), [arXiv:2409.13679 \[hep-th\]](#).
- [94] A. Bonanno, F. Ihssen, and J. M. Pawłowski, Tunneling with physics-informed RG flows in the anharmonic oscillator (2025), [arXiv:2504.03437 \[hep-th\]](#).
- [95] C. G. Michael and P.-L. Lions, Viscosity solutions of Hamilton–Jacobi equations, *Transactions of the American Mathematical Society* **277**, 1 (1983).
- [96] R. Jensen, The Maximum Principle for Viscosity Solutions of Fully Nonlinear Second Order Partial Differential Equations, *Archive for Rational Mechanics and Analysis* **101**, 1 (1988).
- [97] G. Barles, *Hamilton–Jacobi Equations: Approximations, Numerical Analysis and Applications* (Springer Berlin, Heidelberg, 2013) Chap. An Introduction to the Theory of Viscosity Solutions for First-Order Hamilton–

- Jacobi Equations and Applications, pp. 49–109.
- [98] V. Caselles, Scalar conservation laws and Hamilton-Jacobi equations in one-space variable, *Nonlinear Analysis: Theory, Methods & Applications* **18**, 461 (1992).
  - [99] S. Floerchinger, Exact flow equation for the divergence functional, *Phys. Lett. B* **846**, 138244 (2023), [arXiv:2303.04082 \[hep-th\]](#).
  - [100] F. Capellino, A. Dubla, S. Floerchinger, E. Grossi, A. Kirchner, and S. Masciocchi, Fluid dynamics of charm quarks in the quark-gluon plasma, *Phys. Rev. D* **108**, 116011 (2023), [arXiv:2307.14449 \[hep-ph\]](#).
  - [101] Wikipedia contributors, *Flux limiter* (2025), [Online; accessed 2025.10.03].
  - [102] Wolfram Research, Inc., *IDA Method for NDSolve* (2025).
  - [103] Wolfram Research, Inc., *Mathematica, Version 14.2* (2025).
  - [104] A. Connelly, G. Johnson, F. Rennecke, and V. Skokov, Universal Location of the Yang-Lee Edge Singularity in  $O(N)$  Theories, *Phys. Rev. Lett.* **125**, 191602 (2020), [arXiv:2006.12541 \[cond-mat.stat-mech\]](#).
  - [105] Y. Fujimoto, L. O’Raifeartaigh, and G. Parravicini, Effective potential for non-convex potentials, *Nucl. Phys. B* **212**, 268 (1983).
  - [106] A. Wipf, *Statistical Approach to Quantum Field Theory*, Lect. Notes Phys. No. 864 (Springer-Verlag, Berlin, Germany, 2013).
  - [107] G. A. Sod, A survey of several finite difference methods for systems of nonlinear hyperbolic conservation laws, *J. Comput. Phys.* **27**, 1 (1978).
  - [108] D. J. Gross and A. Neveu, Dynamical Symmetry Breaking in Asymptotically Free Field Theories, *Phys. Rev. D* **10**, 3235 (1974).
  - [109] B. Rosenstein, B. J. Warr, and S. H. Park, Dynamical symmetry breaking in four Fermi interaction models, *Phys. Rept.* **205**, 59 (1991).
  - [110] J. Zinn-Justin, *Quantum field theory and critical phenomena*, 4th ed., Int. Ser. Monogr. Phys., Vol. 113 (Oxford University Press, 2002) pp. 1–1054, a Clarendon Press Publication.
  - [111] A. G. Quinto, R. Vega Monroy, and A. F. Ferrari, Renormalization group improvement of the effective potential in a  $(1 + 1)$  dimensional Gross-Neveu model, *Nucl. Phys. B* **984**, 115959 (2022), [arXiv:2108.04079 \[hep-th\]](#).
  - [112] A. Chodos and H. Minakata, The Gross-Neveu model as an effective theory for polyacetylene, *Phys. Lett. A* **191**, 39 (1994).
  - [113] H. Takayama, Y. R. Lin-Liu, and K. Maki, Continuum model for solitons in polyacetylene, *Phys. Rev. B* **21**, 2388 (1980).
  - [114] I. K. Affleck, Phase Transition in the Lattice Gross-Neveu Model, *Phys. Lett. B* **109**, 307 (1982).
  - [115] R. Shankar, Ashkin-Teller and Gross-Neveu models: New relations and results, *Phys. Rev. Lett.* **55**, 453 (1985).
  - [116] B. J. Harrington and A. Yildiz, Chiral Symmetry Behavior at Large Densities, *Phys. Rev. D* **11**, 1705 (1975).
  - [117] B. J. Harrington and A. Yildiz, Restoration of Dynamically Broken Symmetries at Finite Temperature, *Phys. Rev. D* **11**, 779 (1975).
  - [118] L. Jacobs, Critical behavior in a class of  $O(N)$ -invariant field theories in two dimensions, *Phys. Rev. D* **10**, 3956 (1974).
  - [119] R. F. Dashen, S.-k. Ma, and R. Rajaraman, Finite temperature behavior of a relativistic field theory with dynamical symmetry breaking, *Phys. Rev. D* **11**, 1499 (1975).
  - [120] R. F. Dashen, B. Hasslacher, and A. Neveu, Semiclassical Bound States in an Asymptotically Free Theory, *Phys. Rev. D* **12**, 2443 (1975).
  - [121] U. Wolff, The phase diagram of the infinite-N Gross-Neveu model at finite temperature and chemical potential, *Phys. Lett. B* **157**, 303 (1985).
  - [122] T. F. Trembl, Dynamical mass generation in the Gross-Neveu model at finite temperature and density, *Phys. Rev. D* **39**, 679 (1989).
  - [123] R. Pausch, M. Thies, and V. L. Dolman, Solving the Gross-Neveu model with relativistic many body methods, *Z. Phys. A* **338**, 441 (1991).
  - [124] F. Karbstein and M. Thies, How to get from imaginary to real chemical potential, *Phys. Rev. D* **75**, 025003 (2007), [arXiv:hep-th/0610243](#).
  - [125] M. Thies, Analytical solution of the Gross-Neveu model at finite density, *Phys. Rev. D* **69**, 067703 (2004), [arXiv:hep-th/0308164](#).
  - [126] M. Thies and K. Urlichs, Revised phase diagram of the Gross-Neveu model, *Phys. Rev. D* **67**, 125015 (2003), [arXiv:hep-th/0302092](#).
  - [127] O. Schnetz, M. Thies, and K. Urlichs, Phase diagram of the Gross-Neveu model: Exact results and condensed matter precursors, *Annals Phys.* **314**, 425 (2004), [arXiv:hep-th/0402014](#).
  - [128] P. de Forcrand and U. Wenger, New baryon matter in the lattice Gross-Neveu model, *PoS LAT2006*, 152 (2006), [arXiv:hep-lat/0610117](#).
  - [129] J. Braun, S. Finkbeiner, F. Karbstein, and D. Roscher, Search for inhomogeneous phases in fermionic models, *Phys. Rev. D* **91**, 116006 (2015), [arXiv:1410.8181 \[hep-ph\]](#).
  - [130] L. Pannullo, J. Lenz, M. Wagner, B. Wellegehausen, and A. Wipf, Inhomogeneous phases in the 1+1 dimensional Gross-Neveu model at finite number of fermion flavors, *Acta Phys. Polon. Supp.* **13**, 127 (2020), [arXiv:1902.11066 \[hep-lat\]](#).
  - [131] J. Lenz, L. Pannullo, M. Wagner, B. Wellegehausen, and A. Wipf, Inhomogeneous phases in the Gross-Neveu model in 1+1 dimensions at finite number of flavors, *Phys. Rev. D* **101**, 094512 (2020), [arXiv:2004.00295 \[hep-lat\]](#).
  - [132] J. J. Lenz, L. Pannullo, M. Wagner, B. H. Wellegehausen, and A. Wipf, Baryons in the Gross-Neveu model in 1+1 dimensions at finite number of flavors, *Phys. Rev. D* **102**, 114501 (2020), [arXiv:2007.08382 \[hep-lat\]](#).
  - [133] S. Carignano, *Inhomogeneous chiral symmetry breaking phases*, Ph.D. thesis, Technische Universität Darmstadt (2012).
  - [134] M. Buballa and S. Carignano, Inhomogeneous chiral condensates, *Prog. Part. Nucl. Phys.* **81**, 39 (2015), [arXiv:1406.1367 \[hep-ph\]](#).
  - [135] A. Koenigstein, L. Pannullo, S. Rechenberger, M. J. Steil, and M. Winstel, Detecting inhomogeneous chiral condensation from the bosonic two-point function in the  $(1 + 1)$ -dimensional Gross-Neveu model in the mean-field approximation\*, *J. Phys. A* **55**, 375402 (2022), [arXiv:2112.07024 \[hep-ph\]](#).
  - [136] T. F. Motta, J. Bernhardt, M. Buballa, and C. S. Fischer, Toward a stability analysis of inhomogeneous phases in QCD, *Phys. Rev. D* **108**, 114019 (2023),

[arXiv:2306.09749 \[hep-ph\]](#).